



Università di Pisa
Physics Department

PhD Thesis

Out-of-equilibrium dynamics in round-trip and dissipation protocols

Behavior of the quantum phase transitions

Author:
Francesco Tarantelli

Supervisor:
Prof. Ettore Vicari

Session 2023/2024

Contents

Introduction	iii
1 Out-of-equilibrium dynamics	1
1.1 Introduction	1
1.2 Equilibrium Quantum Transitions	1
1.2.1 Continuous Quantum Transition (CQT)	1
1.2.2 First Order Quantum Transition (FOQT)	2
1.3 Unitary time-evolution	2
1.3.1 Quench	2
1.3.2 Kibble-Zurek mechanism	3
1.4 Time-evolution in Open Quantum Systems	3
1.4.1 Lindblad framework	3
1.4.2 Liouvillian gap	3
2 Round Trip variation of Hamiltonian parameter	5
2.1 Introduction	5
2.2 The models	5
2.2.1 Quantum many-body systems	5
2.2.2 Classical Ising model	7
2.3 One-way and round-trip KZ protocols across transition points	7
2.3.1 One-way KZ protocols	8
2.3.2 Round-trip KZ protocols	9
2.4 Observables to monitor the out-of-equilibrium dynamics	10
2.4.1 Quantum case	10
2.4.2 Classical case	11
2.5 Dynamic scaling along the one-way KZ protocol	11
2.5.1 Dynamic FSS for quantum KZ protocols	11
2.5.2 Dynamic FSS for classical KZ protocols	14
2.6 Dynamic scaling for the round-trip KZ protocol	15
2.6.1 Quantum dynamic FSS	15
2.6.2 Classical dynamic FSS	16
2.7 Numerical results	17
2.7.1 Along the quantum one-way KZ protocol	17
2.7.2 Along the classical round-trip KZ protocol	19
2.7.3 Along the quantum round-trip KZ protocol	22
2.8 Round-Trip across First-Order Transition	29
2.8.1 Driving Protocol	29
2.8.2 Finite Size Scaling at FOQT	32
2.8.3 Effective Description	34

2.8.4 Floquet Driving	40
3 Dissipation	45
3.1 Introduction	45
3.2 Out-of-equilibrium dynamics arising from a dissipation hole	46
3.2.1 Free lattice fermions with localized dissipative defects	47
3.2.2 Fermi gases within hard walls	50
3.2.3 Asymptotic stationary states	50
3.2.4 Approach to the asymptotic states	54
3.2.5 Intermediate scaling behaviors keeping N_0 fixed	58
3.2.6 Intermediate dynamic behavior keeping N_0/M fixed	59
3.3 Fermionic gases within harmonic traps	60
3.3.1 Large-time behavior	61
3.3.2 Large- L_t scaling behavior of the time dependence	63
3.4 From local to uniform dissipation: the sunburst model	64
3.4.1 Liouvillian Gap	66
3.4.2 Dynamic FSS Framework	69
3.4.3 Out-of-equilibrium FSS frameworks at CQTs with b fixed	71
3.4.4 Out-of-equilibrium FSS framework at CQTs with n fixed	72
3.5 Thermal-bath effects in quantum quenches	73
3.5.1 The fermionic Kitaev chain	73
3.5.2 Modelization of the thermal bath	74
3.5.3 Quantum-quench protocols	75
3.5.4 Observables monitoring the time evolution	75
3.5.5 Out-of-equilibrium scaling	76
4 Conclusions	83
A Round-trip Landau-Zener protocols in two-level models	86
A.1 Equilibrium FSS functions	92
A.2 FSS functions across a FOT	92
A.2.1 Single passage	93
A.2.2 Round trip	93
B Liouvillian gap	95
B.1 Steady-state solution and Δ_λ for $b = 1$	95
B.2 Simulation techniques	96
B.2.1 Time evolution of two-point functions (coordinate space)	97
B.2.2 Time evolution for $b \geq 1$ (momentum space)	97
B.2.3 Third quantization techniques: coordinate basis	98
B.2.4 Third quantization techniques: momentum basis	99
C Correlators in the thermal bath framework	101
C.1 Asymptotic thermal states	101
C.2 Computations for the unitary protocol	101
C.3 Computations for the dissipative protocol	102
References	104

Introduction

The progress achieved in the control of nano-scales many-body systems has recently renewed the interest in understanding the out-of-equilibrium dynamic in quantum spin models [1, 2]. Out-of-equilibrium, these efforts provided, for instance, a characterization of the unusual spreading of correlations and entanglement [3, 4, 5, 6, 7, 8, 9, 10], as well as of the thermalization [11, 12, 13, 14], in condensed-matter analogs of confined systems.

A deeper comprehension of the time evolution of the critical correlations and entanglement spreading is indeed sought by both the theoretical and experimental communities [15].

In the realm of many-body systems, intriguing out-of-equilibrium phenomena come to the forefront as these systems undergo phase transitions. Even when the timescale (τ_s) for varying system parameters is significantly extended, large-scale critical modes fail to reach equilibrium. This leads to a rich tapestry of dynamic phenomena at phase transitions, including hysteresis, coarsening, Kibble-Zurek (KZ) defect production [16, 17, 18, 19], aging, and more. Such phenomena have been explored extensively in both theoretical and experimental settings, spanning classical and quantum phase transitions (see, for instance, Refs. [20, 21, 22, 23, 24, 1, 25] and related references).

Out-of-equilibrium scaling behaviors tend to emerge when slowly traversing a critical point, especially when doing so in the large-timescale (τ_s) limit. These scaling behaviors depend on several factors, including the nature of the transition (classical or quantum), its universality class, and the specific characteristics of critical dynamics in classical systems (as detailed in Refs. [17, 19, 24, 1]). Slow, or quasiadiabatic, passages through these critical points enable researchers to unveil universal features related to the emergence of long-range modes during thermal and quantum critical phenomena.

In both classical and quantum contexts, many-body systems are described by Hamiltonians that can be expressed as:

$$H(t) \equiv H[w(t)] = H_c + w(t)H_p , \quad (1)$$

Here, $w(t)$ represents a time-dependent Hamiltonian parameter, while H_c and H_p are time-independent components. H_c serves as the critical Hamiltonian at the transition point, which might denote a quantum continuous transition driven by quantum fluctuations or a classical continuous transition fueled by thermal fluctuations. H_p , on the other hand, embodies a nontrivial, relevant perturbation. Within quantum many-body models, it's generally assumed that $[H_c, H_p] \neq 0$. The tunable parameter w controls the strength of the coupling with the perturbation H_p , and it's considered a relevant parameter guiding the continuous transition.

Consequently, $w_c = 0$ marks the transition point. To explore the scaling properties of out-of-equilibrium dynamics during phase transitions, researchers employ time-dependent protocols where parameters like $w(t)$ are slowly varied, linearly in time, across the transition point at $w_c = 0$, employing a large timescale t_s .

The inevitable growth of out-of-equilibrium dynamics during phase transitions in the thermodynamic limit arises because large-scale modes cannot equilibrate the long-range critical correlations that emerge at the transition point. This holds true even when the parameter w changes very slowly, and even in the limit of large timescales. Consequently, when starting from equilibrium states at the initial value w_i , the system cannot pass through equilibrium states corresponding to the values of $w(t)$ across the transition point. This departure from equilibrium results in distinctive out-of-equilibrium dynamic scaling phenomena, especially when observed in the limit of large timescale t_s . This scenario gives rise to the Kibble-Zurek (KZ) problem, which concerns the scaling behavior of the final number of defects after slow passages through continuous transitions from the disordered phase to the ordered phase.

Out-of-equilibrium scaling behaviors in many-body systems undergoing slow transitions across classical and quantum critical points exhibit intriguing similarities. These phenomena can be comprehensively analyzed within unified renormalization-group (RG) frameworks, analogous to those employed to understand equilibrium scaling behaviors, which can be related through quantum-to-classical mappings. However, it's important to note that the out-of-equilibrium scaling behavior in classical systems depends on the chosen dynamics, whether it involves purely relaxational processes or conserved quantities, leading to different dynamic features.

The first part embarks on an investigation into the effects of slow round-trip variations in the Hamiltonian parameter $w(t)$, which entail multiple crossings of quantum and thermal transitions. These round-trip protocols are initiated from equilibrium conditions, traverse the transition point, and return to their initial state, with the timescale t_s governing the slow-crossing regime in the large- t_s limit.

The exploration encompasses both classical and quantum continuous transitions, characterized by emerging long-range correlations. Unified RG frameworks are utilized to derive general dynamic scaling behaviors applicable to both classical and quantum transitions, considering large timescale t_s for round-trip KZ protocols and large system sizes L . This study builds upon existing dynamic RG frameworks used in standard one-way KZ protocols.

Notably, this study focuses on transitions between gapped phases characterized by short-range correlations, avoiding the complexities associated with gapless modes in ordered phases. This approach differs from standard KZ protocols, where systems transition from a disordered phase to ordered phases characterized by long-range correlations, leading to additional dynamic effects at large timescales, such as coarsening phenomena or the emergence of massless Goldstone excitations.

As the ensuing discussions reveal, while there are analogies in the scaling behaviors observed in standard one-way KZ protocols at classical and quantum transitions, these similarities only partially extend to round-trip KZ protocols. Significant differences emerge, especially when the extreme value $w_f > 0$ is held fixed and finite at the return point, a situation where classical systems exhibit well-defined scaling phenomena with hysteresis-like scenarios. In contrast, quantum systems encounter challenges in observing scaling behaviors along the return path due to rapidly oscillating relative phases between relevant quantum states, making the

return trajectory highly sensitive to protocol parameters, such as w_f and system size. This sensitivity is a consequence of the quantum unitary nature of dynamics, and it bears similarities to the behavior observed in quantum two-level models subject to round-trip protocols, akin to the Landau-Zener-Stckelberg problem.

Since any experimental device is unintentionally coupled to the environment, a particular emphasis is put on the dynamics of *open quantum systems* [26].

When the interactions of a quantum system with its surroundings are sufficiently weak, the real-time evolution of such apparatuses emerges from the interplay between the unitary and dissipative dynamics of the whole setup [27]. These hypotheses are usually satisfied within *Lindblad* frameworks, which underpin the modelization of most atomic, molecular, and optical devices (AMO) [28]. In such cases, the system is described in terms of a density matrix ρ , and the time evolution is controlled by *Lindblad Master equations*

$$\frac{d\rho}{dt} = \mathcal{L}[\rho]. \quad (2)$$

The system generally thermalizes to a Non-Equilibrium Steady-State (NESS) solution after a transitory time frame. However, determining whether the NESS is unique is a more subtle issue [29, 30]. A quantity of particular interest is the *Liouvillian gap*, hereafter denoted as Δ_λ . This energy scale sets the typical relaxation time required to make the NESS stand out, entailing a complete loss of information on the initial quantum state. Quantum memory devices, for example, would benefit from long relaxation times, therefore small Δ_λ [31].

Several works have addressed the nature of the Liouvillian gap in one-dimensional open quantum systems, considering different lattice geometries and dissipation sources also in integrable models [32]. Distinguished behaviors emerge when the dissipators are either isolated or in a relatively large number compared to the system size L . On the one hand, with bulk dissipation acting on the whole network, the system is gapped in several paradigmatic spin chains, such as XX, XXZ, and Ising models [33, 32, 34]. On the other hand, when the number of dissipative sources is constant, the Liouvillian gap generally vanishes with a distinctive power-law behavior in the thermodynamic limit, typically as $\sim L^{-3}$ [35, 36, 37]. In particular, we focus on homogeneous systems within hard walls and inhomogeneous systems where the particles are trapped by space-dependent external potentials, such as harmonic traps. We model the dissipative particle- decay mechanism by Lindblad master equations governing the time evolution of the density matrix. The resulting quantum dynamics is analyzed in protocols starting from the ground state of the Hamiltonian for N_0 particles, then evolving under the effect of one dissipative particle-loss defect, for example at the center of the system. We study the interplay between time, size l and the number N_0 of initial particles, considering two different situations: (i) fixed number N_0 of initial particles; (ii) fixed ratio N_0/l , corresponding to the thermodynamic limit of the initial equilibrium state. The physical mechanisms tying together these two regimes are still unclear and are, also, one of the main focus in this thesis.

Moreover, we investigate a $(1+1)$ -dimensional Kitaev ring with local particle-decay dissipators arranged in a *sunburst* geometry [38, 39, 40]. Starting the protocol in the proximity of a Continuous Quantum Transition (CQT), we study the

out-of-equilibrium dynamic using Renormalization Group (RG) arguments and Finite-Size Scaling (FSS) frameworks [41, 27].

Finally, we address the out-of-equilibrium dynamics arising from quantum-quench (QQ) protocols (instantaneous changes of the Hamiltonian parameters) in many-body systems within their quantum critical regime and in contact with (homogeneously coupled) thermal baths. We consider two classes of QQ protocols. In one of them the thermal bath is used to prepare the initial finite-temperature Gibbs state; then, after quenching, the thermal bath is removed and the dynamics of the system is unitary. We also address a more complex QQ protocol where the thermal bath is not removed after quenching, thus the quantum evolution is also driven by the interaction with the bath, which may be described by appropriate master equations for the density matrix of the system, where a further relevant time scale, or inverse decay rate, characterizes the system-bath coupling.

Outline

In the **Chapter 1**, we introduce all the equations and the definitions useful to present the original results in the last two chapters. Indeed, we give a brief intro on the quantum phase transitions and, then, we explain two different mechanisms which send the system out-of-equilibrium regime: the Kibble-Zurek mechanism and the Lindblad mechanism.

In the **Chapter 2**, we address the effect of a round-trip Kibble-Zurek protocol near a continuous and a first order quantum phase transition, using the Finite Size Scaling framework. We will find results which diverge from the classic hysteresis cycle scenario.

In the **Chapter 3**, we analyze the effects of a local and a uniform dissipation process on a second-order transition. We will focus on the interplay between these two type of dissipation mechanism, trying to extract common properties and different behaviors. Moreover, we focus also on the effects in the case in which we consider the interaction of our quantum many-body system with a thermal bath characterized by an uniform temperature T .

Chapter 1

Out-of-equilibrium dynamics

1.1 Introduction

In this chapter, we briefly introduce the main concepts which are the starting point of all the research statement. We will described the definition of transitions for many-body systems and some processes that drive out from this equilibrium, like:

- the unitary round-trip processes whose time-evolution is associated with an hermitian Hamiltonian;
- the dissipation processes in which we put our quantum system in contact with external baths.

We will always consider models which undergo a continuous quantum transition (CQT) and/or a first order transition (FOT).

All these concepts will be explored with more details in the future chapters of the work. The aim is to understand the behavior of a quantum system and its dynamics out of the equilibrium regime. We will use the Out-of-equilibrium Finite Size Scaling (OFSS) theory to discover the properties of these complex systems.

1.2 Equilibrium Quantum Transitions

1.2.1 Continuous Quantum Transition (CQT)

In the thermodynamic limit, i.e. infinite volume limit, same specific models could undergo a continuous phase transition. With the word phase, we intend the physical properties of the ground state associated with the Hamiltonian and characterized by the values of the Hamiltonian parameters. If this phase changes driving one of this parameter, we are in the presence of a quantum transition and the point, in which that happens, is called transition point.

In the particular case of the CQT, the quantum ground-state properties are continuous close to the transition point, called also critical point. In this special point, the system develops a long-distance correlations and its microscopic behavior becomes negligible.

Independent from the local details, the global properties determine a notable universal critical behavior in which we collect different physical systems in universality class. In terms of the Renormalization Group (RG) theory, the critical

point and its universal behavior are associated the fixed points of the RG flux. Hence, if we call b the characteristic unit length of the system and if we define the RG transformation as the parameter rescaling respect b , the physical observables satisfy general scaling law unchanged along all the RG flux [42, 41].

From a physics point of view, we can interpret the factor b like the spatial correlation length ξ which diverges approaching the critical point. According to the renormalization group (RG) theory of critical phenomena, these global properties may be the spatial dimensionality, the nature of the order parameter, the symmetry and the symmetry-breaking pattern [43].

Moreover, at CQTs the systems develop an equilibrium and dynamic scaling behavior in the thermodynamic limit and their quantum functions satisfy scaling power laws characterized by universal critical exponents [44].

1.2.2 First Order Quantum Transition (FOQT)

Quasi-degenerate vacua naturally arise in the context of quantum phase transitions, after a spontaneous symmetry breaking. Their behavior and coexistence in the non-critical regime is governed by a first-order quantum transition.

It is characterized by the crossings of the lowest-energy states in the infinite-volume limit and in the absence of conservation laws [45]. Instead, in a finite system, the energy gap among these states remain different from zero, giving rise to the phenomenon of avoided level crossing.

FOQTs are associated with many important out-of-equilibrium effects such as, including nucleations and metastability [20, 22], coarsening [46], and anomalous dependence on the boundary conditions [47, 48, 49, 50, 51].

1.3 Unitary time-evolution

1.3.1 Quench

In the quench protocol, we define a family of Hamiltonians of type:

$$H(\bar{\mu}) = H_o + \bar{\mu}P , \quad (1.1)$$

where in this case the scaling variable $\bar{\mu}$ tunes the strength of the perturbation P such that $[H_o, P] \neq 0$ and H_o is the unperturbed Hamiltonian whose parameters assume their critical values.

In this quench protocol, at $t = t_0$ the system starts in the ground state of the Hamiltonian associated with an initial value $\bar{\mu}_i$. Then, at time $t > 0$, we suddenly change the coupling from $\bar{\mu}$ to $\bar{\mu}_i$ and we follow the corresponding evolution of the system, described by the Schrödinger equation in the form of the Von-Neumann equation:

$$\partial_t \rho(t) = -i \left[\hat{H}(\bar{\mu}), \rho(t) \right] \quad \rho(t=0) = \rho_0 , \quad (1.2)$$

where $\rho(t)$ is the system density matrix at time t .

To express a possible scaling law, we define a further scaling variable associated with the time:

$$\theta = t\Delta , \quad (1.3)$$

which is obtained by recalling that the inverse energy difference of the lowest states is proportional to the relevant time scale of the critical modes.

1.3.2 Kibble-Zurek mechanism

The Kibble-Zurek(KZ) mechanism is related to the amount of final defects after slow passages through continuous transition, from disordered to the ordered phase [16, 17, 18, 19, 52]. This type of out-of-equilibrium process is several studied both analytically-numerically [24, 1, 46, 53] both experimentally [23, 25].

The large-scale modes, associated with the changes of the transition tuning parameter, are insufficient to equilibrate the long-distance critical correlations. Even in the large time variation regime, the out-of-equilibrium dynamics grows in the thermodynamic limit. In other words, when the system evolves, starting from an equilibrium state, the time-evolution is different from an adiabatic dynamics and the system does not pass through equilibrium states.

In this scenario, the out-of-equilibrium regime is always describable in terms of the RG framework and the equilibrium scaling behaviors can be related by the quantum to classical mapping [53, 42].

1.4 Time-evolution in Open Quantum Systems

1.4.1 Lindblad framework

To model the weak interaction between the previous quantum model and the surrounding environment, we consider local external baths each in contact with only site of the system chain. We work under the Born-Markov and secular approximations, so dissipators can be effectively modeled employing Lindblad quantum jump operators \hat{L}_x . In this limit, the time evolution of the density matrix can be described by Markovian master equations in the Lindblad form as [26, 36, 54]:

$$\frac{d\rho}{dt} = \mathcal{L}[\rho] = -i[H, \rho] + \mathbb{D}[\rho] ; \quad (1.4)$$

where \mathcal{L} is the Liouville superoperator, and \mathbb{D} is the corresponding dissipation term, whose strength is regulated by the coupling γ :

$$\mathbb{D}[\rho] = \gamma \sum_{x \in \mathcal{I}} \mathbb{D}_x[\rho] , \quad (1.5)$$

$$\mathbb{D}_x[\rho] = \hat{L}_x \rho \hat{L}_x^\dagger - \frac{1}{2} \left\{ \rho, \hat{L}_x^\dagger \hat{L}_x \right\} ; \quad (1.6)$$

where we indicate with \mathcal{I} the set of the external baths in contact with the quantum system.

1.4.2 Liouvillian gap

Let us consider the following equation:

$$\tilde{\mathcal{L}}[\tilde{\rho}_i] = \lambda_i \tilde{\rho}_i , \quad \lambda_i \in \mathbb{C} ; \quad (1.7)$$

where $\tilde{\mathcal{L}}$ is the (non-hermitian) Lindblad superoperator after the Choi-Jamiolkowski isomorphism [26, 55], and $\tilde{\rho}_i$ is the density matrix eigen-operator associated with the complex eigenvalue λ_i . In a few words, the transformation we have mentioned sends the density matrix ρ to $\tilde{\rho}$ through the mapping:

$$\rho_{ij} |i\rangle \langle j| \longrightarrow \tilde{\rho}_{ij} |i\rangle \langle j| . \quad (1.8)$$

Therefore, the vectorized $\tilde{\rho}$ lives in a 4^L -dimensional Hilbert space. In this basis, the action of $\tilde{\mathcal{L}}$ on $\tilde{\rho}$ can be written as follows:

$$\tilde{\mathcal{L}} = -i(\hat{H} \otimes \hat{\mathbb{I}} - \hat{\mathbb{I}} \otimes \hat{H}^t) + \gamma \sum_{x \in \mathcal{I}} \hat{L}_x \otimes \hat{L}_x^* \quad (1.9)$$

$$- \frac{\gamma}{2} \sum_{x \in \mathcal{I}} (\hat{L}_x^\dagger \hat{L}_x \otimes \hat{\mathbb{I}} + \hat{\mathbb{I}} \otimes \hat{L}_x^t \hat{L}_x^*) . \quad (1.10)$$

It can be shown that all eigenvalues of $\tilde{\mathcal{L}}$ satisfy $\text{Re}\lambda_i \leq 0$ [26]. The zero mode of the above operator represents the steady-state solution, namely, the NESS of the system. If \hat{L}_x is not hermitian, the density matrix corresponding to the steady-state solution is not proportional to the identity matrix [35]. We focus on the Liouvillian gap Δ_λ , which is the non-vanishing eigenvalue of \mathcal{L} with the smallest real part:

$$\Delta_\lambda = -\max_i \text{Re}\lambda_i . \quad (1.11)$$

This quantity controls the typical relaxation time of the longest-living eigenmode differing from the NESS.

Chapter 2

Round Trip variation of Hamiltonian parameter

2.1 Introduction

In this chapter, we analyze the effects of multiple crossing the quantum and the thermal transitions. In particular, we consider a round-trip evolution of an hamiltonian parameter starting from an equilibrium state. The main propose is to understand the details of the final state if the driving parameter returns to its initial value.

At first, we focus our attention upon a system which undergoes a continuous transition. Then, we replace the diverging correlation length and time with the corresponding typical scales characterizing a first order transition.

In fact, understanding whether similar scaling relations occur when the system is driven across a quantum/classical phase transition from an out-of-equilibrium configuration is still not clear.

Below, we investigate the emergence of finite-size scaling behaviors during this round-trip driving across the transition point.

2.2 The models

2.2.1 Quantum many-body systems

As a paradigmatic quantum many-body system we consider the 1D quantum Ising models, described by the Hamiltonian

$$H_{qI}(g, h) = -J \sum_{x=1}^L \sigma_x^{(1)} \sigma_{x+1}^{(1)} - g \sum_{x=1}^L \sigma_x^{(3)} - h \sum_{x=1}^L \sigma_x^{(1)}, \quad (2.1)$$

where L is the system size, $\sigma_x^{(k)}$ are the Pauli matrices on the x^{th} site ($k = 1, 2, 3$ labels the three spatial directions). Periodic and antiperiodic boundary conditions (respectively PBC and ABC) are set by requiring respectively $\sigma_{L+1}^{(k)} = \sigma_1^{(k)}$ and $\sigma_{L+1}^{(k)} = -\sigma_1^{(k)}$.

We recall that the quantum Ising model (2.1) develops a quantum critical behavior at $g = g_c = J$ and $h = 0$, belonging to the 2D Ising universality class, see e.g. Ref. [42]. The model is always gapped for $h \neq 0$. The relevant parameters

$r \equiv g - g_c$ and h are respectively associated with even and odd RG perturbations at the Ising fixed point. Their RG dimensions are respectively $y_r = 1/\nu = 1$ and $y_h = 15/8$. The dynamic exponent z , controlling the vanishing of the gap at the transition point, is given by $z = 1$. Moreover, we recall that the RG dimension of the order-parameter field, associated with the longitudinal operators $\sigma_x^{(1)}$, is given by $y_l = d + z - y_h = 1/8$, while that associated with the transverse operator $\sigma_x^{(3)}$ is given by $y_t = d + z - y_r = 1$. In the following we assume ferromagnetic nearest-neighbour interactions with $J = 1$, thus $g_c = J = 1$.

To achieve round-trip protocols between gapped phases, without degeneration of the lowest quantum states, we consider Ising chains with PBC at $g = g_c$ driven by a time-dependent longitudinal field $h(t)$, that is, comparing with Eq. (1), we identify

$$H_c = H_{qI}(g_c, 0), \quad w(t) = h(t), \quad H_p = -\sum_x \sigma_x^{(1)}. \quad (2.2)$$

The quantum Ising Hamiltonian $H_{qI}(g, 0)$ for vanishing longitudinal field h can be mapped into a quadratic model of spinless fermions through a Jordan-Wigner transformation [56, 57], obtaining the so-called quantum Kitaev wire: [58]

$$H_K(\mu) = -\sum_x (c_x^\dagger c_{x+1} + c_x^\dagger c_{x+1}^\dagger + \text{h.c.}) - \mu \sum_x n_x, \quad (2.3)$$

where $c_x^{(\dagger)}$ is the fermionic annihilation (creation) operator on site x of the chain, $n_x \equiv c_x^\dagger c_x$ is the corresponding number operator, and $\mu = -2g$. Analogously to the Ising spin representation, PBC and ABC are set by requiring respectively $c_{L+1} = c_1$ and $c_{L+1} = -c_1$. The Kitaev model undergoes a continuous quantum transition at $\mu_c = -2g_c = -2$. Of course, it belongs to the 2D Ising universality class as well, so that $y_\mu = y_r = 1/\nu = 1$ (there is no an analogue of the longitudinal field h of the spin formulation (2.1) within the above fermionic representation). At the Ising transition the fermionic operators c_x and the particle density operator n_x acquire the RG dimensions $y_c = 1/2$ and $y_n = 1$, respectively.

Although the bulk behaviors of the Ising and Kitaev models in the infinite-volume limit (and thus their phase diagram) are analogous, some features of finite-size systems may significantly differ. As a matter of fact, the nonlocal Jordan-Wigner transformation of the Ising chain with PBC or ABC does not simply map into the fermionic model (3.44) with PBC or ABC. Indeed further considerations apply [57, 59], leading to a less straightforward correspondence, which also depends on the parity of the particle-number eigenvalue. In particular, we note that the Kitaev quantum wire with ABC turns out to be gapped in both phases separated by the quantum transition at $\mu_c = -2$. Indeed, it does not exhibit the lowest-state degeneracy of the ordered phase of the quantum Ising chain (namely, the exponential suppression of the gap with increasing L). The reason for such substantial difference resides in the fact that the Hilbert space of the former is restricted with respect to that of the latter, so that it is not possible to restore the competition between the two vacua belonging to the symmetric/antisymmetric sectors of the Ising model [57, 58, 44, 53]. Therefore, a continuous quantum transition between gapped phases is also realized within the Kitaev wire with ABC, by choosing

$$H_c = H_K(\mu_c), \quad w(t) = \mu(t) - \mu_c, \quad H_p = -\sum_x n_x. \quad (2.4)$$

2.2.2 Classical Ising model

As a classical paradigmatic model undergoing a finite-temperature continuous transition, we consider the 2D Ising model, defined on a square lattice by the partition function

$$Z = \sum_{\{s_x\}} e^{-\beta H_{cI}}, \quad \beta = 1/T, \quad (2.5)$$

$$H_{cI}(J, h) = -J \sum_{\langle xy \rangle} s_x s_y - h \sum_x s_x, \quad (2.6)$$

where \mathbf{x} are the sites of the lattice, $\langle xy \rangle$ indicates the nearest-neighbour sites of the lattice, $s_x = \pm 1$ are classical spin variables, and h is an external homogenous magnetic field (we use the same symbol of the external longitudinal field of the quantum Ising model (2.1), but this should not lead to confusion). We consider systems with PBC. We again set $J = 1$. The square-lattice Ising model (2.6) undergoes a thermal continuous transition at $h = 0$ and $T_c = 2/\ln(\sqrt{2} + 1)$ [60]. The critical behavior belongs to the same universality class of the 1D quantum Ising model. Therefore, it is characterized by the critical exponents $\nu = 1$ and $\eta = 1/4$, and correspondingly the RG dimension associated with the temperature relevant parameter is given by $y_t = 1/\nu = 1$, and that associated with the odd external field h is $y_h = 2 - \eta/2 = 15/8$, see e.g. Ref. [43].

Since we are going to discuss dynamic behaviors, we must also define the type of dynamics driving the time evolution of the system. We consider a purely relaxational dynamics (also known as model A of critical dynamics [61, 62]), which can be realized by stochastic Langevin equations, or just Metropolis updatings in Monte Carlo simulations [63]. The corresponding dynamic exponent z has been accurately estimated by numerical studies, obtaining $z \approx 2.167$ with an apparent relative precision that is better than one per mille. Indeed, some of the most recent estimates of the dynamic exponent z for purely relaxational dynamics are $z = 2.1667(5)$ from [64], $z = 2.168(5)$ from [65], $z = 2.1665(12)$ from [66], $z = 2.172(6)$ from [67], $z = 2.170(6)$ from Ref. [68], which have been obtained by numerical analyses based on Monte Carlo simulations in equilibrium conditions. In the following we use the estimate $z = 2.167(1)$.

One may consider time-dependent KZ protocols also in this classical context, supplementing the partition function (2.5) defining the classical Ising model with the purely relaxational dynamics. Analogously to the quantum case, cf. Eq. (2.2), we consider 2D Ising models with PBC at T_c driven by a time-dependent magnetic field $h(t)$. Therefore, we identify

$$\begin{aligned} H_c &= H_{cI}(1, 0), & \beta = \beta_c &= \frac{\ln(\sqrt{2} + 1)}{2}, \\ w(t) &= h(t), & H_p &= - \sum_x s_x. \end{aligned} \quad (2.7)$$

2.3 One-way and round-trip KZ protocols across transition points

In the following we assume the general Hamiltonian (1), which represents the three models presented in Sec. 2.2 with the identifications in Eqs. (2.2), (2.4), and (2.7).

2.3.1 One-way KZ protocols

KZ-like protocols have been largely employed to investigate the dynamics of critical systems, at quantum transitions when the many-body system is subject to unitary time evolutions, and at classical thermal transitions considering, for example, a purely relaxational dynamics which can be implemented by standard Langevin equations [61].

Quantum KZ protocols

In the case of quantum many-body systems, quasi-adiabatic passages through the continuous quantum transition are obtained by slowly varying w across $w_c = 0$, following, e.g., the standard KZ procedure:

- (i) One starts from the ground state of the many-body system at $w_i < 0$, that is $|\Psi(t=0)\rangle \equiv |\Psi_0(w_i)\rangle$.
- (ii) Then the out-of-equilibrium unitary dynamics, ruled by the Schrödinger equation

$$\frac{d|\Psi(t)\rangle}{dt} = -i \hat{H}[w(t)] |\Psi(t)\rangle, \quad (2.8)$$

arises from a linear time dependence of the Hamiltonian parameter $w(t)$, such as

$$w(t) = t/t_s, \quad (2.9)$$

up to a final value $w_f > 0$. Therefore the KZ protocol starts at time $t_i = t_s w_i < 0$ and stops at $t_f = t_s w_f > 0$. The parameter t_s denotes the time scale of the slow variations of the Hamiltonian parameter w .

Across a continuous transition, the growth of an out-of-equilibrium dynamics is inevitable in the thermodynamic limit, even for very slow changes of the parameter w , because large-scale modes are unable to equilibrate as the system changes phase. Indeed, when starting from the ground state associated with the initial value w_i , the system cannot pass adiabatically through the ground states associated with $w(t)$ across the transition point (in the infinite volume limit), thus departing from an adiabatic dynamics. Note that, in the quantum cases that we consider, cf. Eqs. (2.2) and (2.4), the slow variation of the longitudinal field w brings the system from a gapped condition at $w_i < 0$ to another gapped condition for $w_f > 0$. This somehow differs from the standard situation of the KZ problem related to the defect production going from disorder to order phases. [16, 17, 18, 19, 52, 69, 70, 71, 24, 72, 46].

Classical KZ protocols

In the case of many-body systems at classical thermal transitions, one can again assume that slow passages through the continuous transition are obtained by slowly varying w across $w_c = 0$, following the classical KZ procedure:

- (i) One starts from an equilibrium thermalized configuration at $w_i < 0$.
- (ii) Then the out-equilibrium classical dynamics, ruled by the relaxational Langevin equation [61], or a standard Metropolis upgrading [63] of lattice configurations, arises from linear changing of the parameter $w(t)$, as $w(t) = t/t_s$, up to a final value $w_f > 0$. In the case of Metropolis-like dynamics, this can be

achieved by incrementing the time by one unity after one global sweep of the lattice variables (Metropolis upgrading of all lattice spin variables). Again the KZ protocol starts at time $t_i = t_s w_i < 0$ and stops at $t_f = t_s w_f > 0$.

Since the above protocol involves a stochastic relaxational process, results are obtained by averaging over an ensemble of trajectories (starting from an ensemble of thermalized configurations at w_i), obtained following the above protocol.

We remark again that the classical out-of-equilibrium phenomena associated with the above protocol occurs between two phases, for $w < 0$ and $w > 0$, with short-ranged correlations. This is again different from standard classical protocols associated with the KZ problem, in which one passes from a disordered to an ordered phase characterized by long-range correlations, where further important dynamic effects may set in, such as coarsening phenomena [46], in particular when the global symmetry is preserved by the KZ protocol and its initial state, such as coarsening phenomena or massless Goldstone excitations.

2.3.2 Round-trip KZ protocols

We now consider round-trip protocols in which the Hamiltonian parameter $w(t)$ varies linearly from $w_i < 0$ to $w_f > 0$, which is analogous to the one-way KZ protocol, and then linearly decreasing it back to the original value, crossing twice the transition point. For quantum systems:

- (i) One starts at $t = t_i$ from the ground state of the many-body system at $w_i < 0$, given by $|\Psi(t_i)\rangle \equiv |\Psi_0(w_i)\rangle$.
- (ii) The out-equilibrium unitary dynamics, ruled by the Schrödinger equation (2.8), is driven by linearly increasing $w(t)$: as $w(t) = t/t_s$ from $w_i < 0$ (at time $t_i = w_i t_s < 0$) to $w_f > 0$ (at time $t_f = w_f t_s > 0$).
- (iii) Then, for $t > t_f$ the dynamics is ruled by the Schrödinger equation (2.8) with an external field $w(t)$ that decreases linearly with the same time scale t_s , from $w_f > 0$ to the original value $w_i < 0$, closing the cycle.

To simplify the protocol, reducing its number of parameters, we consider a *symmetric* round-trip protocol (an extension of the later results to the most general case is straightforward) in which we fix

$$w_\star = w_f = -w_i, \quad (2.10)$$

and write the time dependence of $w(t)$ as

$$w(t) = \frac{\mathcal{T}(t)}{t_s} \quad \text{for } t_i = -t_\star \leq t \leq 3t_\star, \quad (2.11)$$

where

$$\mathcal{T}(t) = t_\star - |t - t_\star| \quad (2.12)$$

is the *triangular* function going linearly from $\mathcal{T}(-t_\star) = -t_\star$ to $\mathcal{T}(t_\star) = t_\star$, and then back to $\mathcal{T}(3t_\star) = -t_\star$. The parameter t_s represents the time scale of the variation. The parameter $t_\star > 0$ controls the extension, i.e. the starting and final times, of the protocols, from $t_i = -t_\star$ to $t_f = 3t_\star$, and also the interval of variation of $w(t)$, from $w(t_i) = -t_\star/t_s$ to $w(t_\star) = t_\star/t_s$.

Analogously to the quantum case, we extend the one-way KZ protocol for classical systems to round-trip protocols, by taking the time-dependent parameter $w(t)$ as in Eq. (2.11), with the same definitions.

2.4 Observables to monitor the out-of-equilibrium dynamics

2.4.1 Quantum case

The resulting out-of-equilibrium evolution of quantum many-body systems can be investigated by monitoring observables and correlations at fixed time. To characterize the departure from adiabaticity along the slow dynamic across the continuous transition, we monitor the adiabaticity function

$$A(t) = |\langle \Psi_0[w(t)] | \Psi(t) \rangle|, \quad (2.13)$$

where $|\Psi_0[w(t)]\rangle$ is the ground state of the Hamiltonian $H[w(t)]$, i.e. at instantaneous values of $w(t)$, while $|\Psi(t)\rangle$ is the actual time-dependent state evolving according to the Schrödinger equation (2.8).

The adiabaticity function measures the overlap of the time-dependent state with the corresponding ground state of the Hamiltonian at the same $w(t)$. Since the protocol starts from the ground state associated with $w_i = w(t_i)$, we trivially have $A(t_i) = 1$. If the quantum evolution is adiabatic, then $A(t) = 1$ at any time. In the general case arising from the protocols crossing transition points, $A(t)$ is expected to depart from the initial trivial value, due to the impossibility of the system to adiabatically follow the changes of the function $w(t)$ across its critical value $w = 0$. Note however that this is strictly true in the infinite-volume limit. In systems of finite size L , there is always a sufficiently large time scale t_s , so that the system can evolve adiabatically, essentially because finite-size systems are strictly gapped, although the gap Δ at the continuous quantum transition gets suppressed as $\Delta \sim L^{-z}$. The interplay between the size L and the time scale t_s gives rise to nontrivial out-of-equilibrium scaling behaviors, which can be studied within finite-size scaling (FSS) frameworks [53, 73].

Another general observable is related to the surplus energy of the system with respect to its instantaneous ground state at the given $w(t)$, i.e.

$$E_s(t) = \langle \Psi(t) | H | \Psi(t) \rangle - \langle \Psi_0[w(t)] | H | \Psi_0[w(t)] \rangle \geq 0. \quad (2.14)$$

Since the protocols considered start from a ground state at t_i , the surplus energy $E_s(t)$ vanishes along adiabatic evolutions, while nonzero values $E_s(t) > 0$ are related to the degree of out-of-equilibrium of the dynamics across the transition.

To monitor the out-of-equilibrium dynamics in the case of Ising models in the presence of a time-dependent longitudinal field $w(t)$, one may consider the evolution of the local and global average magnetization

$$m_x(t) \equiv \langle \Psi(t) | \sigma_x^{(1)} | \Psi(t) \rangle, \quad M(t) \equiv \frac{1}{L} \sum_x m_x(t), \quad (2.15)$$

as well as the fixed-time correlation function of the order-parameter operator and its space integral,

$$G(t, x, y) \equiv \langle \Psi(t) | \sigma_x^{(1)} \sigma_y^{(1)} | \Psi(t) \rangle. \quad (2.16)$$

Taking into account the translation invariance due to the absence of boundaries (such as the cases with PBC or ABC), we trivially have $m_x(t) = M(t)$ and

$G(t, x, y) \equiv G(t, x - y)$. We also consider the transverse magnetization

$$N(t) \equiv \frac{1}{L} \sum_x \langle \Psi(t) | \sigma_x^{(3)} | \Psi(t) \rangle. \quad (2.17)$$

More precisely, we consider the subtracted quantity

$$N_s(t) = N(t) - N_c, \quad (2.18)$$

where N_c is the ground-state transverse magnetization at the critical point, i.e. [59]

$$N_c = \lim_{L \rightarrow \infty} \langle \Psi_0, w=0 | \sigma_x^{(3)} | \Psi_0, w=0 \rangle = \frac{2}{\pi}. \quad (2.19)$$

In the case of the Kitaev model with ABC subject to a time-dependent chemical potential, one may also consider the particle density, and in particular the subtracted definition

$$\rho_s(t) \equiv \langle \Psi(t) | n_x | \Psi(t) \rangle - \rho_c, \quad (2.20)$$

which is independent of x due to translation invariance, and, for convenience, we have subtracted its known critical ground-state value in the infinite volume limit, which is given by [59] $\rho_c = (\pi - 2)/(2\pi) = 0.18169011\dots$. One may also consider the fermionic correlation functions, such as

$$\begin{aligned} P(x, t) &\equiv \langle \Psi(t) | c_j^\dagger c_{j+x}^\dagger + c_{j+x} c_j | \Psi(t) \rangle, \\ C(x, t) &\equiv \langle \Psi(t) | c_j^\dagger c_{j+x} + c_{j+x}^\dagger c_j | \Psi(t) \rangle, \\ D(x, t) &\equiv \langle \Psi(t) | n_j n_{j+x} | \Psi(t) \rangle_c, \end{aligned} \quad (2.21)$$

where $j, x \in [1, L/2]$, we have taken into account the translation invariance of systems with ABC, and the subscript c in the definition of $D(x, t)$ indicates that the connected part must be taken.

2.4.2 Classical case

In the case of the classical 2D Ising systems we consider the magnetization

$$m_{\mathbf{x}}(t) \equiv \langle s_{\mathbf{x}} \rangle_t, \quad M(t) \equiv \frac{1}{L^2} \sum_{\mathbf{x}} m_{\mathbf{x}}(t), \quad (2.22)$$

as well as the fixed-time correlation function of the order-parameter operator and its space integral,

$$G(t, \mathbf{x}, \mathbf{y}) \equiv \langle s_{\mathbf{x}} s_{\mathbf{y}} \rangle_t. \quad (2.23)$$

The symbol $\langle \rangle_t$ indicates the average over trajectories at time t . Taking into account the translation invariance due to the absence of boundaries (such as the cases with PBC), we trivially have $m_{\mathbf{x}}(t) = M(t)$ and $G(t, \mathbf{x}, \mathbf{y}) = G(t, \mathbf{x} - \mathbf{y})$.

2.5 Dynamic scaling along the one-way KZ protocol

2.5.1 Dynamic FSS for quantum KZ protocols

Dynamic FSS frameworks at quantum transitions has been reviewed in Ref. [53]. In this section we outline the dynamic scaling behavior that is expected to emerge

at the one-way KZ protocol of the models introduced in the previous sections, driven by the time dependent $w(t) = t/t_s$, starting from the ground state at $w_i = w(t_i) < 0$. For a RG derivation of the main features of the dynamic scaling at KZ protocols see Ref. [53] (in particular its chapter 9).

The dynamic scaling along one-way KZ protocols, such as those outlined in Sec. 2.3.1, entails the introduction of a number of appropriate scaling variables [53], such as

$$\begin{aligned} K &= w(t)L^{y_w}, & \Upsilon &= t_s/L^\zeta, \\ \Theta_i &= w_i t_s^{1-\kappa}, & \Theta &= w(t) t_s^{1-\kappa} = t/t_s^\kappa, \end{aligned} \quad (2.24)$$

where

$$\zeta = y_w + z, \quad \kappa = z/\zeta, \quad 1 - \kappa = y_w/\zeta. \quad (2.25)$$

Note that $\Theta \geq \Theta_i$, $K = \Upsilon^{\kappa-1}\Theta$, and that κ and $1 - \kappa$ are both positive and smaller than one. The asymptotic dynamic FSS behavior is obtained by taking $t_s \rightarrow \infty$ and $L \rightarrow \infty$, while keeping the scaling variables K , Υ , Θ and Θ_i fixed.

The dynamic FSS of a generic observable O_s , that is the expectation value of a local operator $O(x)$ with RG dimension y_o , and the corresponding two-point correlation function $G_O(x - y)$, behave as [53]

$$O_s(t, t_s, w_i, L) \approx L^{-y_o} \mathcal{O}(\Upsilon, \Theta, \Theta_i), \quad (2.26)$$

$$G_O(x, t, t_s, w_i, L) \approx L^{-2y_o} \mathcal{G}_O(X, \Upsilon, \Theta, \Theta_i), \quad (2.27)$$

where $X \equiv x/L$, and we assumed translation invariance, i.e., systems without boundaries such as PBC. The above scaling behaviors are expected to describe the dynamics within the interval $t_i \leq t \leq t_f$, corresponding to the interval $w_i \leq w(t) \leq w_f$, therefore the scaling variable Θ takes values within the interval

$$\Theta_i \leq \Theta \leq \Theta_f = w_f t_s^{1-\kappa} > 0. \quad (2.28)$$

Since the dynamic FSS limit at fixed $\Theta < \Theta_f$ does not depend on Θ_f , but only on Υ and Θ_i , in the following of this section dedicated to one-way KZ protocols, we omit the dependence on Θ_f . Of course, if we keep w_f fixed in the large- t_s limit, i.e. if we do not scale w_f to zero to keep Θ_f fixed, then $\Theta_f \rightarrow \infty$.

We also mention that the scaling functions may have a nontrivial large- Θ behavior. But we postpone this discussion when we will consider round-trip protocols, where the impact of the extremal value w_f , and therefore Θ_f , will be important for the return trajectories in quantum models.

Using the above general dynamic scaling ansatz, we can derive the dynamic FSS of the longitudinal magnetization M , the correlation function G , and the transverse magnetization N_s of the quantum Ising systems, cf. Eq. (2.15), (2.16), (2.17), and (2.18),

$$M(t, t_s, w_i, L) \approx L^{-y_l} \mathcal{M}(\Upsilon, \Theta, \Theta_i), \quad (2.29)$$

$$G(x, t, t_s, w_i, L) \approx L^{-2y_l} \mathcal{G}(X, \Upsilon, \Theta, \Theta_i), \quad (2.30)$$

$$N_s(t, t_s, w_i, L) \approx L^{-y_t} \mathcal{N}(\Upsilon, \Theta, \Theta_i), \quad (2.31)$$

where \mathcal{M} , \mathcal{G} and \mathcal{N} are appropriate scale functions, and we recall that $y_w = y_h = 15/8$, $y_l = 1/8$, and $y_t = 1$, for the 2D Ising universality class.

An analogous scaling behavior is put forward for the adiabaticity function in quantum systems, cf. Eq. (2.13),

$$A(t, t_s, w_i, L) \approx \mathcal{A}(\Upsilon, \Theta, \Theta_i) = \tilde{\mathcal{A}}(\Upsilon, K, \Theta_i). \quad (2.32)$$

Due to the initial condition of the KZ protocol, we must have $\mathcal{A} = 1$ for $\Theta = \Theta_i$. Moreover, since $\Upsilon \rightarrow \infty$ keeping K fixed corresponds to the adiabatic limit within the FSS framework, we must also have that

$$\tilde{\mathcal{A}}(\Upsilon \rightarrow \infty, K, \Theta_i) = 1. \quad (2.33)$$

Using standard RG arguments, we may also derive an ansatz for the dynamic scaling behavior of the surplus energy defined in Eq. (2.14), which turns out to be analogous to that of N_s , cf. Eq. (2.31), i.e.

$$E_s(t, t_s, w_i, L) \approx L^{y_t} \mathcal{E}_s(\Upsilon, \Theta, \Theta_i), \quad (2.34)$$

where $y_t = d + z - y_r = 1$ is the RG exponent associated with the even energy operator. Note that the leading analytic background contributions [44, 53], generally arising at the critical point, get cancelled by the difference of the two terms in the definition of E_s , cf. Eq. (2.14).

Assuming that the KZ protocol starts from a gapped phase, such as the case of Ising rings with any $|w| > 0$, and that the initial $w_i < 0$ is kept fixed in the dynamic scaling limit, the same dynamic FSS is expected to hold, irrespective of the value of w_i . Thus, the dynamic FSS behavior at fixed $w_i < 0$ in Eqs. (2.29) and (2.30) simplify to

$$M(t, t_s, w_i, L) \approx L^{-y_l} \mathcal{M}_f(\Upsilon, \Theta), \quad (2.35)$$

$$G(x, t, t_s, w_i, L) \approx L^{-2y_l} \mathcal{G}_f(X, \Upsilon, \Theta), \quad (2.36)$$

matching the $\Theta_i \rightarrow -\infty$ limit, i.e.

$$\mathcal{M}_f(\Upsilon, \Theta) = \mathcal{M}(\Upsilon, \Theta, \Theta_i \rightarrow -\infty), \quad (2.37)$$

and analogously for \mathcal{G}_f . Indeed, with increasing L , the dynamic FSS occurs within a smaller and smaller interval δ_w of values of $|w|$ around $w = 0$: since the time interval of the out-of-equilibrium process described by the scaling laws scales as $t_{\text{KZ}} \sim t_s^\kappa$, the relevant interval δ_w of values of $|w|$ shrinks as $\delta_w \sim t_{\text{KZ}}/t_s \sim L^{-y_w}$, when keeping Υ fixed.

Note that, in the limit $\Upsilon \rightarrow \infty$, the evolution as a function of $w(t) = t/t_s$ corresponds to an adiabatic dynamics. Indeed, since the finite size L guarantees the presence of a gap between the lowest states, one may adiabatically cross the critical point if $\Upsilon \rightarrow \infty$, passing through the ground states of the finite-size system for $w(t)$. The adiabatic evolution across the transition point is prevented only when $L \rightarrow \infty$ (before the limit $t_s \rightarrow \infty$), i.e., when the time scale t_r of the critical correlations diverges, as $t_r \sim \Delta^{-1} \sim L^z$. Within the FSS framework, the adiabatic limit is achieved by taking the $\Upsilon \rightarrow \infty$ limit keeping K fixed, cf. Eq. (2.24).

The scaling behavior in the infinite size *thermodynamic* limit can be straightforwardly obtained by taking the $L \rightarrow \infty$ limit of the FSS equations, therefore in

the limit $\Upsilon \rightarrow 0$. Thus, taking the large- t_s limit keeping the initial value w_i fixed, we expect the asymptotic scaling behavior

$$M(t, t_s, w_i, L \rightarrow \infty) \approx \lambda^{-y_l} \mathcal{M}_\infty(\Theta), \quad (2.38)$$

$$G(x, t, t_s, w_i, L \rightarrow \infty) \approx \xi_t^{-2y_l} \mathcal{G}_\infty(x/\xi_t, \Theta), \quad (2.39)$$

where

$$\lambda = t_s^{1/\zeta} \quad (2.40)$$

is the KZ length scale arising from the linear time-dependence of the Hmailtonian parameter across the transition. Note that

$$\mathcal{M}_\infty(\Theta) = \lim_{\Upsilon \rightarrow 0} \Upsilon^{y_l/\zeta} \mathcal{M}(\Upsilon, \Theta), \quad (2.41)$$

and an analogous relation can be derived for the two-point function. Moreover for the adiabaticity function we obtain

$$A(t, t_s, w_i, L \rightarrow \infty) \approx \mathcal{A}_\infty(\Theta) = \mathcal{A}(\Upsilon \rightarrow 0, \Theta). \quad (2.42)$$

Scaling corrections to the asymptotic dynamic scaling limit arises for finite time scales t_s , in particular for moderately large t_s . They are expected to be generally controlled by the leading irrelevant perturbations at the 2D Ising fixed point, which get suppressed as $\xi^{-\omega}$ (where ξ is diverging correlation length, or the KZ length scale λ) with the universal exponent $\omega = 2$ [74, 75, 44], and also from analytical contribution which dominates the corrections arising from the leading irrelevant perturbation [43, 53]. However, typically the leading corrections in out-of-equilibrium dynamic phenomena arising from KZ protocols are suppressed as λ^{-1} , cf. Eq. (2.40), or equivalently as $1/L$ in the dynamic FSS [53].

Analogous dynamic scaling behaviors are expected for the protocol within the Kitaev model, essentially replacing $w(t) = \mu(t) - \mu_c$, and $y_w = y_r = 1$, and using $y_c = 1/2$ and $y_n = 1$ (instead of y_l) for the scaling prefactor of the two-point functions defined in Eqs. (2.21).

2.5.2 Dynamic FSS for classical KZ protocols

The dynamic FSS framework at classical thermal continuous transitions is essentially analogous, that is we introduce the scaling variables (2.24) with the corresponding critical exponents, see Sec. 2.2.2. In particular, we recall that the dynamic exponent associated with the purely relaxational dynamics is given by $z = 2.167(1)$. Then the dynamic FSS of the observables introduced in Sec. 2.4.2 is the same as that reported in Eqs. (2.29) and (2.30). Analogous considerations concern protocols at finite fixed w_i , whose scaling behavior must match that obtained in the limit $\Theta_i \rightarrow -\infty$, thus leading to the scaling ansatzes reported in Eqs. (2.35) and (2.36), and also Eqs. (2.38), (2.39), and (2.40) in the infinite-volume limit, formally obtained in the $\Upsilon \rightarrow 0$ limit. The adiabatic limit is analogously obtained by taking the limit $\Upsilon \rightarrow \infty$.

However, further considerations apply to the classical system under purely relaxational dynamics, related to the fact that, within KZ protocols between phases with short-ranged correlations, such a dynamics leads to thermalization for sufficiently long times [76], after the out-of-equilibrium regime across the transition.

The limit $\Theta \rightarrow \infty$ of $\mathcal{M}(\Upsilon, \Theta)$ at fixed Υ is expected to lead to their infinite-volume equilibrium values. To infer it, note first that, in a finite volume, the slowest time scale scales as $\tau_r \sim L^z$ where z is the dynamic exponent. A necessary condition to obtain equilibrium results is therefore that $t_s \gg \tau_r$, i.e., $t_s L^{-z} \rightarrow \infty$. At fixed Υ we have $t_s L^{-z} = \Upsilon L^{y_w}$ and hence the condition is satisfied for $L \rightarrow \infty$. Since we take the limit $\Theta \rightarrow \infty$, we are considering the system at times t much larger than the time scale at which the off-equilibrium behavior occurs, so that the system is in equilibrium. Therefore, the scaling function \mathcal{M} should match its equilibrium counterpart $\mathcal{M}_e(K)$. Finally, since $K = w L^{y_w} = \Upsilon^{1-\kappa} \Theta$, in the limit $\Theta \rightarrow \infty$ at fixed Υ we have $K \rightarrow \infty$, i.e., we are considering the behavior in the infinite-volume limit.

The above considerations arising from thermalization under relaxational dynamics turn out to be the key point distinguishing round-trip protocols within classical and quantum contexts, see below.

2.6 Dynamic scaling for the round-trip KZ protocol

2.6.1 Quantum dynamic FSS

We now address the out-of-equilibrium dynamics at the round-trip protocols outlined in Sec. 2.3.2. The scaling arguments of the one-way protocol can be straightforwardly extended to the case of round trip. For round-trip protocols we also expect a further nontrivial dependence on the upper extremal value of w , i.e. w_f , through the scaling variable $\Theta_f = w_f t_s^{1-\kappa}$, to be added to the dependence on the initial values w_i and Θ_i . In the following we consider the *symmetric* round-trip protocol with $w_f = -w_i = w_*$, thus $\Theta_i = -\Theta_f$.

Analogously to the one-way KZ protocol, we define the scaling variables

$$\Upsilon = t_s/L^\zeta, \quad \Theta = w(t) t_s^{1-\kappa}, \quad \Theta_* = w_* t_s^{1-\kappa}, \quad (2.43)$$

where $|\Theta| \leq \Theta_*$, and the exponents ζ and κ are reported in Eq. (2.25). We also define $K = w(t)L^{y_w}$ and $X = x/L$. Note that now Θ is nonmonotonic as $w(t)$, cf. Eq. (2.11), i.e. it takes twice the same value. For this reason, we divide the time evolution into two parts: the first *outward* time evolution (a), from $\Theta = -\Theta_* < 0$ to $\Theta = \Theta_* > 0$ (corresponding to $-t_* \leq t \leq t_*$), and then the second *return* evolution (b), from $\Theta = \Theta_*$ to $\Theta = -\Theta_*$ (corresponding to $t_* \leq t \leq 3t_*$).

Again, the dynamic FSS behavior is expected to be obtained by taking $L \rightarrow \infty$, or equivalently $t_s \rightarrow \infty$, while keeping the scaling variables Υ , Θ , Θ_* , K and X fixed. Then, the expectation value O_s and correlation function $G_O(x-y)$ of a generic local observable $O(x)$ is given by

$$\begin{aligned} O_s^{(a/b)}(t, t_s, w_*, L) &\approx L^{-y_o} \mathcal{O}^{(a/b)}(\Upsilon, \Theta, \Theta_*), \\ G_O^{(a/b)}(x, t, t_s, w_*, L) &\approx L^{-2y_o} \mathcal{G}_O^{(a/b)}(X, \Upsilon, \Theta, \Theta_*) . \end{aligned} \quad (2.44)$$

Note that the values of the observables after the full cycle do not generally equal those at its beginning, i.e. for finite Υ

$$\mathcal{O}_s^{(b)}(\Upsilon, -\Theta_*, \Theta_*) \neq \mathcal{O}_s^{(a)}(\Upsilon, -\Theta_*, \Theta_*), \quad (2.45)$$

unless we consider the adiabatic limit $\Upsilon \rightarrow \infty$. The above scaling ansatz apply to any observable introduced in Sec. 2.4 for the quantum models considered. Finally, concerning the approach to the above asymptotic scaling behaviors, we expect scaling corrections analogous to those mentioned in the case of the one-way KZ protocol, at least when Θ_* is kept finite.

For example for the adiabaticity function and the surplus energy, we expect

$$A^{(a/b)}(t, t_s, w_*, L) \approx \mathcal{A}^{(a/b)}(\Upsilon, \Theta, \Theta_*), \quad (2.46)$$

$$E_s^{(a/b)}(t, t_s, w_*, L) \approx L^{y_t} \mathcal{E}_s^{(a/b)}(\Upsilon, \Theta, \Theta_*). \quad (2.47)$$

The above scaling behaviors appear quite similar to those already emerging at the one-way KZ protocols. However, a nontrivial issue concerns the existence of the large- Θ_* limit, or alternatively the existence of a scaling limit of the return trajectories when $w_* > 0$ is kept fixed in the round-trip protocol. As we shall see, classical and quantum systems turn out to behave differently. On the one hand, the relaxational dynamics of classical system lead to a well defined scaling when keeping $w_* > 0$ fixed, developing a hysteresis-like scenario. On the other hand, for quantum systems, thus unitary dynamics, such a limit turns out to be problematic, due to rapid oscillations which make the return somehow chaotic, and extremely sensitive to the protocol parameters, such as w_* , L , etc...

2.6.2 Classical dynamic FSS

Again, the RG framework allows us to describe the dynamic FSS arising from round-trip protocols in classical systems. Analogous scaling relations apply. Indeed, we introduce the same scaling variables as in Eq. (2.43), and the scaling equations (2.44) for generic observables, such as those defined in Eqs. (2.22) and (2.23). A key difference between quantum and classical systems is related to the large- Θ_* limit of these scaling equations.

The large- Θ_* limit is expected to be well defined for classical systems driven across transitions between phases with short-ranged correlations. This is essentially related to the fact that the purely relaxational dynamics is able to thermalize the system at finite $w = O(1)$, i.e. outside the critical region, for sufficiently large t_s . When $w(t) > 0$ the systems thermalize for a sufficiently large time t_{th} , reproducing an equilibrium behavior for any $t > t_{\text{th}}$, thus depending only on the actual value $w(t)$, and therefore independently of the versus of the time changes of $w(t)$. At the turning point the system is thermalized and ready to follow an equivalent trajectory toward $w = -w_*$. Of course, due to the inevitable out-of-equilibrium when crossing the transition, the return trajectory with decreasing $w(t)$ differs from the one with increasing $w(t)$, and the size of the area within the two curves somehow quantifies the degree of out-of-equilibrium. Therefore, for classical systems we expect that the following limits exists

$$\lim_{\Theta_* \rightarrow \infty} \mathcal{M}^{(a/b)}(\Upsilon, \Theta, \Theta_*) \equiv \mathcal{M}_f^{(a/b)}(\Upsilon, \Theta), \quad (2.48)$$

and analogously for the correlation functions, corresponding to round-trip protocols with finite $w_* > 0$. Moreover, the symmetry under \mathbb{Z}_2 reflection implies that

$$\mathcal{M}_f^{(b)}(\Upsilon, \Theta) = -\mathcal{M}_f^{(a)}(\Upsilon, -\Theta) \quad (2.49)$$

Since the two trajectories (*a*) and (*b*) gives rise to a close area, to achieve a quantitative indication of how far the system is out of equilibrium in the large- t_s limit, we may define [77]

$$I_A(t_s, w_\star, L) = -t_s^{-\kappa} \oint dt M(t, t_s, w_\star, L) \quad (2.50)$$

where the integration is over the time from the beginning to the end of the round-trip protocol. Assuming that the $\Theta_\star \rightarrow \infty$ is well defined, and the system develops a critical hysteresis, i.e. a closed area, during the whole round-trip protocol, the scaling behavior of I_A must be independent of the actual finite value of $w_\star > 0$. Using the dynamic FSS framework outlined above, we obtain the scaling prediction

$$\begin{aligned} I_A(t_s, w_\star, L) &\approx L^{-y_l} \mathcal{I}_A(\Upsilon) \\ &= -L^{-y_l} \int_{-\infty}^{\infty} d\theta \left[\mathcal{M}_f^{(a)}(\Upsilon, \theta) - \mathcal{M}_f^{(b)}(\Upsilon, \theta) \right] \\ &= -L^{-y_l} \int_{-\infty}^{\infty} d\theta \left[\mathcal{M}_f^{(a)}(\Upsilon, \theta) + \mathcal{M}_f^{(a)}(\Upsilon, -\theta) \right]. \end{aligned} \quad (2.51)$$

As we shall see, the scaling function $\mathcal{I}_A(\Upsilon \rightarrow \infty) = 0$ turns out to be well defined and finite. In particular, such area is expected to shrink in the adiabatic limit, i.e. for $\Upsilon \rightarrow \infty$.

2.7 Numerical results

In this section we report numerical analyses for the various quantum and classical models introduced in Sec. 2.2, subject to the one-way and round-trip KZ protocols outlined in Sec. 2.3.

2.7.1 Along the quantum one-way KZ protocol

The numerical analyses of quantum Ising chains (2.1) with a time-dependent longitudinal field is based on exact diagonalization. The corresponding Schrödinger equation is solved using a 4th order Runge-Kutta method. This approach allows us to compute the out-of-equilibrium dynamics up to lattice size $L \approx 16$, which, as we shall see, turns out to be sufficient to achieve substantial evidence of the dynamic FSS outlined in the previous sections.

We want to check the dynamic FSS put forward in Sec. 2.5.1. In the case of the quantum 1D Ising model (2.2), the exponents entering the definitions of the scaling variables (2.24) are

$$y_w = 15/8, \quad \zeta = 23/8, \quad \kappa = 8/23. \quad (2.52)$$

Some results for the one-way protocol are reported in Figs. 2.1 and 2.2, respectively for the adiabaticity function, defined in Eq. (2.13), and the longitudinal magnetization, defined in Eq. (2.15), at fixed Θ_i and w_i , for lattice sizes up to $L = 16$ and $L = 18$ respectively (this difference is due to the fact that the computation of the adiabaticity function is heavier). Although the system sizes of the available results are only moderately large, we clearly observe a collapse toward asymptotic

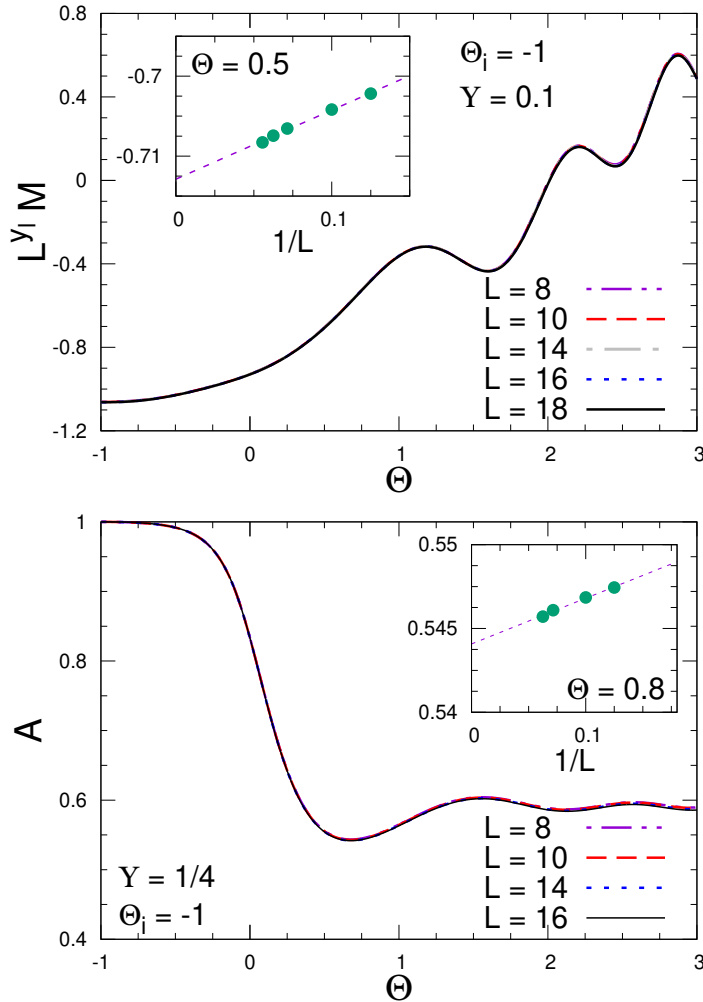


Figure 2.1: Dynamic FSS of the quantum Ising chain along the one-way KZ protocol at fixed $\Theta_i \equiv w_i L^{y_w}$. We show results for the adiabaticity function $A(t, t_s, w_i, L)$ at fixed $\Upsilon = t_s/L^\zeta = 1/4$ and $\Theta_i = -1$ up to $L = 16$ (bottom) and the longitudinal magnetization $M(t, t_s, w_i, L)$ at fixed $\Upsilon = 1/10$ and $\Theta_i = -1$ up to $L = 18$ (top), versus $\Theta = t/t_s^\kappa$. The exponents y_w , ζ , and κ are reported in Eq. (2.52). The approach to the large- t_s asymptotic behavior is globally characterized by $O(1/L)$ corrections (apart from small superimposed wiggles), see for example the inset of the figures (where the line is drawn to guide the eyes).

scaling curves, thus a robust evidence of the dynamic FSS outlined in Sec. 2.5.1. In particular, the dynamic FSS emerging from the data at fixed $w_i < 0$ turns out to be independent of the actual fixed value $w_i < 0$, as predicted by the scaling arguments reported in Sec. 2.5.1 (in Fig. 2.2 we only show results for $w_i = -1/8$, but we have explicitly checked the independence of $w_i < 0$ of the scaling curves). We note that, as expected, the adiabaticity function significantly drops crossing the quantum transition at finite values of Υ , while it remains close to one, i.e. the value corresponding to adiabatic evolutions, for large values of Υ . We also note that the data show that the convergence to the asymptotic dynamic FSS is globally consistent with $O(1/L)$ corrections (apart from superimposed wiggles).

Analogous results are obtained for the quantum Kitaev wire, with driving chemical potential. The corresponding exponents, cf. Eq. (2.25), entering the definitions

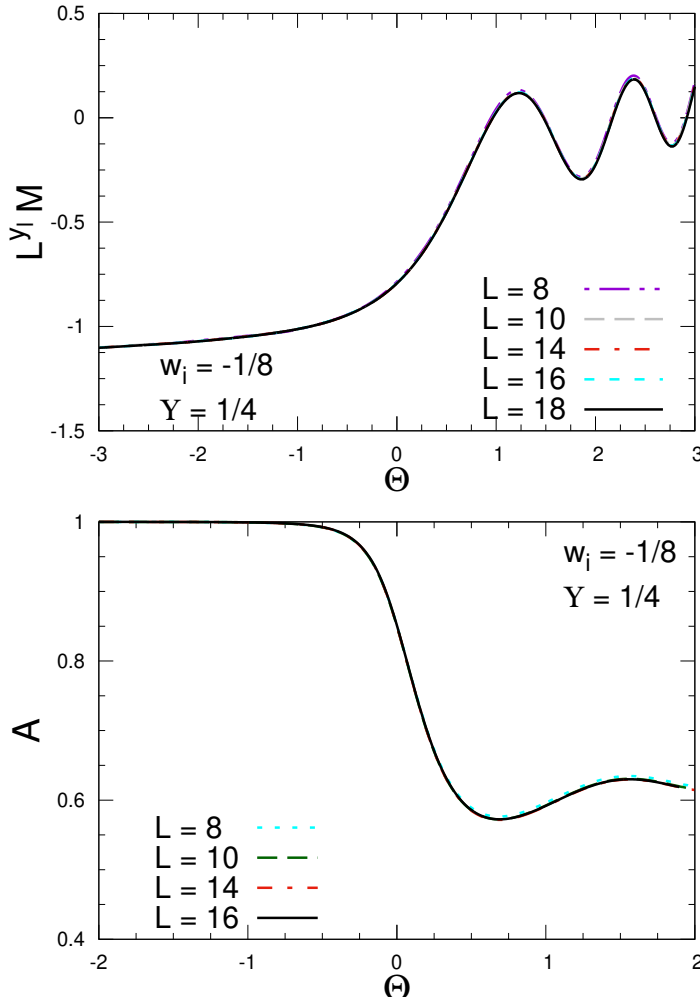


Figure 2.2: Dynamic FSS of the quantum Ising chain along the one-way KZ protocol at fixed $w_i < 0$. We show the adiabaticity function $A(t, t_s, w_i, L)$ up to $L = 16$ (bottom) and the longitudinal magnetization $M(t, t_s, w_i, L)$ up to $L = 18$ (top), at fixed $\Upsilon = 1/4$ and $w_i = -1/8$, versus Θ . As explained in the text, the scaling behavior emerging at fixed $w_i < 0$ matches that obtained in the $\Theta_i \rightarrow -\infty$ limit.

of the scaling variables (2.24), are

$$y_w = 1, \quad \zeta = 2, \quad \kappa = 1/2. \quad (2.53)$$

The simpler *integrable* nature of the quantum Kitaev wire (3.44) allows us to easily consider much larger systems, up to $L \approx 10^3$, using standard procedures after Fourier transforming to the momentum space. Again the resulting data (not shown) for the adiabaticity function, energy surplus, particle density, and the two-point functions, cf. Eq. (2.21), nicely support the dynamic FSS outlined in Sec. 2.5.1, see also Ref. [53].

2.7.2 Along the classical round-trip KZ protocol

The numerical analysis of the classical Ising model is based on standard Monte Carlo simulations based on local Metropolis upgrading procedures [63], which provide a purely relaxational dynamics without conserved quantities, that is model A

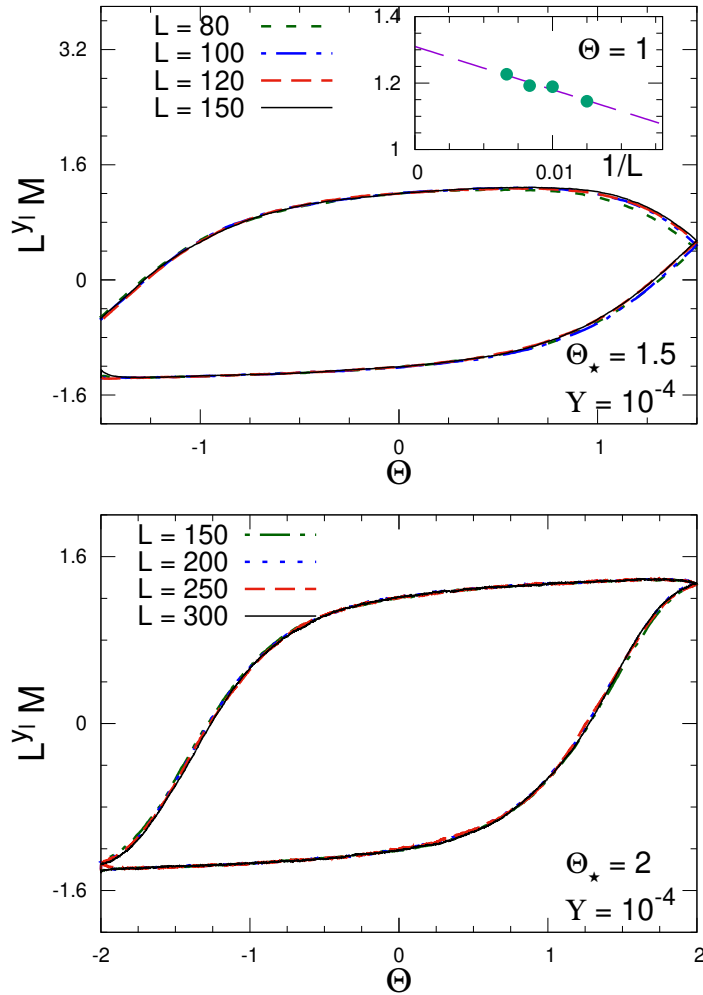


Figure 2.3: Dynamic FSS behavior of $M(t, t_s, w_*, L)$ for classical Ising model along the round-trip KZ protocol. Data are obtained at fixed $\Upsilon = 10^{-4}$, and fixed $\Theta_* = 1.5$ (top) and $\Theta_* = 2$ (bottom), and are plotted versus $\Theta = w(t)t_s^{1-\kappa}$. The convergence is globally consistent with a $1/L$ behavior, see for example the inset of the top figure. The values of the exponents y_w , ζ , and κ are reported in Eq. (2.54). Statistical errors are typically smaller than the thickness of the lines.

according to the standard classification reported in Ref. [61]. The time unit of this dynamics is represented by a global sweep of upgradings of all $L \times L$ spin variables. We perform the single-site update sequentially, moving from one site to one of its neighbours in a typewriter fashion. The results along the time-dependent protocols are obtained by averaging over a sample of trajectories (typically of order 10^3), starting from an ensemble of thermalized configurations at the initial parameter values. Also in this case relatively large systems can be simulated, typically for $L \gtrsim 10^2$.

The dynamic scaling arising from the one-way protocol is quite analogous to that observed at quantum transitions, with corresponding scaling behaviors, characterized by the static Ising critical exponents supplemented by the purely relaxational dynamic exponent $z = 2.167(1)$. The corresponding relevant exponents, cf. Eq. (2.25), entering the definitions of the scaling variables (2.24), are

$$y_w = 15/8, \quad \zeta = 4.0420(1), \quad \kappa = 0.5361(1). \quad (2.54)$$

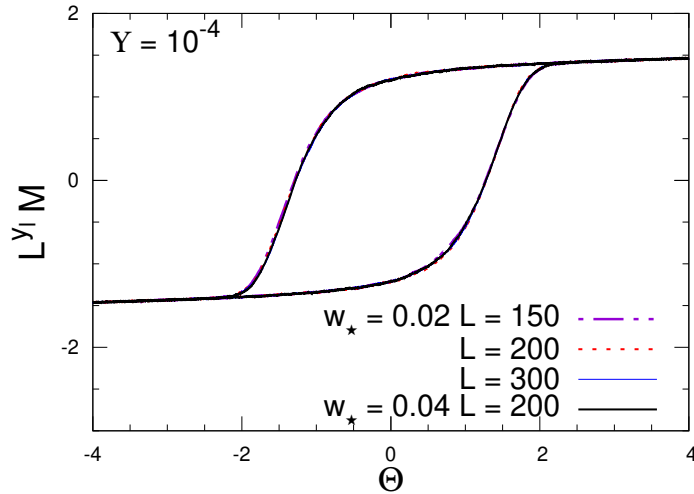


Figure 2.4: Dynamic FSS behavior of $M(t, t_s, w_*, L)$ for the classical 2D Ising model along the round-trip KZ protocol for fixed $\Upsilon = 10^{-4}$, and fixed $w_* = 0.02$ and $w_* = 0.04$. Statistical errors are typically smaller than the thickness of the lines. These results clearly support the predicted scaling behaviors, see Sec. 2.6.2, and their independence of the finite value of $w_* > 0$.

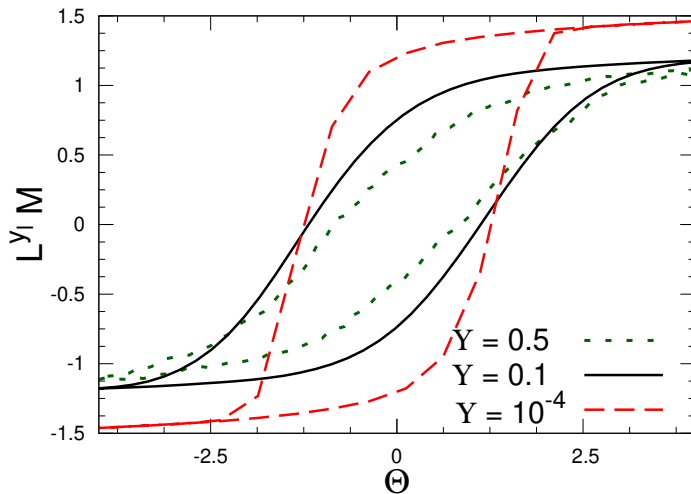


Figure 2.5: Hysteresis curves of the magnetization $M(t, t_s, w_*, L)$ for the classical 2D Ising model along the round-trip KZ protocol for various values of fixed Υ . They confirm that the hysteresis area decreases as Υ increases. The curve for $\Upsilon = 10^{-4}$ is taken from the data shown in Fig. 2.4, those for $\Upsilon = 0.1$ and $\Upsilon = 0.5$ are obtained from simulations for $L = 50$, whose size is already sufficient to provide a good approximation of the asymptotic large- L scaling curves (note that Monte Carlo simulations becomes more demanding with increasing Υ).

In the following we only report results for the round-trip KZ protocols, taking also into account that its first part is equivalent to the one-way KZ protocol.

The dynamic scaling behavior of the magnetization, cf. Eq. (2.44), is fully supported by the data reported in Fig. 2.3, for a fixed $\Upsilon = 10^{-4}$ and two different values of Θ_* . Analogous results are obtained for other values of Υ . As expected the round-trip cycle does not close the curves for finite values of Υ and Θ_* , see

Eq. (2.45), leaving a finite gap between the initial and final values of the cycle, i.e.

$$\mathcal{M}^{(b)}(\Upsilon, -\Theta_*, \Theta_*) - \mathcal{M}^{(a)}(\Upsilon, -\Theta_*, \Theta_*) > 0, \quad (2.55)$$

which becomes smaller and smaller with increasing Θ_* .

As argued in Sec. 2.6.2, the outward and return trajectories close in the large- Θ_* limit, and therefore for finite $w_* > 0$, giving rise to critical hysteresis phenomena. This is clearly demonstrated by the results shown in Fig. 2.4 for two different finite values of $w_* > 0$, whose scaling curves coincide. The outward and return curves for large $|\Theta|$ tend to coincide, differing only within a finite interval around $\Theta = 0$, which becomes smaller and smaller with increasing Υ , and vanishes in the adiabatic limit $\Upsilon \rightarrow \infty$. Such a dependence on Υ is demonstrated by the curves reported in Fig. 2.5 showing the magnetization hysteresis for various values of Υ . They confirm the scaling law (2.51) of the hysteresis area. Moreover, the data at small values of Υ hint at a convergence to a constant for $\Upsilon \rightarrow 0$, which corresponds to the infinite-volume limit.

As we shall see, these peculiar behaviors of round-trip protocols developing scaling hysteresis do not have a quantum counterpart, being strictly connected with the thermalizing relaxational dynamics of classical models.

We also stress that the above hysteresis scenario arises from the round-trip protocols between phases with short-ranged correlations. More complicated situations are expected to occur when round-trip protocols involve ordered phases, where coarsening phenomena may drastically change the picture, in particular along the return trip, in the large- Θ_* limit.

2.7.3 Along the quantum round-trip KZ protocol

Scaling for finite Θ_*

To begin with, we show results for round-trip KZ protocols for the quantum Ising chain, cf. Eq. (2.2), when keeping Θ_* finite, see Figs. 2.6 and 2.7, respectively for the adiabaticity function, the longitudinal and transverse magnetizations. Analogous results are obtained for other values of Υ and Θ_* . They nicely support the scaling behaviors put forward in Sec. 2.6.1. Analogous results are obtained for the quantum Kitaev wire, cf. Eq. (2.4), see for example the results shown in Figs. 2.8, 2.9, and 2.10, respectively for the adiabaticity function, the surplus energy E_s defined in Eq. (2.14), and the two point function defined in Eq. (2.21). They nicely support the dynamic FSS at fixed finite Θ_* .

The limit $\Theta_* \rightarrow \infty$

We now discuss the large- Θ_* limit, or equivalently the case in which we keep $w_* > 0$ fixed in the round-trip protocols. This limit turns out to be quite problematic in quantum round-trip KZ protocols.

Some hints at the absence of a well defined large- Θ_* limit of the dynamic scaling behavior are shown by the plots of Fig. 2.11 reporting the longitudinal magnetization of a quantum Ising system of size $L = 10$ for various Θ_* , whose return paths do not show any apparent convergence when increasing Θ_* .

The return trajectories keeping $w_* > 0$ fixed do not show evidence of convergence in the large- L dynamic scaling limit. This is shown by the curves of

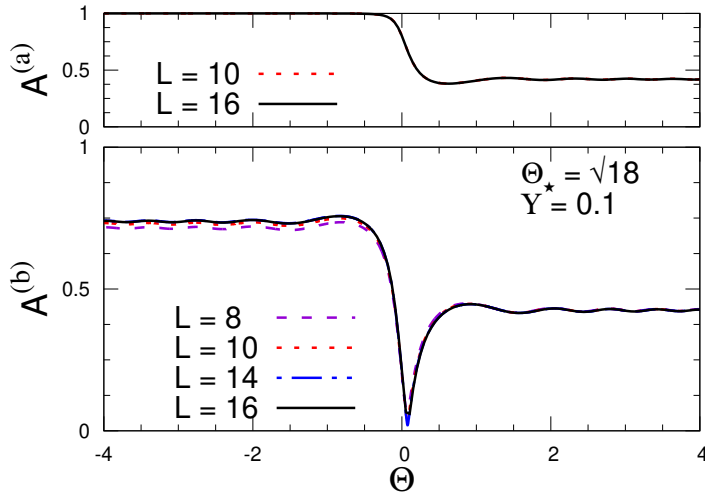


Figure 2.6: Round-trip dynamic FSS of the quantum Ising chain, cf. Eq. (2.2), for a finite Θ_* . We show results for the adiabaticity function $A(t, t_s, w_*, L)$ at fixed $\Upsilon = t_s/L^\zeta = 0.1$ and $\Theta_* = w_* L^{1-\kappa} = 3\sqrt{2}$, for the outward (top) and return (bottom) branches of the round-trip KZ protocol, versus $\Theta = w(t)L^{1-\kappa}$, for various size L up to $L = 16$. The values of the exponents y_w , ζ , and κ are reported in Eq. (2.52). The shown results clearly support the dynamic scaling behavior given in Eq. (2.46).

the adiabaticity function along the return branch of the round-trip protocol, see Fig. 2.12, for $w_* = 1/4$ and $\Upsilon = 0.1$. While convergence is clearly observed along the outward part, as expected because the one-way protocol showed a well defined limit in the large- $|\Theta_i|$ limit, the return pattern does not show a stable convergence pattern. The same behavior is also shown by the longitudinal and transverse magnetizations M and N , see for example Fig. 2.13. Analogous results are also obtained for the quantum Kitaev wire, see Fig. 2.14, where we report results for the adiabaticity function at $\Upsilon = 0.001$ and various large values of Θ_* , for a large lattice size $L = 2000$.

Actually, such an instability appears quite similar to that emerging in analogous round-trip protocols within two-level systems. They are discussed in App. A. Similarly to the Landau-Zener problem [78], we consider a time-dependent two-level Hamiltonian

$$H_{2\ell}(t) = -\beta(t)\sigma^{(3)} + \frac{\Delta}{2}\sigma^{(1)}, \quad (2.56)$$

where Δ is a constant,

$$\beta(t) = \frac{\mathcal{T}(t)}{t_s} \quad \text{for } t_i = -t_* \leq t \leq 3t_*, \quad (2.57)$$

and $\mathcal{T}(t) = t_* - |t - t_*|$ is the triangular function. The quantities $\tau = \mathcal{T}(t)/\sqrt{t_s}$ and $\tau_* = t_*/\sqrt{t_s}$ play the same role of the scaling variables Θ and Θ_* describing the round-trip KZ protocols in quantum many-body systems. The corresponding Schrödinger functions can be analytically solved in terms of parabolic cylinder functions $D_\nu(x)$ [79], see App. A.

The resulting behavior of the expectation values of $\sigma^{(3)}$ and the adiabatic function show that the large- τ_* limit is problematic, being characterized by large $O(1)$

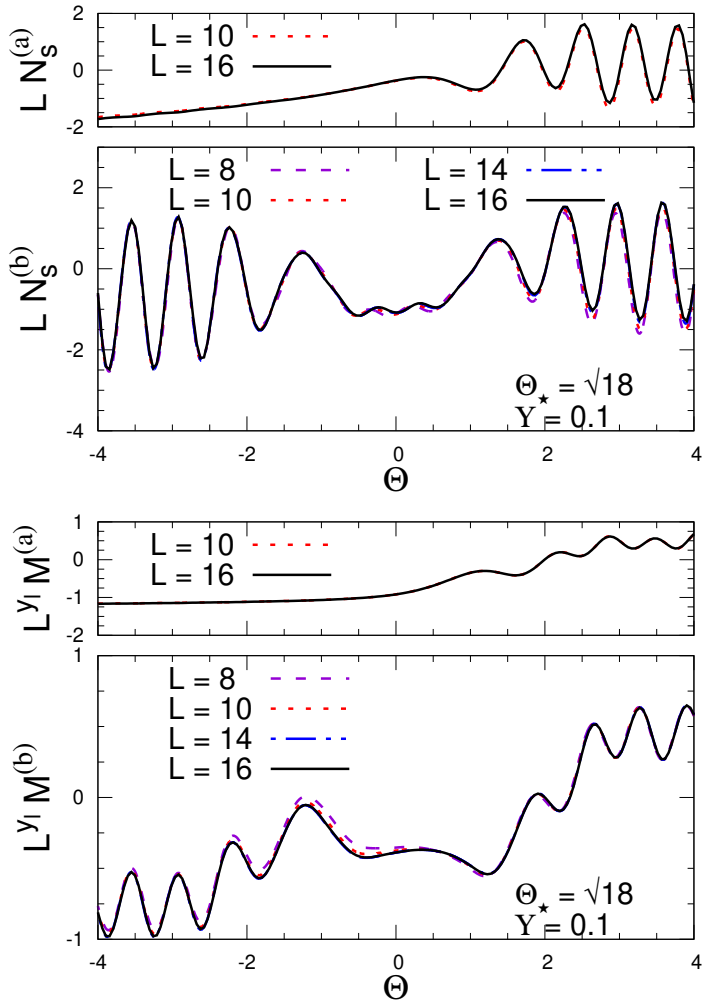


Figure 2.7: Round-trip dynamic FSS of the longitudinal magnetization $M(t, t_s, w_*, L)$ (bottom figure) and subtracted transverse magnetization $N_s(t, t_s, w_*, L)$ (top figures), cf. Eq. (2.18), in the quantum Ising chain at fixed $\Upsilon = 0.1$ and $\Theta_* = 3\sqrt{2}$, for the outward (top) and return (bottom) branches of the round-trip KZ protocol, versus Θ , for various size L up to $L = 16$. The results clearly support the dynamic scaling behavior given in Eq. (2.44).

oscillations with frequencies increasing proportionally to τ_* , roughly. See App. A for details. They turn out to be related to the rapid changes of the relative phase between the relevant states of the two-level system at the extremal values $\tau = \tau_*$ when τ_* becomes large, increasing as τ_*^2 . Since the quantum evolution along the return trajectory turns out to be very dependent on such phase, it becomes extremely sensitive to the value of τ_* , showing analogous oscillations. As a consequence, the value of all observables along the return trajectory, from $\tau = \tau_*$ down to the return point $\tau = -\tau_*$, do not show a well defined limit for $\tau_* \rightarrow \infty$. The size of the oscillations depend on the value of the scaling variable Υ , and tend to be suppressed in the adiabatic limit $\Upsilon \rightarrow \infty$.

We observe a similar behavior in the quantum many-body systems. This scenario is demonstrated by the results shown in Fig. 2.15, where we report the values of A , M , and N_s at end of the outward branch and at the end of the return branch for some interval of values of Θ_* , around large values of Θ_* and fixed $L = 10$.

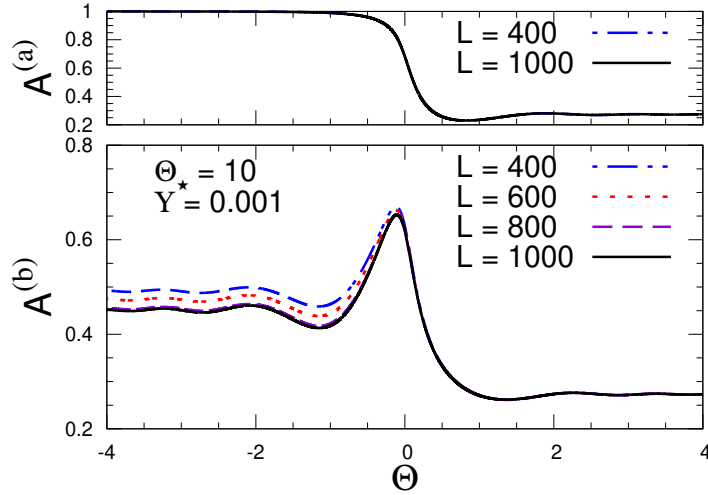


Figure 2.8: Round-trip dynamic FSS within the quantum Kitaev wire for a finite Θ_* . We show results for the adiabaticity function $A(t, t_s, w_*, L)$ at fixed $\Upsilon = t_s/L^\zeta = 0.001$ and $\Theta_* = w_* L^{1-\kappa} = 10$, for the outward (top) and return (bottom) branches of the round-trip KZ protocol, versus $\Theta = w(t)L^{1-\kappa}$, for various size L up to $L = 1000$. The values of the exponents y_w , ζ , and κ are reported in Eq. (2.53). The numerical results clearly support the dynamic scaling behavior given in Eq. (2.46).

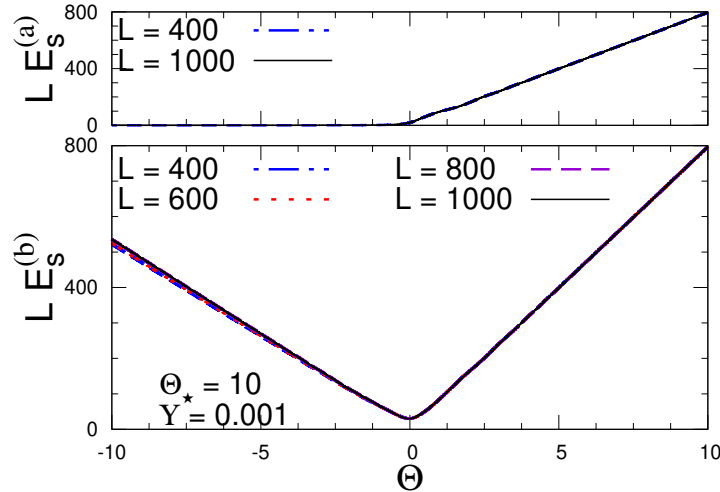


Figure 2.9: Round-trip dynamic FSS within the quantum Kitaev wire for a finite Θ_* . We show results for the surplus energy $E_s(t, t_s, w_*, L)$ defined in Eq. (2.14), at $\Upsilon = t_s/L^\zeta = 0.001$, and $\Theta_* = w_* L^{1-\kappa} = 10$, for the outward (top) and return (bottom) branches of the round-trip KZ protocol, versus $\Theta = w(t)L^{1-\kappa}$, for various size L up to $L = 1000$. The results clearly support the dynamic scaling behavior given in Eq. (2.47).

Similarly to the results obtained for two-level model, the observables at the end of the outward branch oscillate, with a frequency that becomes larger and larger with increasing Θ_* , and the oscillations observed after the whole cycle are strongly correlated to those at the end of the first branch, doubling the frequency. Analogous results are obtained for other values of Υ . We also note that the oscillations

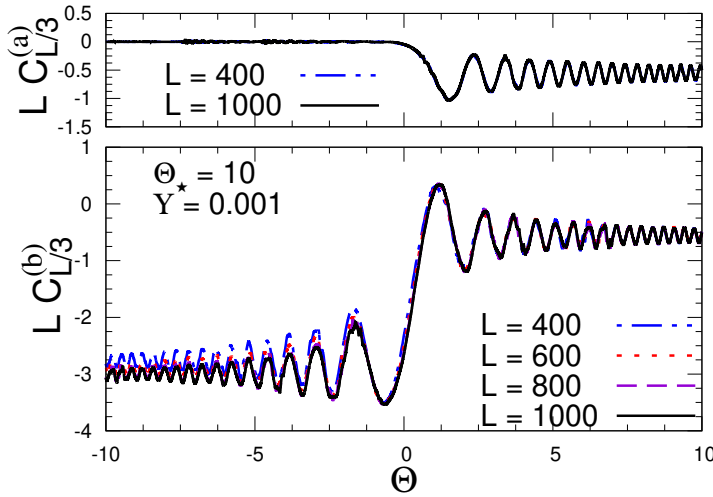


Figure 2.10: Round-trip dynamic FSS within the quantum Kitaev wire for a finite Θ_* . We show results for the two-point function $C(x, t, t_s, w_*, L)$, cf. Eq. (2.21), at fixed $X = x/L = 1/3$, $\Upsilon = t_s/L^\zeta = 0.001$, and $\Theta_* = w_* L^{1-\kappa} = 10$, for the outward (top) and return (bottom) branches of the round-trip KZ protocol, versus $\Theta = w(t)L^{1-\kappa}$, for various size L up to $L = 1000$.

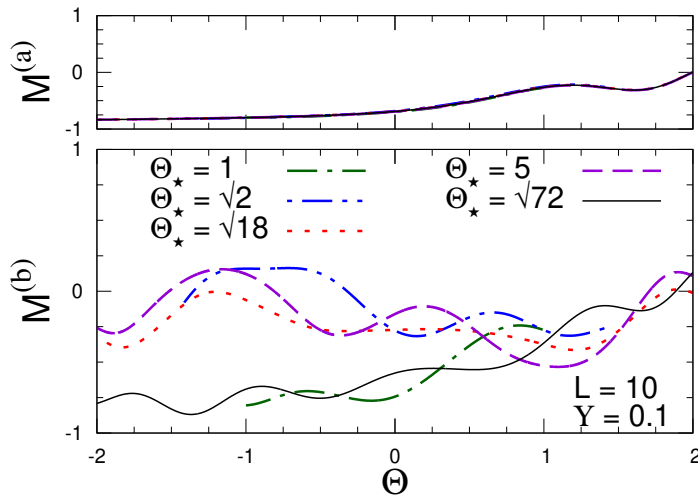


Figure 2.11: Behavior of $M(t, t_s, w_*, L)$ for fixed $L = 10$, $\Upsilon = 0.1$ for the one way trip (top figure) and for the return trip (bottom figure), versus Θ , for various Θ_* up to $\Theta_* = 6\sqrt{2}$. We note that along the outward path the convergence is large- Θ_* convergence is rapid (it is essentially related to the convergence with respect to $\Theta_i = -\Theta_*$ of the one-way protocol), along the return path the curves do not appear to approach a large- Θ_* limit.

tend to be suppressed in the adiabatic $\Upsilon \rightarrow \infty$ limit. We believe that this extreme sensitivity to Θ_* makes also problematic the large- L limit after the limit $\Theta_* \rightarrow \infty$ shown by the numerical data.

Similar results are also obtained for the quantum Kitaev wire, see Fig. 2.16 where we show results for the adiabaticity function and the particle density. In this case the values at the end of the outward way appear quite stable, but the return way is characterized again by large (less regular) oscillations with larger

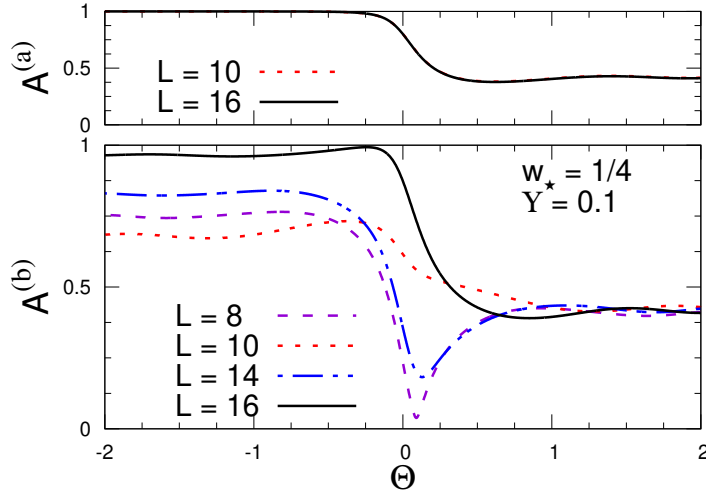


Figure 2.12: The adiabaticity function $A(t, t_s, w_*, L)$ of quantum Ising chains along round-trip protocols, for fixed $\Upsilon = 0.1$ and $w_* = 1/4$, for the outward (top) and return (bottom) branches of the round-trip protocol, versus Θ , for various size L up to $L = 16$.

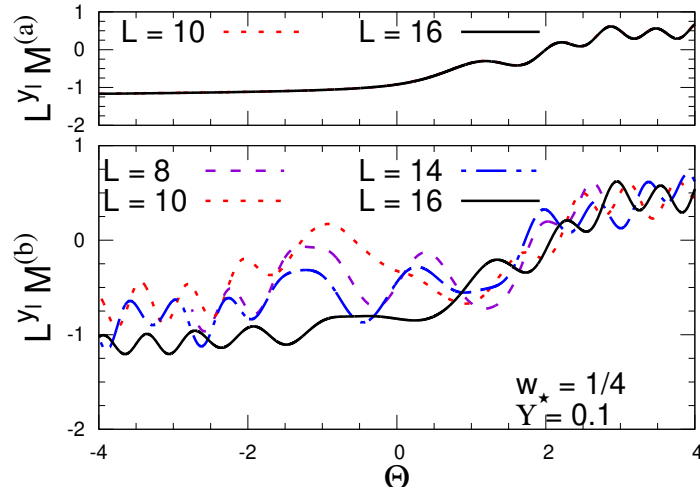


Figure 2.13: The longitudinal magnetization $M(t, t_s, w_*, L)$ along the round-trip protocol, for fixed $w_* = 1/4$, $\Upsilon = 0.1$ for the outward (top) and return (bottom) branches of the round-trip protocol, versus Θ , for various size L up to $L = 16$.

and larger frequencies with increasing Θ_* .

On the basis of the above results, we conclude that in quantum many-body systems the large- Θ_* limit of the dynamic KZ scaling does not apparently exist along the return trajectories, showing similarities with the behavior of two-level model (2.56) subject to round-trip protocols. We believe that this issue deserves further investigation, for example addressing the possibility of obtaining well defined scaling behavior after some average procedures over the oscillations induced by large values of Θ_* , to obtain a well defined large- Θ_* limit.

However, we stress that the dynamic scaling behavior is nicely observed when keeping Θ_* fixed, even along the return trajectory. This is related to the fact that, when keeping Θ_* fixed, the time scaling variable Θ remains finite, therefore the

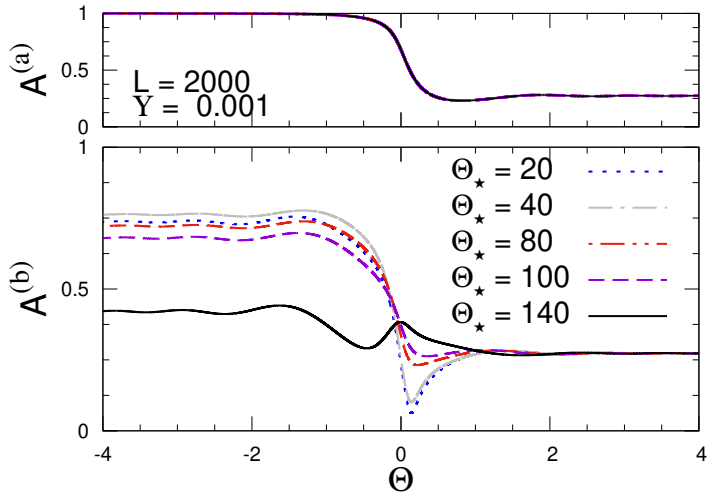


Figure 2.14: The adiabaticity function $A(t, t_s, w_*, L)$ for the quantum Kitaev wire at $L = 2000$ and $\Upsilon = 0.001$ for the outward (top) and return (bottom) branches of the round-trip KZ protocol, versus Θ , for various Θ_* up to $\Theta_* = 140$. We note that along the outward path the convergence is large- Θ_* convergence is rapid (it is essentially related to the convergence with respect to $\Theta_i = -\Theta_*$ in the one-way KZ protocol), along the return path the curves do not appear to approach a large- Θ_* limit.

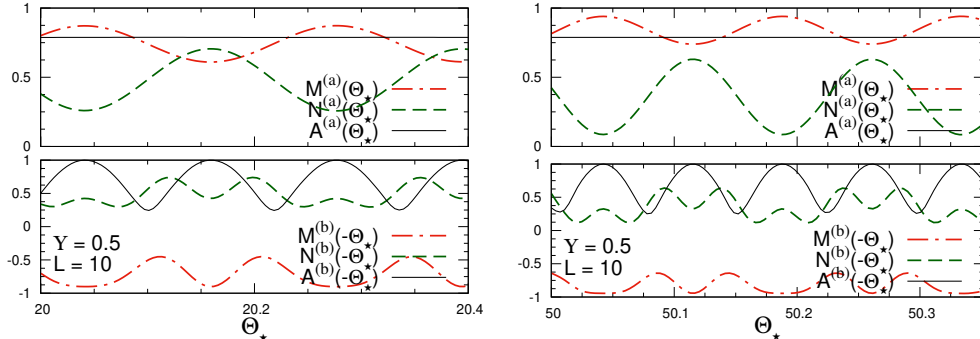


Figure 2.15: Results for M , N and A for fixed $L = 10$, $\Upsilon = 0.5$ versus Θ_* , close to $\Theta_* = 20$ (top figure) and $\Theta_* = 50$ (bottom figure). In each figure, the top plot the values of $M^{(a)}$, $N^{(a)}$ and $A^{(a)}$ at the end of the outward branch, corresponding to $\Theta = \Theta_*$, while the bottom plot shows the values of $M^{(b)}$, $N^{(b)}$ and $A^{(b)}$ at the end of the return branch, corresponding to $\Theta = -\Theta_*$. The comparison of the top and bottom figures show that the oscillations tend to become more frequent with increasing Θ_* (note that the interval of the abscissa is different). Analogous results are obtained for other values of Υ .

time variable is always rescaled consistently with the time scale of the equilibrium quantum transition, provided by the inverse gap at the transition $\Delta \sim L^{-z} \sim \lambda^{-z}$. As a consequence, the the variation of $w(t)$ gets limited within a small interval δ_w around the transition, which becomes smaller and smaller in the large-size limit, as $\delta_w \sim L^{-y_w}$.

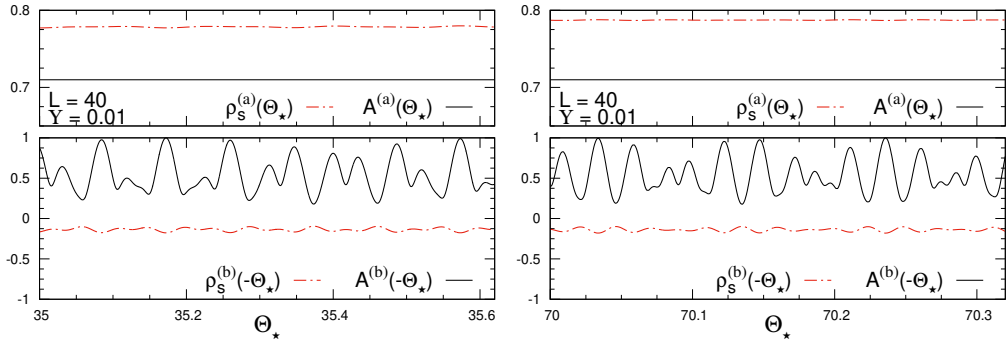


Figure 2.16: Behavior of the subtracted particle density ρ_s , cf. Eq. (2.20), and the adiabaticity function A for the Kitaev wire, for fixed $L = 40$, $\Upsilon = 0.01$ versus Θ_* , close to $\Theta_* = 70$ (bottom figure) and $\Theta_* = 35$ (top figure). In each figure, the top plot the values of $\rho_s^{(a)}$ and $A^{(a)}$ at the end of the outward branch, corresponding to $\Theta = \Theta_*$, while the bottom plot shows the values of $\rho_s^{(b)}$ and $A^{(b)}$ at the end of the return branch, corresponding to $\Theta = -\Theta_*$. Again, the comparison of the top and bottom figures show that the oscillations tend to become more frequent with increasing Θ_* .

2.8 Round-Trip across First-Order Transition

2.8.1 Driving Protocol

As a prototypical quantum many-body system displaying a FOT, we shall consider the one-dimensional Ising model in a tilted magnetic field, whose Hamiltonian reads

$$\hat{H}(h_\perp, h_\parallel) = -J \sum_{j=1}^{L-1} \hat{\sigma}_j^{(3)} \hat{\sigma}_{j+1}^{(3)} - \sum_{j=1}^L (h_\perp \hat{\sigma}_j^{(1)} + h_\parallel \hat{\sigma}_j^{(3)}). \quad (2.58)$$

Here, L is the system size, $\hat{\sigma}_j^{(k=1,2,3)}$ denotes standard Pauli operators acting on site j , h_\perp (resp. h_\parallel) is the transverse (resp. longitudinal) component of the magnetic field and $J = 1$ is the overall energy scale which is set to unit from thereafter.

We set open boundary conditions (OBC) for the spin chain (2.58). Notice that other choices of *neutral* boundary conditions (i.e., not favoring any particular phase) –such as periodic boundary conditions– will not alter our discussion below. The case of non-neutral types of boundary is discussed in Refs. [80, 47, 48, 49, 50, 51].

We briefly recall the phase diagram of the model (2.58), depicted in Fig. 2.17. At $(h_\perp, h_\parallel) = (1, 0)$, the Ising model develops a critical behavior belonging to the 2D Ising universality class, see e.g. [42]. For $h_\parallel \neq 0$ instead, the system is always gapped. Our focus is on the ferromagnetic phase $h_\perp < 1$, where the model undergoes a quantum FOT at $h_\parallel = 0$. Across this FOT point, the model remains non-critical and thus displays exponential decay of correlation functions. Nevertheless, it has been shown that finite-size scaling (FSS) behaviors arise in the limit $L \rightarrow \infty$, $h_\parallel \rightarrow 0^\pm$ [81], as argued below.

For $h_\parallel = 0$, the model (2.58) features a level crossing of the two lowest-energy states in the infinite-volume limit, separated by an exponentially closing energy

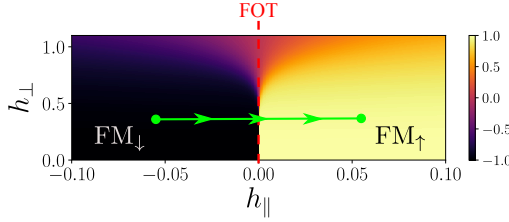


Figure 2.17: Illustration of the phase diagram of the model (2.58) — For $h_\perp < 1$, the ground state is ferromagnetic, i.e., it features a non-vanishing longitudinal magnetization (color map). This ferromagnet is aligned with the direction of h_\parallel (FM $_\downarrow$ and FM $_\uparrow$ phases in the figure). A line of quantum FOTs at $h_\parallel = 0$ separate these two ferromagnetic phases (dashed vertical line). The protocol that will be discussed is a passage across the quantum FOT at fixed $h_\perp < 1$ (green line).

gap for $L \rightarrow \infty$ [82]. For OBC, this is

$$\Delta(h_\perp, L) = 2h_\perp^L(1 - h_\perp^2) \left[1 + \mathcal{O}(h_\perp^{2L}) \right]. \quad (2.59)$$

On the other hand, the presence of a small longitudinal magnetic field $|h_\parallel| \ll 1$ induces a Zeeman-like gap in energy between the two lowest levels, thus introducing another symmetry-breaking mechanism of the aforementioned degeneracy. The latter can be estimated using standard perturbation theory in h_\parallel as [83]

$$\mathcal{E}(h_\perp, h_\parallel, L) \xrightarrow{h_\parallel \rightarrow 0} 2h_\parallel \sum_{j=1}^L \left| \langle \hat{\sigma}_j^{(3)} \rangle \right| \simeq 2h_\parallel L M_0(h_\perp), \quad (2.60)$$

where we approximated the longitudinal magnetization with its value $M_0 = (1 - h_\perp^2)^{1/8}$ attained when $h_\parallel = 0$ and $L = \infty$.

These two effects (2.59)-(2.60) do compete across a quantum FOT (i.e., when $h_\parallel \rightarrow 0^\pm, L \rightarrow \infty$), giving rise to a FSS behavior controlled by the scaling variable $\kappa = \mathcal{E}(h_\perp, h_\parallel, L)/\Delta(h_\perp, L)$ [84, 81]. For instance, the longitudinal magnetization

$$M(h_\perp, h_\parallel, L) = L^{-1} \sum_{j=1}^L \langle \hat{\sigma}_j^{(3)} \rangle \quad (2.61)$$

satisfies the FSS for $h_\parallel \rightarrow 0^\pm, L \rightarrow \infty$ [84, 85]

$$M(h_\perp, h_\parallel, L) \sim M_0(h_\perp) f_M(\kappa). \quad (2.62)$$

Similarly, the energy gap between the two lowest levels $\Delta E(h_\perp, h_\parallel, L) = E_1 - E_0$ obeys the FSS

$$\Delta E(h_\perp, h_\parallel, L) \sim \Delta(h_\perp, L) f_E(\kappa). \quad (2.63)$$

Note that the ground state properties of the model (2.58) across the quantum FOT are entirely controlled by the competition of the two quasi-degenerate vacua. This enables the analytical calculation of the scaling functions f_M, f_E in (2.62)-(2.63) using an effective two-level description (see Appendix A.1 and Refs.[83, 86, 87, 88] for details). The result is

$$f_M(\kappa) = \frac{\kappa}{\sqrt{1 + \kappa^2}}; \quad f_E(\kappa) = \sqrt{1 + \kappa^2}. \quad (2.64)$$

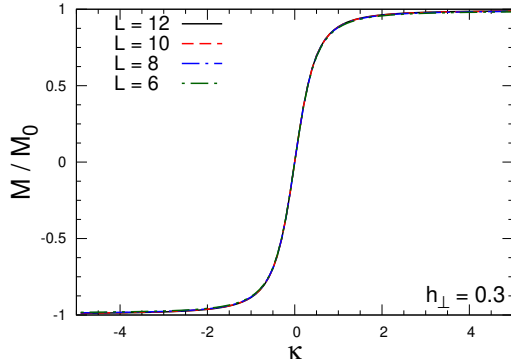


Figure 2.18: FSS of the longitudinal magnetization in Eq. (2.62) – M/M_0 shown as function of the scaling variable κ for different system sizes up to $L = 12$ and $h_\perp = 0.3$. The data collapse to the scaling function f_M in Eq. (2.64).

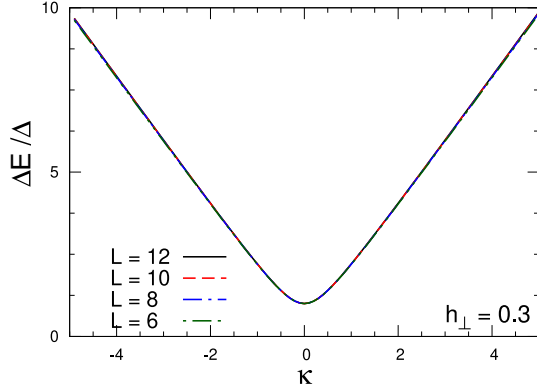


Figure 2.19: FSS of the energy gap in Eq. (2.63) – $\Delta E/\Delta$ shown as function of the scaling variable κ for different system sizes up to $L = 12$ and $h_\perp = 0.3$. The data collapse to the scaling function f_E in Eq. (2.64).

The FSS behavior of Eqs. (2.62)-(2.63) is shown in Figs. 2.18 and 2.19.

In what follows, we investigate the out-of-equilibrium finite-size scaling (OFSS) behaviors arising due to a slowly-varying time-dependent longitudinal magnetic field h_\parallel that drives the system across the quantum FOT at fixed $h_\perp < 1$.

We discuss the case of single- and round-trip passage through the transition, and we comment on the validity of the two-level effective description of the many-body system during the nonequilibrium dynamics.

In our setting, the out-of-equilibrium dynamics is generated at fixed $h_\perp < 1$ by varying h_\parallel in the Ising Hamiltonian (2.58) as a linear ramp in time ¹

$$h_\parallel(t) = t/t_s, \quad (2.65)$$

where t_s is a characteristic time scale. With this convention, the model is prepared at $t_i < 0$ in the many-body ground state $|\Psi(t_i)\rangle = |\Psi_0[h_\parallel(t_i)]\rangle$ corresponding to the initial value of longitudinal field $h_\parallel = t_i/t_s$. At times $t > t_i$, the system evolves unitarily with time-dependent Ising Hamiltonian

$$i\partial_t |\Psi(t)\rangle = \hat{H}(h_\perp < 1, t/t_s) |\Psi(t)\rangle, \quad (2.66)$$

¹The case of a non-linear driving $h_\parallel(t) = (t/t_s)^r$ with odd exponent r can be obtained straightforwardly, see e.g. Ref. [24].

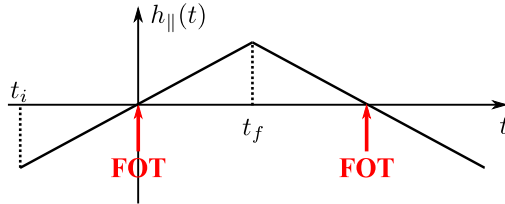


Figure 2.20: Illustration of the driving protocol: the longitudinal magnetic field $h_{\parallel}(t)$ is varied as a linear ramp (2.65) from a time $t_i < 0$ to a time $t_f > 0$ with slope t_s^{-1} . With this convention, the system is driven across the quantum FOT at $t = 0$. For a round-trip passage, the ramp is inverted at $t = t_f$ so that we can drive the system back to the value $h_{\parallel}(t_i)$ in a time-window $2(t_f - t_i)$, see Fig. 2.20 for an illustration.

crossing the quantum FOT when $t = 0$. A single-passage protocol stops at a final time $t_f > 0$ while a round-trip protocol is implemented by inverting the ramp (2.65) at $t = t_f$ so that we can drive the system back to the value $h_{\parallel}(t_i)$ in a time-window $2(t_f - t_i)$, see Fig. 2.20 for an illustration.

2.8.2 Finite Size Scaling at FOQT

Below, we specify to the case of slow drivings, $t_s \rightarrow \infty$. For a single passage and at the critical point ($h_{\perp} = 1$), this class of protocols would correspond to the standard Kibble-Zurek setup, whose OFSS has been extensively discussed in literature, see e.g. Refs. [70, 69, 52, 89, 90, 21, 91, 92, 93, 94, 25, 23, 95, 96] and [24, 53] for reviews. We also mention recent works e.g. [97, 98, 99] on the complete probability distribution of topological defects.

Analogously, across the quantum FOT ($h_{\perp} < 1, h_{\parallel} = 0$), one can formulate an OFSS ansatz as the limit $L \rightarrow \infty$, $u \equiv t_s L^{-1} M_0^{-1} \rightarrow \infty$ with fixed scaling variables:

$$\tau = t/\sqrt{u}; \quad (2.67)$$

$$v = u \Delta(h_{\perp}, L)^2, \quad (2.68)$$

where the longitudinal magnetization is expected to scale as

$$M(h_{\perp}, t, t_s, L) \sim M_0(h_{\perp}) \mathcal{F}_M(\tau, v) \quad (2.69)$$

with OFSS function \mathcal{F}_M .

In Eq. (2.67), τ is a rescaled time and $t_{\text{KZ}} = \sqrt{u}$ plays the role of a Kibble-Zurek time, as commented in the following section. Similar relations arise at classical FOT, see e.g. Refs. [77, 100]. In this sense, we expect to assist to a breakdown of adiabaticity when $|\tau| \lesssim 1$. To quantitatively probe this effect during the driving, it is useful to introduce the *adiabaticity function*

$$A(h_{\perp}, t, t_s, L) = \left| \langle \Psi_0[h_{\parallel}(t)] | \Psi(t) \rangle \right|, \quad (2.70)$$

defined as the modulus of the overlap coefficient between the time-evolved wavefunction $|\Psi(t)\rangle$ and the instantaneous ground state $|\Psi_0[h_{\parallel}(t)]\rangle$ of the time-dependent

Hamiltonian $\hat{H}(h_\perp, t/t_s)$. Initially, $A(t_i) = 1$ by construction, and it deviates from unit when the adiabatic approximation of the state $|\Psi(t)\rangle$ breaks down near the quantum FOT point. In the OFSS limit,

$$A(h_\perp, t, t_s, L) \sim \mathcal{F}_A(\tau, v). \quad (2.71)$$

Finally, notice that the scaling variable κ (characterizing the equilibrium FSS) is obtained from (2.67)-(2.68) as

$$\kappa = \frac{2\tau}{\sqrt{v}}. \quad (2.72)$$

It is then easy to see that the energy gap

$$\Delta E(h_\perp, t, t_s, L) \sim \Delta(h_\perp, L) f_E \left(\frac{2\tau}{\sqrt{v}} \right) \quad (2.73)$$

in the OFSS limit.

In Figs. 2.21 and 2.22, we show the results for the OFSS of the longitudinal magnetization (Eq. (2.69)) and of the adiabaticity function (Eq. (2.71)). The numerical data is obtained by performing exact diagonalization of the spin chain (2.58) and Runge-Kutta methods for time evolution. Notice that despite our data are obtained for spin chains of modest system sizes, the convergence to the thermodynamic limit is controlled by the interplay of h_\perp and L , and thus it can be reached already for modest system sizes when $h_\perp \ll 1$. For h_\perp closer to one, larger values of L are required to observe OFSS, see Ref. [83, 84]. The convergence to the OFSS regime is shown in Fig. 2.23 for different values of L and h_\perp .

The OFSS for a single passage across the quantum FOT has been discussed e.g. in Refs. [101, 102, 103, 104, 105, 73]. Here, we show that such scaling behavior remains valid for a round-trip passage. It is important to remark that the OFSS during a round-trip protocol cannot be inferred from the observed OFSS for a single passage. Indeed, while the first passage is responsible for the formation of excitations from the adiabatic ground state in the Kibble-Zurek sense, for $t > t_f$ the system is found in a nonequilibrium state before approaching the transition for the second time. Therefore, standard Kibble-Zurek arguments do not apply.

Interestingly, the OFSS during the round-trip protocol shows a dependence on the initial condition τ_i , see Figs. 2.24 and 2.25. Such feature arises due to the magnetic field inversion occurring at $t = t_f$ i.e. when the system is already far from equilibrium and thus unable to wash out such information during the unitary evolution for $t > t_f$. This is a qualitative difference with respect to the single passage protocol. Given the dependence on τ_i , we refer to the OFSS functions \mathcal{F}_M and \mathcal{F}_A for the round trip as *quasi-universal*.

In the following sections, we derive an effective description of the many-body system during the driving protocol (2.65). In this way, we determine analytical expressions for the quasi-universal OFSS functions characterizing the round-trip protocol.

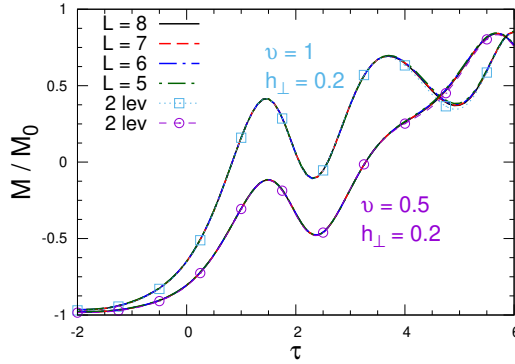


Figure 2.21: OFSS of the longitudinal magnetization in Eq. (2.69) — $M(t)/M_0$ shown as a function of the rescaled time τ during a round-trip protocol with $|\tau_i| = \tau_f = 2$ (FOTs at $\tau = 0, 4$). We show different values of v and h_\perp (different curves) and we vary the system sizes up to $L = 8$. In the plot legend, ‘2 lev’ refers to the scaling functions $\mathcal{F}_M(\tau, v)$ obtained using the effective two-level description discussed in Sec. 2.8.3.

2.8.3 Effettive Description

Let us consider the following formal expansion of the many-body wavefunction

$$|\Psi(t)\rangle = \sum_{n=0}^{2^L} C_n(t) e^{-i\vartheta_n(t)} |\psi_n(t)\rangle \quad (2.74)$$

where $|\psi_n(t)\rangle$ is the instantaneous eigenbasis of the Hamiltonian at fixed time t satisfying

$$\hat{H}(t) |\psi_n(t)\rangle = E_n(t) |\psi_n(t)\rangle, \quad (2.75)$$

and

$$\vartheta_n(t) = \int_{t_0}^t ds E_n(s) \quad (2.76)$$

is the associated dynamical phase. Using (2.74), the time evolution generated by the Schrödinger equation (2.66) can be reduced to the set of equations for the overlap coefficients

$$\frac{dC_k}{dt} = - \sum_n C_n(t) \langle \psi_k(t) | \left| \frac{\partial \psi_n(t)}{\partial t} \right\rangle e^{i(\vartheta_n(t) - \vartheta_k(t))}, \quad (2.77)$$

which is solved imposing the initial condition $C_k(t_i) = \delta_{0,k}$. Differentiating Eq. (2.75), one obtains

$$\begin{aligned} & \langle \psi_m(t) | \partial_t \hat{H} | \psi_n(t) \rangle \\ & + (E_m(t) - E_n(t)) \langle \psi_m(t) | \left| \frac{\partial \psi_n(t)}{\partial t} \right\rangle = \frac{dE_m}{dt} \delta_{m,n} \end{aligned} \quad (2.78)$$

from which one can write Eq. (2.77) as

$$\begin{aligned} \frac{dC_k(t)}{dt} &= - \langle \psi_k(t) | \left| \frac{\partial \psi_k(t)}{\partial t} \right\rangle C_k(t) \\ &+ \sum_{n \neq k} C_n(t) \frac{\langle \psi_k(t) | \partial_t \hat{H} | \psi_n(t) \rangle}{(E_n(t) - E_k(t))} e^{i(\vartheta_n(t) - \vartheta_k(t))}. \end{aligned} \quad (2.79)$$

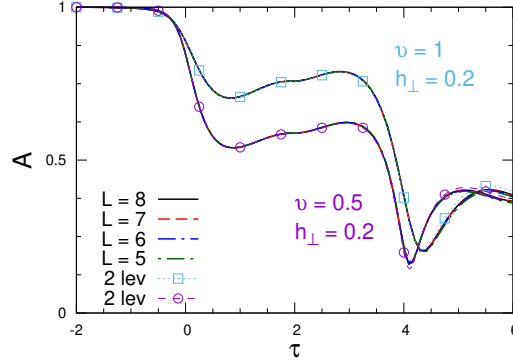


Figure 2.22: OFSS of the adiabaticity function in Eq. (2.71) — $A(t)$ shown as a function of the rescaled time τ during a round-trip protocol with $|\tau_i| = \tau_f = 2$ (FOTs at $\tau = 0, 4$). We show different values of v and h_{\perp} (different curves) and we vary the system size up to $L = 8$. In the plot legend, ‘2 lev’ refers to the scaling functions $\mathcal{F}_A(\tau, v)$ obtained using the effective two-level description discussed in Sec. 2.8.3.

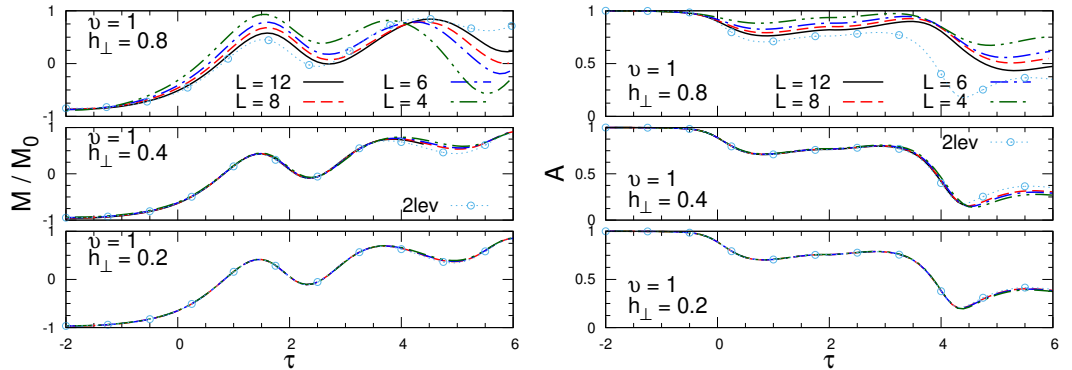


Figure 2.23: Convergence to the OFSS regime – Top: Longitudinal magnetization $M(t)/M_0$; Bottom: adiabaticity function $A(t)$, both shown for different L and h_{\perp} as function of the rescaled time τ during a round-trip protocol with $|\tau_i| = \tau_f = 2$ and $v = 1$. The symbols show the scaling functions \mathcal{F}_M , \mathcal{F}_A obtained using the effective two-level description discussed in Sec. 2.8.3.

This formal expression for the coefficients is exact. Specifying it to the Ising Hamiltonian (2.58) with ramp (2.65), we have

$$\frac{\langle \psi_k(t) | \partial_t \hat{H} | \psi_n(t) \rangle}{(E_n(t) - E_k(t))} = \frac{M_{k,n}(t)}{t_s L^{-1} (E_n(t) - E_k(t))}, \quad (2.80)$$

where $M_{k,n}(t) = L^{-1} \langle \psi_k(t) | \sum_{j=1}^L \hat{\sigma}_j^{(3)} | \psi_n(t) \rangle$.

The adiabatic limit corresponds to the limit $t_s \rightarrow \infty$ (regardless the value of L). In such limit the off-diagonal terms in Eq. (2.79) vanish and the system remains in the adiabatic ground state with $h_{\parallel}(t)$ at any time t . Conversely, in the OFSS limit considered, a breakdown of the adiabatic approximation is observed (cf Fig. 2.22). In particular, it is easy to show that the contribution coming from the first excited level is non-negligible since

$$t_s L^{-1} (E_1(t) - E_0(t)) \sim \sqrt{u v} M_0 f_E(\kappa) \quad (2.81)$$

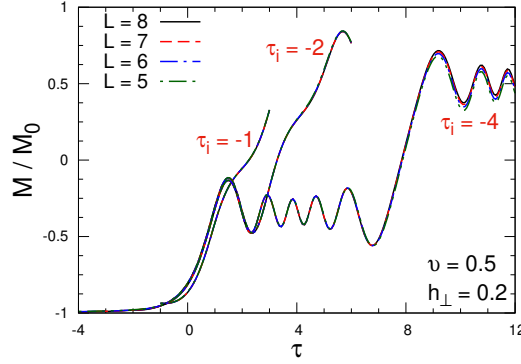


Figure 2.24: Quasi-universality of the OFSS behavior of M/M_0 during a round trip protocol. We show the data collapse as function of τ at fixed $v = 0.5$, $h_\perp = 0.2$, and varying the system size up to $L = 8$. Different curves refer to different values of $|\tau_i| = \tau_f$ (see legend).

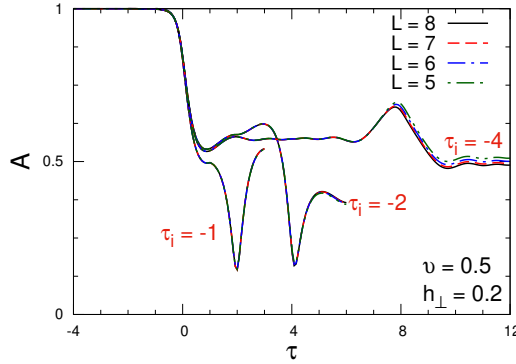


Figure 2.25: Quasi-universality of the OFSS behavior of A during a round trip protocol. We show the data collapse as function of τ at fixed $v = 0.5$, $h_\perp = 0.2$, and varying the system size up to $L = 8$. Different curves refer to different values of $|\tau_i| = \tau_f$ (see legend).

and v is fixed in the OFSS regime. This means that the time scale of the transition to the first excited level is of the order of $t_{\text{KZ}} = \sqrt{u}$, and it starts to be populated at rescaled times $\tau \sim \mathcal{O}(1)$, in agreement with the OFSS arguments above and with the numerical results of figures 2.21, 2.22.

Higher energy levels are not expected to contribute to the early stages of the nonequilibrium dynamics as we now argue. In the OFSS regime, we can approximate the energy gaps for $n \geq 2$ as

$$E_n(t) - E_0(t) \approx (E_n - E_0)|_{h_\parallel=0} \quad (2.82)$$

since the presence of a weak longitudinal field do not significantly alter higher excited levels. Considering that,

$$(E_n - E_0)|_{h_\parallel=0} \geq (E_2 - E_0)|_{h_\parallel=0} = 2(1 - h_\perp) + \mathcal{O}(L^{-2}) \quad (2.83)$$

for OBC [82], and that $E_n - E_1 \simeq E_n - E_0$ up to exponentially small corrections in L , we conclude that OFSS regime is restricted within the Hilbert space spanned by

the two lowest levels of the Hamiltonian, up to large-time corrections that occur at rescaled times of order $\tau \sim O(t_{\text{KZ}})$.

In order to further check the validity of this argument, we introduce the quantity

$$B(h_\perp, t, t_s, L) = \left| \langle \Psi_1[h_\parallel(t)] \rangle \Psi(t) \right|, \quad (2.84)$$

where $|\Psi_1[h_\parallel(t)]\rangle$ is the instantaneous first excited state associated with the Hamiltonian $\hat{H}(h_\perp, t/t_s)$ in (2.58). Alongside with the adiabaticity function (2.70), the time evolution of $B(t)$ is able to probe the validity of the two-level approximation during the driving. In this sense, introducing *totality function*

$$T(t) = \sqrt{A^2(t) + B^2(t)}, \quad (2.85)$$

the distance variable

$$D(t) = 1 - T(t) \quad (2.86)$$

gives an estimate of the error arising from the projection of the many-body state $|\Psi(t)\rangle$ onto a two-dimensional Hilbert space spanned by $\{|\Psi_0[h_\parallel(t)]\rangle; |\Psi_1[h_\parallel(t)]\rangle\}$. In particular, the closer $D(t)$ is to zero, the more accurate the two-level approximation is.

The time evolution of $D(t)$ for the driving of Figs. 2.21,2.22 is shown in Fig. 2.26. As one can see, the distance $D(t)$ remains extremely close to zero during the whole driving. In Fig. 2.27, we show the time evolution of the functions $A(t)$ and $B(t)$, which undergo (as expected) a non-trivial dynamics characterized by a breakdown of adiabaticity close to the quantum FOT.

Motivated by this evidence, in the next section we develop a two-level effective description of the dynamics to determine the OFSS functions \mathcal{F}_M , \mathcal{F}_A appearing in Eqs. (2.69),(2.71).

Two-level model

By projecting the Ising Hamiltonian (2.58) onto the two-dimensional Hilbert space spanned by $\{|\Psi_0[h_\parallel(t)]\rangle; |\Psi_1[h_\parallel(t)]\rangle\}$, we obtain (up to an unimportant energy shift) the following effective two-level model

$$\hat{H}_{\text{eff}}(t) = \frac{1}{2} (\Delta(h_\perp, L) \hat{\sigma}^{(1)} - \mathcal{E}(h_\perp, t, t_s, L) \hat{\sigma}^{(3)}), \quad (2.87)$$

with \mathcal{E} given by Eq. (2.60) with longitudinal field (2.65). Here, we choose the basis $\{|\psi_0\rangle, |\psi_1\rangle\}$ such that $\mathcal{E}\hat{\sigma}^{(3)}$ is the perturbation induced by h_\parallel , and the off-diagonal terms encode the gap (2.59) between the two quasi-degenerate levels at finite sizes [83]. Higher order perturbative effects in h_\perp generating large bubbles of true vacuum onto the metastable state can be studied using a multi-level effective model, see Ref. [102] for details. Notice that Eq. (2.87) is equivalent to truncate the expansion of the many-body wavefunction in the instantaneous eigenbasis (2.74) with the two lowest overlap coefficients

$$\begin{aligned} |\Psi(t)\rangle &= C_0(t) |\Psi_0[h_\parallel(t)]\rangle + C_1(t) |\Psi_1[h_\parallel(t)]\rangle + \mathcal{O}(t_{\text{KZ}}^{-2}) \\ &= c_0(t) |\psi_0\rangle + c_1(t) |\psi_1\rangle + \mathcal{O}(t_{\text{KZ}}^{-2}), \end{aligned} \quad (2.88)$$

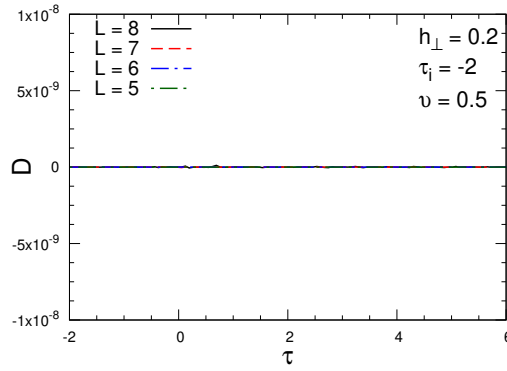


Figure 2.26: OFSS of the function $D(t)$ as a function of the rescaled time τ during a round-trip protocol with $|\tau_i| = \tau_f = 2$ (FOTs at $\tau = 0, 4$). We set $v = 0.5$, $h_\perp = 0.2$ and different system sizes up to $L = 8$.

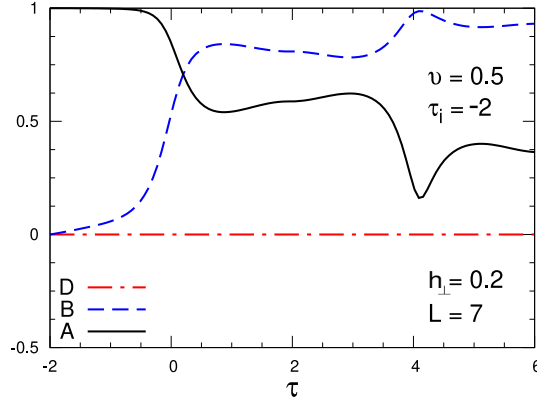


Figure 2.27: Behavior of $A(t)$, $B(t)$ and $D(t)$ as function of the rescaled time τ for a fixed system size $L = 7$ during a round-trip protocol with $|\tau_i| = \tau_f = 2$ (FOTs at $\tau = 0, 4$). We set $v = 0.5$ and $h_\perp = 0.2$.

since $|\psi_{0,1}\rangle \simeq |\Psi_{0,1}[h_\parallel(t_0)]\rangle$ for $|t_0| \gg 1$. The two sets of coefficients are then related via the rotation

$$\begin{pmatrix} C_0(t) \\ C_1(t) \end{pmatrix} = \begin{pmatrix} \cos(\alpha/2) & -\sin(\alpha/2) \\ \sin(\alpha/2) & \cos(\alpha/2) \end{pmatrix} \begin{pmatrix} c_0(t) \\ c_1(t) \end{pmatrix} \quad (2.89)$$

with angle $\alpha = \arctan(\frac{\sqrt{v}}{2\tau})$ (cf Eq. (2.72) and Appendix A.1).

Under this approximation, Eq. (2.77) reduces to a finite-time Landau-Zener-Stückelberg (LZS) problem in the interval $t \in [t_i, t_f]$ [106, 78]

$$i \frac{d}{dt} \begin{pmatrix} c_0(t) \\ c_1(t) \end{pmatrix} = \frac{1}{2} \begin{pmatrix} -\mathcal{E}(t) & \Delta \\ \Delta & \mathcal{E}(t) \end{pmatrix} \begin{pmatrix} c_0(t) \\ c_1(t) \end{pmatrix}. \quad (2.90)$$

In terms of the OFSS variables (2.67)-(2.68),

$$i \frac{d}{d\tau} \begin{pmatrix} c_0(\tau, v) \\ c_1(\tau, v) \end{pmatrix} = \begin{pmatrix} -\tau & \frac{\sqrt{v}}{2} \\ \frac{\sqrt{v}}{2} & \tau \end{pmatrix} \begin{pmatrix} c_0(\tau, v) \\ c_1(\tau, v) \end{pmatrix}, \quad (2.91)$$

which can be solved imposing that $(c_0(\tau_i, v); c_1(\tau_i, v)) = (1; 0)$, see Appendix A.2 for details on the calculation. We write the result in terms of the 2×2 hermitian

matrix $U(\tau, \tau_i)$:

$$\begin{pmatrix} c_0(\tau) \\ c_1(\tau) \end{pmatrix} = U(\tau, \tau_i) \begin{pmatrix} 1 \\ 0 \end{pmatrix} \quad (2.92)$$

from which the OFSS functions in Eqs. (2.69),(2.71) during a single-passage protocol are obtained as [101]

$$\begin{aligned} \mathcal{F}_M(\tau, v) &= 2|c_1(\tau, v)|^2 - 1 \\ &= \frac{v}{4} e^{-\frac{\pi v}{16}} |\mathcal{D}_{-1+\frac{iv}{8}}(\sqrt{2}e^{i\frac{3\pi}{4}}\tau)|^2 - 1 \end{aligned} \quad (2.93)$$

$$\begin{aligned} \mathcal{F}_A(\tau, v) &= |C_0(\tau, v)| \\ &= e^{-\frac{\pi v}{32}} \left| \sqrt{\frac{1}{2} + \frac{|\tau|}{\sqrt{4\tau^2 + v}}} \mathcal{D}_{\frac{iu}{8}}(\sqrt{2}e^{i\frac{3\pi}{4}}\tau) \right. \\ &\quad \left. - \frac{\sqrt{v}e^{-\frac{i\pi}{4}}}{2\sqrt{2}} \sqrt{\frac{1}{2} - \frac{|\tau|}{\sqrt{4\tau^2 + v}}} \mathcal{D}_{-1+\frac{iu}{8}}(\sqrt{2}e^{i\frac{3\pi}{4}}\tau) \right| \end{aligned} \quad (2.94)$$

and similarly for other quantities. Here, $\mathcal{D}_\nu(z)$ denotes the Parabolic Cylinder function.

For the round-trip protocol, we can solve the associated Lzs problem in the time window $t \in [t_f, 2t_f + |t_i|]$ obtaining:

$$\begin{pmatrix} c_0(\tau) \\ c_1(\tau) \end{pmatrix} = \tilde{U}(\tau, \tau_f) U(\tau_f, \tau_i) \begin{pmatrix} 1 \\ 0 \end{pmatrix}, \quad (2.95)$$

where $\tilde{U}(\tau, \tau_f)$ is the evolution matrix with inverted time ramp (2.65), see Appendix A.2 for the analytical expression of its elements. From (2.95), the OFSS functions during the round-trip protocol are straightforwardly obtained as $\mathcal{F}_M = 2|c_1(\tau, v)|^2 - 1$ and $\mathcal{F}_A = |C_0(\tau, v)|$ respectively, although their analytical expression is cumbersome and therefore deferred to Appendix A.2. The important outcome of their calculation is that they display a non-trivial dependence on τ_i , in contrast with (2.93)-(2.94) obtained for a single passage (cf. Figs. 2.24-2.25).

In Figs. 2.21-2.22, the OFSS functions obtained from the solution of the Lzs problem are plotted as dashed lines against the rescaled numerical data for the Ising model (2.58), showing an overall excellent agreement. Small deviations from the OFSS functions computed in the two-level approximation go monotonically to zero on increasing $t_{KZ} = \sqrt{u}$, see Figs. 2.28 -2.29.

In these plots, our numerical analysis reveals a convergence to the OFSS behavior which is compatible with a power-law in \sqrt{u} . Further investigations on this aspect go beyond the scope of this work and thus are delivered to subsequent studies.

Breakdown of the effective description

In this section, we show the breakdown of the OFSS regime (and consequently of the two-level effective description) discussed in Sec. 2.8.2.

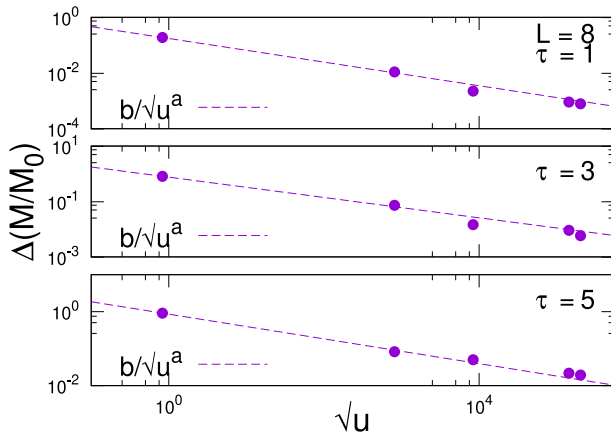


Figure 2.28: Convergence to the OFSS of the longitudinal magnetization — Symbols show the quantity $\Delta(M/M_0) = |M/M_0 - \mathcal{F}_M|$ for fixed $L = 8$, $v = 0.5$, $|\tau_i| = \tau_f = 2$ (FOTs at $\tau = 0, 4$) and for different values of $\tau = 1, 3, 5$ (different panels) as function of \sqrt{u} . Dashed line: power-law ansatz $f(u) = b/(\sqrt{u})^a$ with parameters a, b extracted from a fit of the numerical data.

As argued in Sec. 2.8.3, the OFSS regime is able to capture the nonequilibrium dynamics arising by a slow driving across the quantum FOT for a time window where the dynamics involves the lowest two energy levels only. Corrections to the scaling behavior are expected when $\tau \sim \mathcal{O}(t_{\text{KZ}})$. This is shown in Fig. 2.31 for the adiabaticity function and in Fig. 2.30 for the distance measure. Here, $v = 0.01$ and $t_{\text{KZ}} \simeq 1.29$ for our choice of parameters, and we see that $D(\tau > t_{\text{KZ}}) \neq 0$, as expected. For other choice of parameters such that $v \sim \mathcal{O}(1)$ and $t_{\text{KZ}} \gg 1$, we would observe the same qualitative behavior but occurring at larger time scales (cf. Eq. (2.81)).

2.8.4 Floquet Driving

As a natural extension of our setup, one can consider a Floquet driving of the Ising model (2.58) across the quantum FOT, realized by a periodic repetition of the round-trip protocol discussed above. For sake of simplicity, we focus on the symmetric case $|t_i| = t_f \equiv t_0$ with time ramp

$$h_{\parallel}(t \bmod 4t_0) = \begin{cases} t/t_s, & t \in [-t_0, t_0]; \\ (2t_0 - t)/t_s, & t \in [t_0, 3t_0]. \end{cases} \quad (2.96)$$

Based on the arguments of Sec. 2.8.3, the validity of the two-level approximation is controlled by the energy injected in the model during the driving (and thus by the total duration of the protocol) rather than on the number of passages across the quantum FOT.

Therefore, we test the OFSS relations of Eqs. (2.69), (2.71) during the Floquet driving (2.96) of the Ising Hamiltonian (2.58). The results are shown in Fig. 2.32, with OFSS functions computed by repeatedly applying the LZS solution (2.95) outlined in Sec. 2.8.3. The figures show a good data collapse for different values of the system's parameters, with deviations from the OFSS functions (dashed lines)

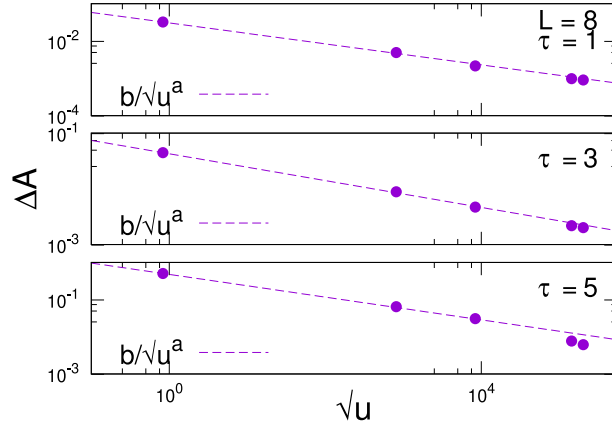


Figure 2.29: Convergence to the OFSS of the adiabaticity function — Symbols show the quantity $\Delta A = |A - \mathcal{F}_A|$ for fixed $L = 8$, $v = 0.5$, $|\tau_i| = \tau_f = 2$ (FOTs at $\tau = 0, 4$) and for different values of $\tau = 1, 3, 5$ (different panels) as function of \sqrt{u} . Dashed line: power-law ansatz $f(u) = b/(\sqrt{u})^a$ with parameters a, b extracted from a fit of the numerical data.

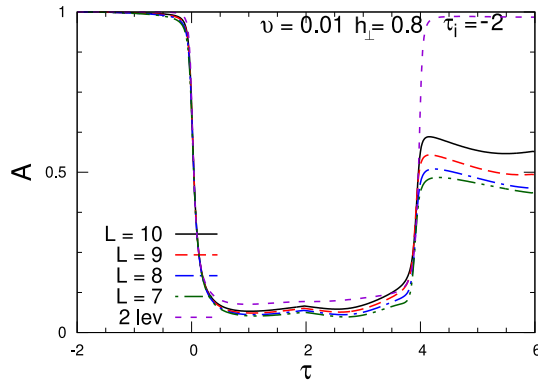


Figure 2.30: Adiabaticity function as a function of the rescaled time τ during a round-trip protocol with $|\tau_i| = \tau_f = 2$ (FOTs at $\tau = 0, 4$). We set $v = 0.01$ and $h_{\perp} = 0.8$ and we vary the system size up to $L = 10$. The dashed line shows the scaling function $\mathcal{F}_A(\tau, v)$ for the effective two-level model (see Sec. 2.8.3).

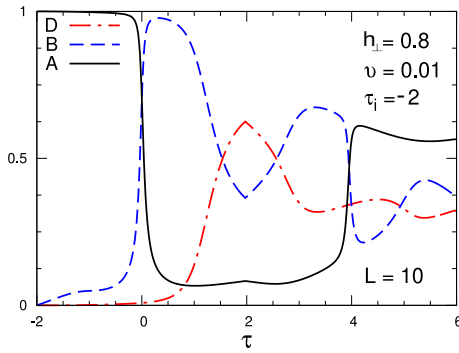


Figure 2.31: Behavior of $A(t)$, $B(t)$ and $D(t)$ as function of the rescaled time τ for a fixed system size $L = 10$ during a round-trip protocol with $|\tau_i| = \tau_f = 2$ (FOTs at $\tau = 0, 4$). We set $v = 0.01$ and $h_{\perp} = 0.8$.

that increase with time. This behavior is compatible with the non-uniform convergence to the OFSS regime with time (i.e., larger values of τ require larger values

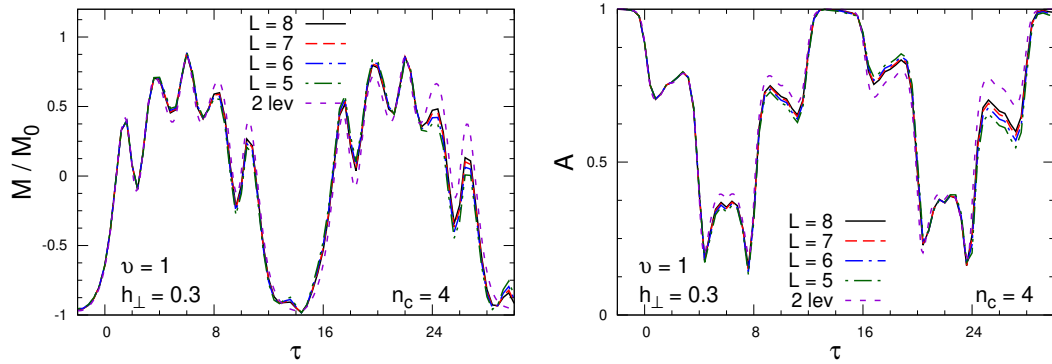


Figure 2.32: OFSS during a Floquet driving of the Ising model (2.58) across the quantum FOT (top – M/M_0 ; bottom – A) as function of the rescaled time τ . We set $\tau_0 = 2$ ($n_c = 4$ round-trip cycles), $v = 1$, $h_{\perp} = 0.3$, and we vary the system size up to $L = 8$. Dashed lines show the OFSS functions computed using the solution of the LZS problem (2.95).

of u), discussed in Sec. 2.8.3 and Sec. 2.8.3.

We also notice that the system is driven extremely close to its initial state at time $\tau_{\text{rec}} \simeq 14$ for our choice of parameters (corresponding to a two periods driving). Interestingly, this recurrence time is independent on the system size in terms of the OFSS variables. For $\tau > \tau_{\text{rec}}$, the pattern for the nonequilibrium dynamics of the quantities in Fig. 2.32 is repeated. This means that if we choose a sufficiently large (but finite) value of t_{KZ} , the two-level effective model of Sec. 2.8.3 can provide a quite accurate description of the many-body system at any stage during the periodic driving.

Finally, it is interesting to consider the evolution after n periods, i.e., to look at the time-evolved wavefunction at stroboscopic times $t_n = t_0(4n - 1)$. In the two-level approximation, this is given by

$$|\Psi(t_n)\rangle \approx \left[(U_F)^n \begin{pmatrix} 1 \\ 0 \end{pmatrix} \right]^T \begin{pmatrix} |\Psi_0[h_{\parallel}(t_0)]\rangle \\ |\Psi_1[h_{\parallel}(t_0)]\rangle \end{pmatrix}, \quad (2.97)$$

with Floquet evolution matrix $U_F = \tilde{U}(3\tau_0, \tau_0) U(\tau_0, -\tau_0)$.

In Fig. 2.33, we show the results for $M(t_n)$ and $A(t_n)$, for a time window of $n = 10$ periods. By comparing our numerical data with the two-level prediction (filled symbols), we observe an excellent agreement during the whole driving. In particular, we see that the convergence of our numerical data for the many-body system to the two-level prediction improves for fixed v and L on decreasing h_{\perp} (i.e., on increasing the time scale t_s), as expected from the scaling arguments of Sec. 2.8.2 and Sec. 2.8.3. This is also confirmed by the curves obtained for $v = 0.05$ and $h_{\perp} = 0.4$ (square symbols), for which the value of t_{KZ} is much smaller. Accordingly, the curves initially show a good agreement with the OFSS theory but, for $n \gtrsim 8$, they significantly deviates from the OFSS functions.

Notice also that the numerical analysis of Fig. 2.33 clearly shows a two-period

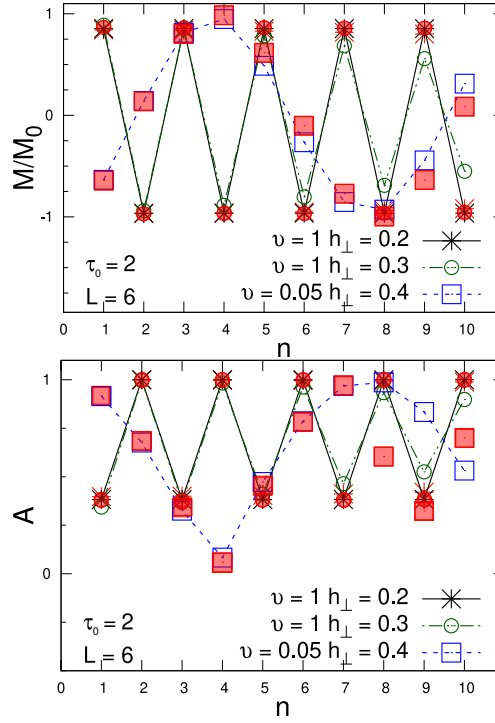


Figure 2.33: Stroboscopic evolution of M/M_0 (top) and of A (bottom) as function of n (corresponding to times $t = t_0(4n - 1)$) at fixed $L = 6$, $\tau_0 = 2$, and for three different values of v , h_{\perp} (different symbols)

. For each set of parameters, the filled symbols show the stroboscopic evolution in the two-level approximation.

recurrence for both the longitudinal magnetization and the adiabaticity function. Such a peculiar behavior of the OFSS regime can be analytically investigated in the two-level approximation. Using the matrix elements of Appendix A.2, it is easy to show that the equation

$$(U_F(\tau_0, v))^n = \pm \text{Id} , \quad (2.98)$$

has solution for $n = 2$, $v = 1$ when $\tau_0 = 2$, in agreement with what observed in Figs. 2.32 and 2.33. In general, there exists a series of exceptional values of $\tau_0 = \tau_*(n, v)$ for which the system shows recurrence after n periods, see Fig. 2.34. For instance, $\tau_*(1, 1) \simeq 1.4$ for one round-trip protocol. Surprisingly, this means that the phases $\Phi(\tau_0, v)$ conferring to the system a non-trivial dependence on τ_0 (see Appendix A.2) can combine for some special values $\tau_0 = \tau_*(n, v)$ to restore the initial state of the system after n periods. In this perspective, the aforementioned quasi-universality of OFSS regime can be exploited to engineer shortcuts to adiabaticity.

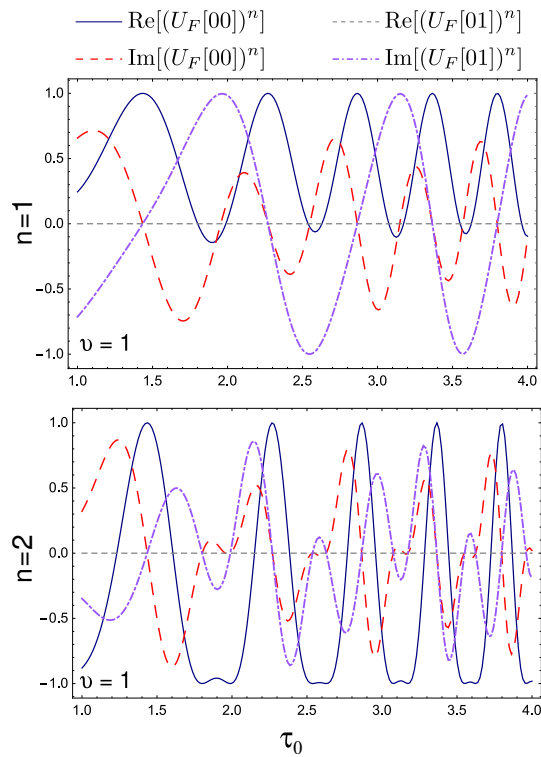


Figure 2.34: Matrix elements of $(U_F(\tau_0, v))^n$ as function of τ_0 , obtained from the analytical results of Appendix A.2. In the panels, we set $v = 1$ and $n = 1$ (top), $n = 2$ (bottom).

Chapter 3

Dissipation

3.1 Introduction

The analysis of open quantum many-body systems plays an important role in fundamental problems of quantum physics, such as quantum information, quantum computing, decoherence and condensed matter physics. The recent progress in the experimental techniques and the realizations of physical devices for quantum computing gives a further motivation to understand the general behavior of these open quantum systems. They involve a wide class of different specific issues as the study of the non-equilibrium steady state (NESS), the effects of a thermal baths, quantum optics, strongly coupled baths, ...etc. In particular, in this discussion we focus on the effects of a dissipative process arising from the weakly interaction with Markovian baths. These dissipative mechanisms may lead to emergence of a new collective phenomena which can change completely the physical behavior of the system. In the condition of complete positivity and trace preserving of a dynamical time-evolution map, we can describe the matrix density of the open system using the Lindblad master equation. This equation describes a non-unitary time evolution which provides the dissipative behavior of the observables defined on the system.

We analyze the dynamic evolution close to a quantum phase transition. In fact, the quantum phase transitions, separating different phases of the system, present universal quantum critical behaviors, which are independent of the local details of the system. They describe the properties of the low-energy spectrum of the system and they show a non-analytical behavior of the ground state, when the size L^d of the system goes to $+\infty$ (thermodynamic limit). However, the finite-size effects provide a finite size scaling (FSS) framework in which, approaching the transition point, the observables satisfy peculiar FSS laws. These law characterize the quantum transition giving us a possible way to compare the analytical theory with the results obtained by computational method. We can extend this theory also to dynamical process aring from coherent drivings, as the quench of the Hamiltonian parameters. In these situations, we can provide a dynamic FSS which controls all the out-of-equilibrium regime close to the transitions point. The following step is to understand how a dissipative process drives the system localized near the transition point and how it changes the dynamic FSS. The answer is given for systems in the presence of a homogeneous local dissipation at continuous quantum transition (CQT) [107] and first-order quantum transition (FOQT) [108] in which emerges

a new dynamic scaling behavior. However, such a dynamic scaling limit requires a particular tuning of the dissipative interactions so that we have a competition between the critical and the dissipative regime.

Instead, in the case of dissipative boundaries [36], two different dynamic regimes emerge: an early- time regime for times $t \sim L$, where the competition between coherent and incoherent drivings develops a dynamic finite-size scaling; and a large- time regime for $t \sim L^3$ whose dynamic scaling describes the late quantum evolution leading to the $t \rightarrow \infty$ stationary states driven by the Liouvillian gap (1.11).

In the following, we extend this analysis of the dissipative defects effects to a localized particle loss, in one- dimensional non-interacting lattice fermionic gases confined within a region of size ℓ . We consider homogeneous systems within hard walls and inhomogeneous systems where the particles are trapped by space-dependent external potentials, such as harmonic traps.

Then, finishing to study the peculiar properties of local and homogeneous dissipation, we focus on the importance of the Liouvillian gap to clarify the interplay between these two different type of dissipation. The aim is to understand if there is a general theory that describe all the discovered properties.

In conclusion, we start to extend all these concepts in case of thermal bath dissipative systems. Here, we consider only the case of quench protocols, but it can be a first step for future research works.

3.2 Out-of-equilibrium dynamics arising from a dissipation hole

As paradigmatic models we consider one-dimensional lattice models of non-interacting spinless fermionic gases, within hard-wall and harmonic traps, subject to dissipative perturbations that give rise to a particle loss localized at one of the sites of the lattice, such as the set up sketched in Fig. 3.1. We model the dissipative particle-decay mechanism by Lindblad master equations governing the time evolution of the density matrix [109, 110, 26, 111, 112]. To investigate the effects of the localized particle-loss dissipation, we study the quantum dynamics arising from protocols starting from the ground state of the fermionic gas, then evolving under the effect of the particle-loss dissipation, for example localized at the center of the system. This is analyzed in the large- ℓ limit for two different initial conditions: fixed number N_0 of initial particles and fixed ratio N_0/ℓ , which corresponds to the *thermodynamic* limit of the initial fermionic gases at equilibrium, in both hard

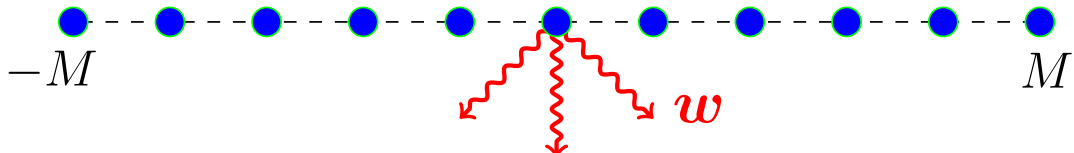


Figure 3.1: Sketch of a fermionic chain of size $L = 2M + 1$ subject to a localized particle loss at the central site, with strength controlled by the dissipation parameter w .

walls and harmonic traps. The quantum evolution of the particle number and space-dependent density turns out to develop various dynamic scaling regimes, and nontrivial large-time behaviors when the dissipative mechanism acts at the center of the system.

Some issues concerning the behavior of fermionic gases in the presence of localized dissipative interactions have been already discussed in Refs. [113, 114, 115, 116, 117], mainly for homogeneous systems neglecting boundary effects. Here we extend these studies by analyzing the interplay between time, size of the system, and number N_0 of initial particles. We analyze the various large-time and intermediate dynamic regimes, in both homogeneous particle systems within hard walls and inhomogeneous particle systems in harmonic traps. Substantially different and peculiar behaviors are observed in fermionic gases confined by hard walls and harmonic traps.

The understanding of the interplay between the time dependence and the finite size of the system is essential to interpret results in various experimental contexts. For example this issue is fundamental for small-size quantum simulators operating on a limited amount of quantum objects, in the presence of controlled dissipation. We also mention experiments with cold atoms within a trap of finite size, when the many-body correlations become eventually sensitive to the trapping potential (local density approximations generally fail to describe quantum correlations, in particular when they are critical [118] and/or out-of-equilibrium [53]).

3.2.1 Free lattice fermions with localized dissipative defects

The Hamiltonian

We consider one-dimensional N -particle Fermi gases defined on a chain with $L = 2M + 1$ sites, by the Hamiltonian

$$\hat{H} = -\kappa \sum_{x=-M}^{M-1} (\hat{c}_x^\dagger \hat{c}_{x+1} + \hat{c}_{x+1}^\dagger \hat{c}_x), \quad (3.1)$$

where \hat{c}_x is a fermion one-particle operator, and $\hat{n}_x = \hat{c}_x^\dagger c_x$ is the particle density operator. We consider hard-wall (open) boundary conditions. The site $x = 0$ is the central site of the chain. In the following we set $\hbar = 1$ and $\kappa = 1$ without loss of generality.

We also consider fermionic systems where the particles are trapped by an external potential, which can be taken into account by adding a corresponding term to the Hamiltonian (3.1), such as

$$\hat{H}_t = - \sum_x (\hat{c}_x^\dagger \hat{c}_{x+1} + \hat{c}_{x+1}^\dagger \hat{c}_x) + \sum_x V(r) \hat{n}_x, \quad (3.2)$$

where

$$\hat{n}_x = \hat{c}_x^\dagger c_x, \quad V(r) = (r/L_t)^p, \quad r \equiv |x|, \quad (3.3)$$

p is a positive number, r is the distance from the center $x = 0$ of the trap, and

L_t plays the role of trap size.¹ The trapping potential is effectively harmonic in most cold-atom experiments [119], i.e., $p = 2$. In the limit $p \rightarrow \infty$ we recover the model (3.1) with hard-wall boundary conditions and $M = \lfloor L_t \rfloor$. The size of systems described by the Hamiltonian \hat{H}_t with finite p is supposed to be infinite. However for practical purposes it is sufficient to consider models within hard walls with $L \gg L_t$. Indeed the large-size convergence is generally fast for sufficiently large values of p , including $p = 2$, due to the fact that the average particle density $\langle \hat{n}_x \rangle$ vanishes rapidly for $|x| \gg L_t$. The main features of the behavior of fermionic gases trapped by a inhomogeneous external power-law potentials have been much investigated, see e.g. Refs. [122, 123, 124, 121, 125].

In systems within both hard-wall and inhomogeneous traps, the particle number operator

$$\hat{N} = \sum_x \hat{n}_x \quad (3.4)$$

commutes with both Hamiltonians (3.1) and (3.2). Therefore the particle number is conserved in both cases. In the following we consider ground states for a number N_0 of particles as starting point of dynamic protocols involving dissipative mechanisms.

Localized particle-decay dissipation

We model the dissipative mechanisms within the Lindblad framework [109, 110], where the evolution of the matrix density $\rho(t)$ of the system is described by the equation [26, 111]

$$\frac{\partial \rho}{\partial t} = \mathcal{L}[\rho] = -i [\hat{H}, \rho] + \mathbb{D}[\rho]. \quad (3.5)$$

We recall that the conditions leading to the Lindblad framework are typically satisfied in quantum optical implementations [28, 112]. The form of the operator $\mathbb{D}[\rho]$ depends on the nature of the dissipation arising from the interaction with the bath. We consider a localized particle-decay dissipation acting at the site z , modeled by the Lindblad operator [126, 127, 29, 107, 116, 117, 112, 53]

$$\mathbb{D}[\rho] = w \left[\hat{c}_z \rho \hat{c}_z^\dagger - \frac{1}{2} (\rho \hat{c}_z^\dagger \hat{c}_z + \hat{c}_z^\dagger \hat{c}_z \rho) \right], \quad (3.6)$$

where w is a parameter controlling the strength of the particle-loss dissipation. Note that reflection symmetry with respect to the center of the confined particle system is only preserved when the particle-loss dissipation is localized at the center. As we shall see, this will lead to peculiar behaviors with respect to the case of particle-loss dissipation localized at generic sites.

The approach to the asymptotic stationary states are generally controlled by the Liouvillian gap $\Delta_{\mathcal{L}}$ associated with the generator \mathcal{L} entering the Lindblad equation (C.6) [26, 111, 32, 128, 35]. The asymptotic stationary state is provided by the eigenstate of \mathcal{L} with vanishing eigenvalue, $\Lambda_0 = 0$, while all other eigenstates have eigenvalues Λ_i with negative real part, i.e. $\text{Re } \Lambda_i < 0$ for any $i > 0$.

¹ L_t plays the role of trap size [119, 120, 121], so that the *thermodynamic* limit is obtained in the large trap-size limit, $L_t \rightarrow \infty$, keeping the ratio between the particle number N and the trap size L_t constant, which can be equivalently obtained by adding a chemical-potential term in the Hamiltonian, such as the one reported in Eq. (3.16).

Dynamic protocol

To study fermionic gases under the effects of a localized particle-loss mechanism, we consider the following dynamic protocol, for systems within both hard-wall and harmonic traps, respectively of size $L = 2M + 1$ and L_t .

- The protocol starts at time $t = 0$ from the ground state of the Hamiltonian (3.1) or (3.2) with a number N_0 of particles. We recall that the ground state of N_0 noninteracting fermionic particles is obtained by filling the lowest N_0 one-particle energy levels.
- The time evolution for $t > 0$ is driven by the Lindblad equation (C.6) for the density matrix $\rho(t)$, with particle-decay dissipation localized at a site z and controlled by the parameter w .
- The particle density and total particle number,

$$n_x(t) = \text{Tr}[\rho(t)\hat{n}_x], \quad N(t) = \text{Tr}[\rho(t)\hat{N}], \quad (3.7)$$

are monitored during the out-of-equilibrium evolution for $t > 0$, up to their large-time behaviors.

To compute the particle density $n_x(t)$ and particle number $N(t)$, we proceed as follows. We introduce the correlation functions

$$\mathcal{C}_{x,y}(t) = \text{Tr}[\rho(t)\hat{c}_x^\dagger\hat{c}_y]. \quad (3.8)$$

For homogeneous systems described by the Hamiltonian (3.1), the Lindblad equation (C.6) implies

$$\begin{aligned} \frac{d\mathcal{C}_{x,y}}{dt} &= i(\mathcal{C}_{x,y+1} - \mathcal{C}_{x-1,y} + \mathcal{C}_{x,y-1} - \mathcal{C}_{x+1,y}) \\ &\quad - \frac{w}{2}(\delta_{z,y} + \delta_{x,z})\mathcal{C}_{x,y}, \end{aligned} \quad (3.9)$$

where $\delta_{x,x} = 1$ and $\delta_{x,y} = 0$ for $x \neq y$. Since we consider open (hard-wall) boundary conditions, $\mathcal{C}_{xy}(t) = 0$ when the coordinates x or y refer to sites outside the space interval $[-M, M]$. An analogous equation can be derived in the presence of an inhomogeneous external trapping potential, cf. Eq. (3.2). We obtain

$$\begin{aligned} \frac{d\mathcal{C}_{x,y}}{dt} &= i(\mathcal{C}_{x,y+1} - \mathcal{C}_{x-1,y} + \mathcal{C}_{x,y-1} - \mathcal{C}_{x+1,y}) \\ &\quad + i\frac{|x|^p - |y|^p}{L_t^p}\mathcal{C}_{x,y} - \frac{w}{2}(\delta_{z,y} + \delta_{x,z})\mathcal{C}_{x,y}. \end{aligned} \quad (3.10)$$

Then, after numerically solving the above equations, we use the relations

$$n_x(t) = \mathcal{C}_{x,x}(t), \quad N(t) = \sum_x n_x. \quad (3.11)$$

One can easily check that for both hard-wall and harmonic traps the derivative of the particle number is proportional to the average particle density n_z at the site z where the particle-decay dissipation is localized, i.e.

$$\frac{dN(t)}{dt} = -w n_z(t) < 0. \quad (3.12)$$

Therefore the particle number decays monotonically, since $n_z(t) \geq 0$, and the particle loss stops if $n_z(t) = 0$ asymptotically.

One may also consider the energy of the system, defined as

$$E(t) = \text{Tr}[\rho(t)\hat{H}], \quad (3.13)$$

for which the Lindblad equation implies

$$\frac{dE(t)}{dt} = \text{Tr}\left[\frac{d\rho(t)}{dt}\hat{H}\right] = w\text{Tr}[\mathbb{D}[\rho]\hat{H}]. \quad (3.14)$$

For systems with particle-loss dissipation localized at the central site $x = 0$, we obtain

$$\frac{dE(t)}{dt} = w \text{Re}(\mathcal{C}_{0,1} + \mathcal{C}_{-1,0}) = 2w \text{Re} \mathcal{C}_{0,1}, \quad (3.15)$$

which holds for systems within hard walls and also inhomogeneous traps.

3.2.2 Fermi gases within hard walls

In this section we consider homogeneous Fermi chains, cf. Eq. (3.1), and discuss the dynamic evolution under the particle-loss dissipation described by the Lindblad equation (C.6), in particular Eq. (B.9). For this purpose, we numerically solve the differential equation (B.9) using the fourth-order Runge-Kutta method (with an accuracy of approximately 10^{-8} on the evolution of the particle number).

We study the interplay between the time dependence, the number N_0 of initial particles and the size $L = 2M + 1$ of the lattice. For this purpose we consider two different situations: (i) the number N_0 of particles is kept fixed while increasing M ; (ii) the number of particles increases as $N_0 \sim M$, so that the ratio N_0/M fixed, while increasing M . Note that the latter condition can be equivalently realized in the large-size limit by adding a chemical potential to the Hamiltonian (3.1), i.e.

$$\hat{H}_\mu = -(\mu + 2) \sum_x \hat{n}_x. \quad (3.16)$$

The value $\mu = \mu_{\text{vs}} = -2$ corresponds to the vacuum-superfluid transition point [42, 122], separating the phase where the lowest Hamiltonian eigenstate has $N = 0$ particles from the one for $\mu > -2$ where the ground-state has $N \sim L$ fermions.

In the following we first analyze the asymptotic large-time regime. Then we show that the time dependence of the particle number develops various asymptotic and intermediate regimes, which may differ in the cases we keep N_0 or N_0/M fixed.

3.2.3 Asymptotic stationary states

For generic locations of the particle-loss defects, the asymptotic stationary state turns out to be trivial, i.e. an empty state without particles. However in some cases, in particular when the defect is localized at the center of the chain, the quantum evolution of the system keeps a residual number of particles even in the large-time limit.

This can be shown analytically, straightforwardly extending the analysis for non-interacting bosons reported in Ref. [129], to free fermions. Since we are considering systems of size $L = 2M + 1$ with hard-wall boundary conditions, we introduce the fermionic operators

$$\hat{\eta}_k = \sqrt{\frac{2}{L+1}} \sum_{y=1}^L \sin\left(\frac{\pi k y}{L+1}\right) \hat{c}_y, \quad (3.17)$$

where, to simplify the formulas, we have shifted the coordinates so that $y = x + M + 1$ (therefore the site coordinates are $y = 1, \dots, L$, and the center is located at $y = M + 1$). This allows us to write the Hamiltonian (3.1) as

$$\hat{H} = -2 \sum_{k=1}^L \cos\left(\frac{\pi k}{L+1}\right) \hat{n}_k, \quad \hat{n}_k = \hat{\eta}_k^\dagger \hat{\eta}_k. \quad (3.18)$$

The operator \hat{n}_k commutes with the Hamiltonian, i.e. $[\hat{H}, \hat{n}_k] = 0$, and satisfies $\sum_k \hat{n}_k = \hat{N} = \sum_x \hat{n}_x$. Its expectation value

$$n_k(t) = \text{Tr}[\rho(t) \hat{n}_k] \quad (3.19)$$

counts the number of particles associated with the mode k . The initial equilibrium ground state with N_0 fermionic particles is constructed by filling the first N_0 one-particle energy levels, thus at $t = 0$ we have $n_k = 1$ for $k \leq N_0 \leq L$, and zero otherwise. The modes with odd (even) k are even (odd) under inversion with respect to the center $y = M + 1$ of the chain. The time evolution of n_k is determined by the Lindblad equation for the density matrix. Considering a particle-decay dissipation located at a generic site z , straightforward calculations lead to the equation

$$\begin{aligned} \frac{dn_k}{dt} &= -\frac{w}{L+1} \sin\left(\frac{\pi k z}{L+1}\right) \\ &\times \sum_{q=1}^L \sin\left(\frac{\pi q z}{L+1}\right) \text{Tr}[\rho(t) (\hat{\eta}_q^\dagger \hat{\eta}_k + \hat{\eta}_k^\dagger \hat{\eta}_q)], \end{aligned} \quad (3.20)$$

where, due to the fact that $[\hat{H}, \hat{n}_k] = 0$, the only contribution to the time derivative of n_k comes from the dissipative term. We note that the r.h.s. of Eq. (3.20) vanishes when

$$kz = j(L+1), \quad j = 1, 2, \dots, \quad (3.21)$$

thus implying the conservation of the corresponding particle number n_k even in the presence of localized particle-decay dissipation.

If we consider a central-site dissipation, thus $z = M + 1 = (L+1)/2$ [we recall that we are using shifted coordinates with respect to Eq. (3.1)], then the condition (3.21) reduces to $k = 2j$, thus implying that n_k remains unchanged for all even k (whose odd-parity modes vanish at the central dissipative site), while it gets suppressed for odd k . Therefore, Eq. (3.20) implies that half of the fermions survives centrally localized decay dissipation. More precisely the stationary states are characterized by a residual particle number $N_{\text{asy}} = N_0/2$ for even N_0 , and $N_{\text{asy}} = (N_0 - 1)/2$ for odd N_0 .

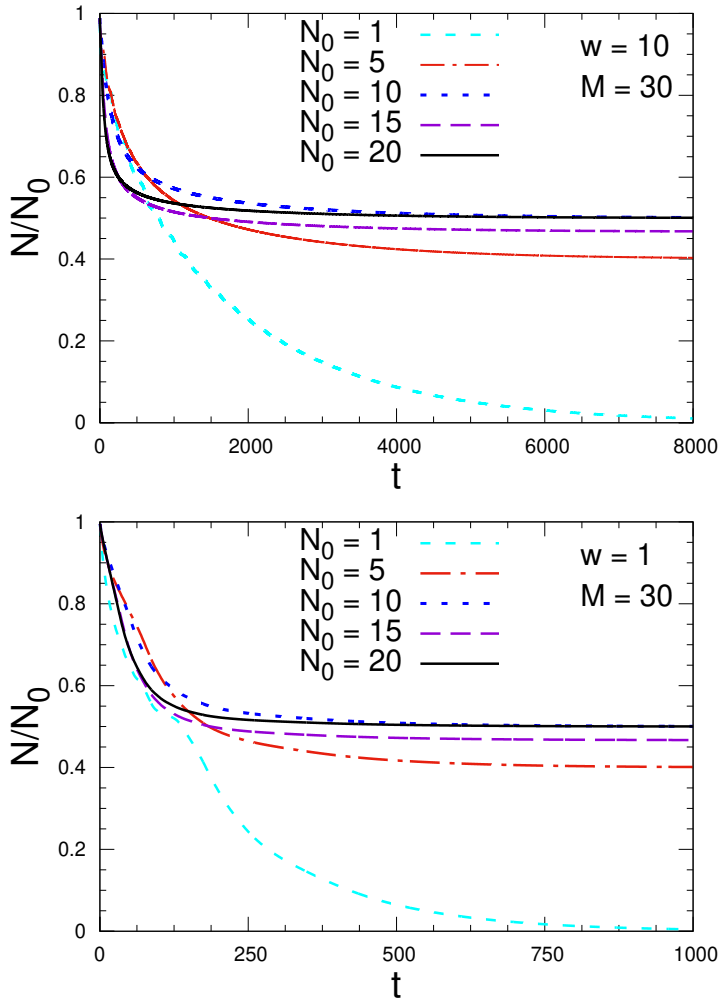


Figure 3.2: Behavior of the ratio $N(t)/N_0$ for the central-site particle-loss dissipation in systems of size $L = 61$ ($M = 30$) within hard walls, various initial particle number N_0 , and dissipation localized at the center of the system, with $w = 1$ (bottom) and $w = 10$ (top). In both cases asymptotic stationary limit turns out to converge to $N/N_0 = 1/2$ for even N_0 , and $N/N_0 = (N_0 - 1)/(2N_0)$ for odd N_0 . Note that approach to the asymptotic value is slower for $w = 10$ than $w = 1$.

Note that the particle loss localized at the center, preserving the parity symmetry with respect to the center of the chain, is the optimal one to keep a fraction of fermionic particles at large time. For example, in the case of a dissipation at the boundaries, i.e., when $z = 1$ or $z = M$ in Eq. (3.20), no particles survive because all k -modes are involved by the Lindblad operator, leading to the complete suppression of the particles filling the initial ground state.

The above analytical results are confirmed by the numerical results for the central particle-loss dissipation, see for example Fig. 3.2 where we show the time dependence of the ratio $N(t)/N_0$ for various values of N_0 and w , and in particular the approach to its nonzero asymptotic limit. Also the space dependence of the particle density n_x turns out to become stable asymptotically, approaching a stationary configuration, as shown in Fig. 3.3. In Fig. 3.4 we show some results for the spatial dependence of the average particle density n_x of the asymptotic stationary states. We note that n_x is quite flat except at $x = 0$ where the dis-

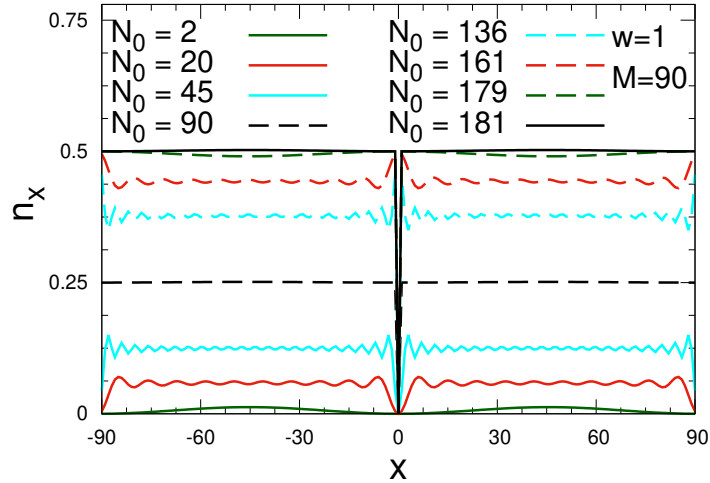


Figure 3.3: Data for the quantum evolution of the fermionic gas within hard walls, size $L = 2M + 1$ with $M = 90$, initial particle number $N_0 = 10$, dissipation localized at the center of the chain with $w = 1$. We show the particle density $n_x(t)$ at the sites $x = 0$ and $x = 10$ (top), and the ratio $N(t)/N_0$ (bottom). They approach asymptotic stationary limits (at least within the numerical precision, which is very accurate).

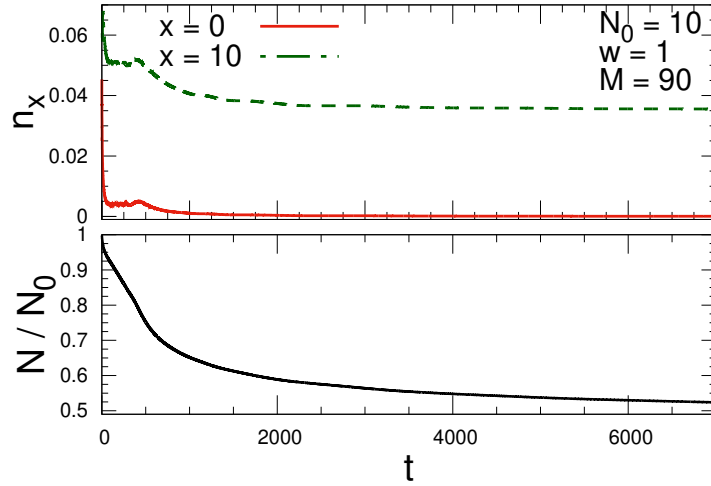


Figure 3.4: Asymptotic stationary limit of the particle density n_x for systems of size $L = 181$ ($M = 90$) within hard-wall boundary conditions, in the presence of a central-site dissipation with $w = 1$, and for various N_0 . In all cases the particle density vanishes for $x = 0$, and it is almost flat elsewhere, apart from small spatial oscillations, which appear similar to the Friedel oscillations characterizing the behavior of closed particle systems

sipative mechanism acts, and at the boundaries of the chain (essentially due to the hard-wall boundary conditions). The almost flat region shows some spatial oscillations, which appear suppressed when $N_0 \approx M$ and $N_0 \approx 2M$.

3.2.4 Approach to the asymptotic states

Large-size behavior of the Liouvillian gap

The approach to the stationary state is controlled by the Liouvillian gap $\Delta_{\mathcal{L}}$ of the generator \mathcal{L} of the Lindblad equation [26, 111, 32, 128, 35],

$$\Delta_{\mathcal{L}} = -\text{Max}_{i>0} \text{Re}(\Lambda_i), \quad (3.22)$$

where Λ_i are the eigenvalues of \mathcal{L} (we recall that the largest eigenvalue is $\Lambda_0 = 0$ and $\text{Re} \Lambda_i < 0$ for any $i > 0$). The Liouvillian gap for homogeneous spin chains and fermionic wires with localized dissipative mechanisms, such as that described by Eq. (3.6), shows generally the asymptotic finite-size behavior [130, 131, 32, 35, 36]

$$\Delta_{\mathcal{L}}(w, L) \approx D_{\mathcal{L}}(w) L^{-3}. \quad (3.23)$$

We expect that this asymptotic large- L behavior holds independently of the location of the particle-decay dissipation, and it does not depend on the initial conditions, thus on N_0 . The scaling equation (3.23) implies that the approach to the asymptotic behavior becomes slower and slower with increasing the size L of the lattice at fixed w .

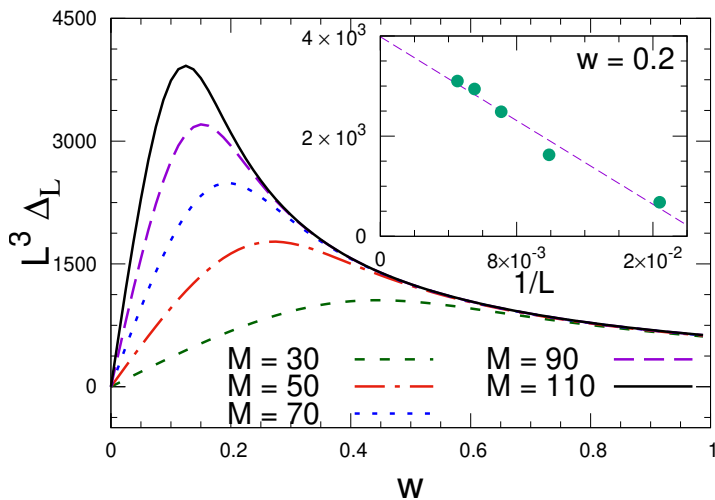


Figure 3.5: The Liouvillian gap $\Delta_{\mathcal{L}}$ for particle-decay dissipation localized at the center of the chain, for various system size $L = 2M + 1$. The curves appear to converge with increasing M ; this is clearly shown at least for $w \gtrsim 0.2$, as also shown by the large- L convergence at a fixed value $w = 0.2$ [suggesting that the corrections to the asymptotic scaling behavior (3.23) are approximately $O(L^{-1})$]. Like the case of dissipation at the boundaries, we believe that the convergence extends to any $w > 0$, but, unlike dissipation at the boundaries, it is nonuniform when decreasing w toward zero, see text.

The asymptotic behavior (3.23) is confirmed by numerical analyses of the Liouvillian gap using the method outlined in Ref. [130], see App. B. Some numerical results are shown by Figs. 3.5 and 3.6, for particle-decay dissipation localized at the center and at the boundary of the chain, respectively.

In both cases, $\Delta_{\mathcal{L}}$ appears nonmonotonic, increasing for small values of w and decreasing for sufficiently large dissipation strength w , for any L . The approach

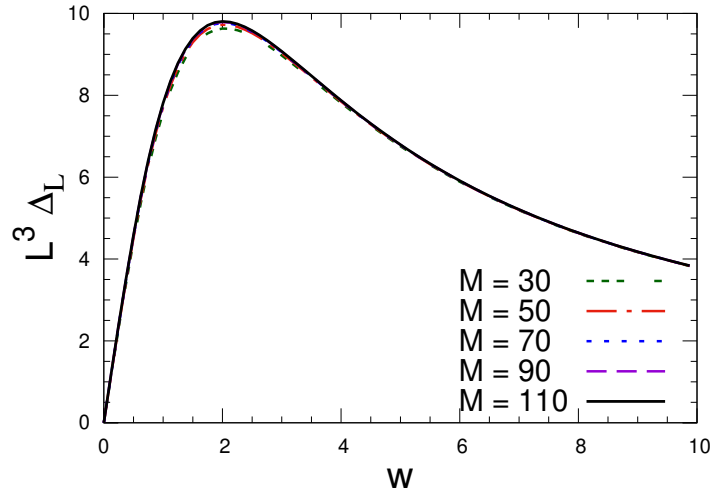


Figure 3.6: Scaling behavior of the Liouvillian gap $\Delta_{\mathcal{L}}$ for particle-decay dissipation localized at one of the boundaries of the chain.

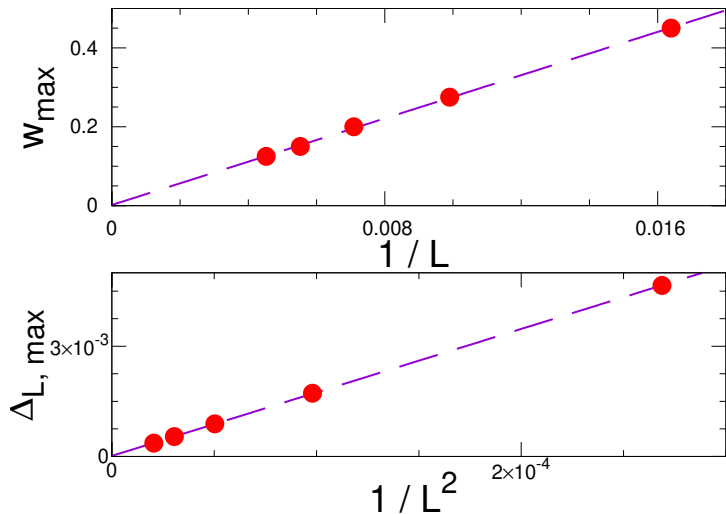


Figure 3.7: Some details of the behavior of the Liouvillian gap $\Delta_{\mathcal{L}}$ for dissipation localized at the center of the lattice. We show the location w_{\max} of the maximum of the Liouvillian gap (top), showing that $w_{\max} \sim L^{-1}$, and value of $\Delta_{\mathcal{L}}$ at the maximum (bottom), showing that $\Delta_{\mathcal{L}}(w_{\max}) \sim L^{-2}$.

to the asymptotic behavior becomes slower and slower with increasing w for large w . In particular, $\Delta_{\mathcal{L}}(w, L)$ shows the large- w behavior $L^3 \Delta_{\mathcal{L}}(w) \approx D_{\mathcal{L}}(w) \sim w^{-1}$. This explains the results shown in Fig. 3.2, where the approach to the asymptotic value of the particle number for $w = 10$ turns out to be slower than that for $w = 1$. The suppression in the limit of strong dissipation, for large w , may be interpreted as a quantum-Zeno-like phenomenon [132, 133], where a strong dissipation somehow slows down the dynamics, see e.g. Refs. [134, 135] for the appearance of similar quantum Zeno regimes.

As shown by Figs. 3.5 and 3.6, the Liouvillian gap at fixed L has a maximum at an intermediate value of w . The corresponding values w_{\max} and $L^3 \Delta_{\mathcal{L}}(w_{\max})$ appears to rapidly converge to the large- L limit in the case of dissipations localized at the boundaries, but they show an apparent size dependence in the case

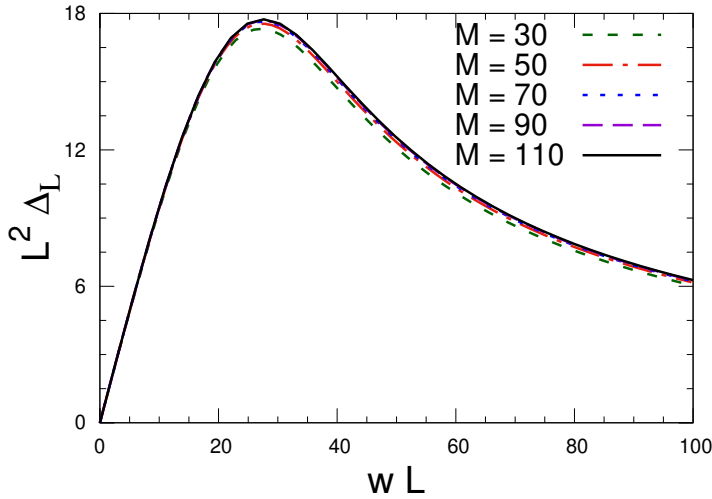


Figure 3.8: Plots of $L^2 \Delta_{\mathcal{L}}$ versus wL for systems within hard walls and with central particle-loss dissipation, for various $L = 2M + 1$. They support the scaling equation (3.24).

of dissipation localized at the center. Indeed the approach to the asymptotic L^{-3} behavior (3.23) appears significantly slower in the case of dissipation localized at the center, in particular for small w , which suggests a nonuniform convergence for $w \rightarrow 0$. The curves for different lattice sizes appear to clearly converge for $w \gtrsim 0.2$, as also shown by the inset of Fig. 3.5. We conjecture that, like the case of dissipation at the boundaries, the convergence in the large-size limit extends to any $w > 0$, but it is nonuniform when decreasing w toward zero, unlike dissipation at the boundaries. This is demonstrated by the plots reported in Figs. 3.7, which show that the location of the maximum value of the Liouvillian gap for central dissipation moves toward $w = 0$, with $w_{\max} \sim L^{-1}$, and its maximum value decreases as $\Delta_{\mathcal{L}}(w_{\max}) \sim w_{\max}^2 \sim L^{-2}$, instead of the general asymptotic L^{-3} behavior for $w > 0$ fixed. Actually, they suggest that the Liouvillian gap for central dissipation shows also the asymptotic scaling behavior

$$\Delta_{\mathcal{L}}(w, L) \approx D_{\mathcal{L}}(wL) L^{-2}, \quad (3.24)$$

obtained in the large- L limit keeping wL constant. This scaling behavior is demonstrated by the plot reported in Fig. 3.8. Therefore the function $D_{\mathcal{L}}(w)$ entering the asymptotic L^{-3} behavior (3.23) must be singular for $w \rightarrow 0$ in the case of central-site dissipation, diverging as w^{-1} .

Note that the above considerations on the behavior of the Liouvillian gap apply to generic values of w , and, of course, they do not depend on the initial number N_0 of particles. In the following we will mainly present results for the value $w = 1$ of the dissipation parameter, whose dynamic scenarios are shared with those arising from generic finite values of w .

Large-time behavior of the particle number

On the basis of the large-size behavior of the Liouvillian gap, we expect that the time scale t_a of the approach to the stationary state is given as

$$t_a \sim \Delta_{\mathcal{L}}^{-1} \sim L^3, \quad (3.25)$$

at fixed $w > 0$. This time scale must characterize the approach to the stationary limits of the particle number and density. This is confirmed by the numerical computations, see for example Fig. 3.9 where we report results for the ratio

$$R_N(t) \equiv \frac{N(t) - N_{\text{asy}}}{N_0 - N_{\text{asy}}} , \quad (3.26)$$

for protocols starting from a fixed number N_0 of particles. They show the asymptotic large- L scaling behavior

$$R_N(t, w, L) \approx A(t/L^3, w) , \quad (3.27)$$

which also implies

$$\frac{dR_N(t, w, L)}{dt} \approx L^{-3} B(t/L^3, w) .$$

Analogous results are obtained for the case we start from a fixed ratio N_0/M , as shown in Fig. 3.10 for $N_0/M = 1/2$, where we plot $N(t) - N_{\text{asy}}$ versus t/L^3 and the curves appear to collapse in the large- M limit. Note that when N_0/M is kept fixed, the quantity R_N defined in Eq. (3.26) is not appropriate, because it is always suppressed in the large-time limit, due to the denominator that behaves as $N_0 - N_{\text{asy}} \sim L$.

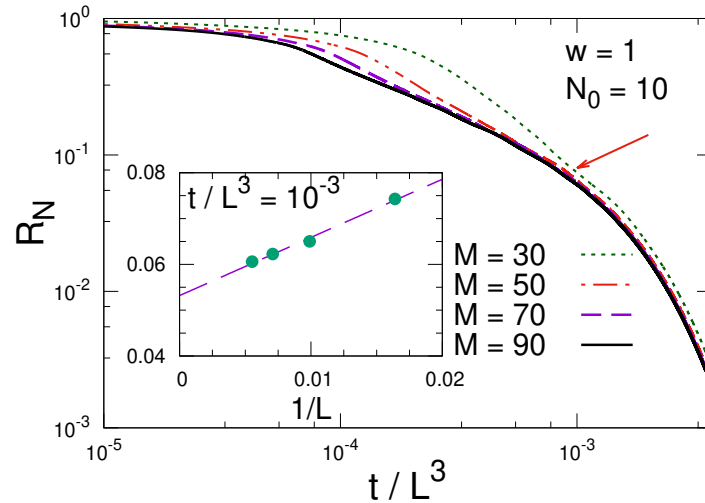


Figure 3.9: The time dependence of the ratio R_N versus t/L^3 ($L = 2M + 1$), for homogenous systems within hard walls with $N_0 = 10$ and central particle-loss dissipation with $w = 1$. The data for various sizes M show clearly the convergence toward a dynamic scaling curve, approximately as $1/L$ as shown by the inset for a particular value of the ratio t/L^3 (the one indicated by the arrow in the main figure).

As we will show below, this is not the end of the story, indeed further peculiar intermediate scaling behaviors emerge, differing between the cases N_0 and N_0/M fixed.

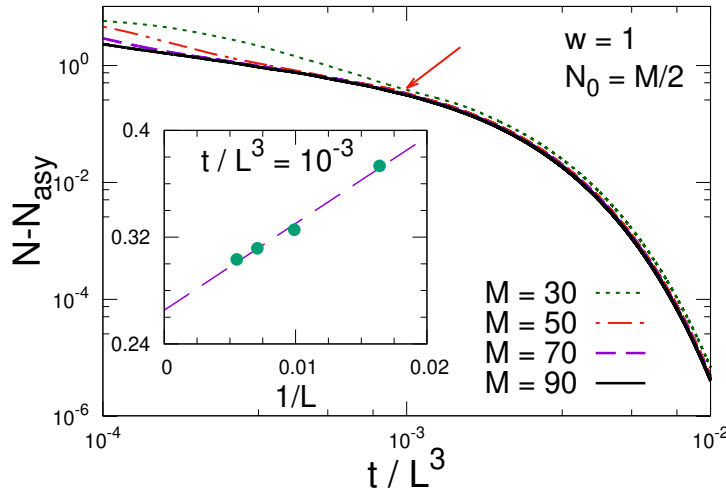


Figure 3.10: The difference $N(t) - N_{\text{asy}}$ vs t/L^3 , for systems within hard walls with $N_0/M = 1/2$, and central dissipation with $w = 1$. Again we observe the asymptotic convergence toward a dynamic scaling curve, as shown by the inset for a particular value of t/L^3 (indicated by the arrow in the main figure).

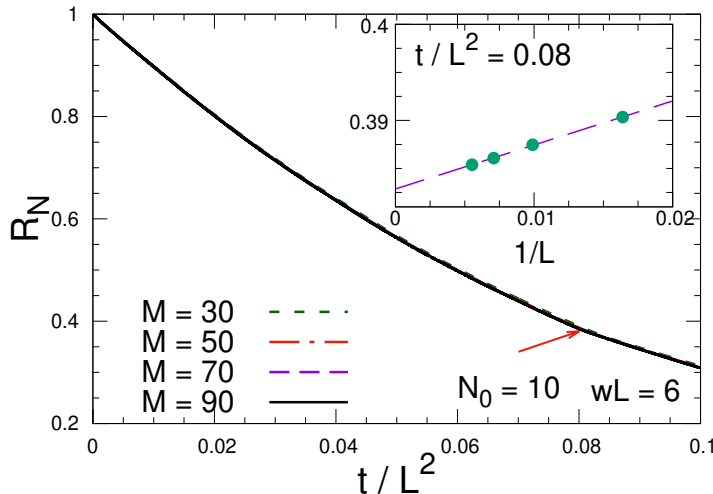


Figure 3.11: The ratio R_N versus t/L^2 for systems within hard walls with $N_0 = 10$, central dissipation with $wL = 6$, for various lattice sizes $L = 2M + 1$. The data appear to converge toward a scaling curve in the large- L limit, as demonstrated by the data reported in the inset for a particular value of the ratio t/L^2 .

3.2.5 Intermediate scaling behaviors keeping N_0 fixed

We now look for intermediate regimes of the time evolution, somehow associated with the time scales of the Hamiltonian (3.1) driving the unitary dynamics, and therefore to its gap Δ_H , i.e. the energy difference between the first excited state and the ground state. When keeping the particle number N_0 fixed, Δ_H behaves asymptotically as $\Delta_H \sim L^{-2}$, corresponding to the dynamic exponent $z = 2$ of the vacuum-superfluid transition [42].

We want to check whether the out-of-equilibrium dynamics develops an intermediate regimes somehow controlled by the Hamiltonian driving of the Lindblad equation, whose intrinsic time scale is related to its gap, i.e. $t \sim \Delta_H^{-1} \sim L^2$, which

is much smaller than the time scale $t \sim L^3$ characterizing the approach to the stationary large-time limit (of course, for sufficiently large L , and in particular in the large- L limit). As we shall see, a closer look at the time evolution provides a clear evidence of such intermediate regime, which also requires a rescaling of the dissipation strength.

In Fig. 3.11 we show some results for the time dependence of the particle number in the case of systems with central-site dissipation starting from a fixed number of particles. We observe that the above-mentioned intermediate regime exists, and extends to any $t \sim L^2$, if we perform an appropriate rescaling of the dissipation parameter w , decreasing w as $w \sim L^{-1}$. Indeed the numerical results clearly support the large- L scaling behavior

$$R_N(t, w, L) \approx U(t/L^2, wL), \quad (3.28)$$

which is obtained by increasing L keeping the ratio t/L^2 and the product wL fixed. Note that this intermediate scaling behavior is expected to hold even for large values of the ratio t/L^2 , because it is also compatible with the alternative scaling behavior (3.24) of the Liouvillian gap.

3.2.6 Intermediate dynamic behavior keeping N_0/M fixed

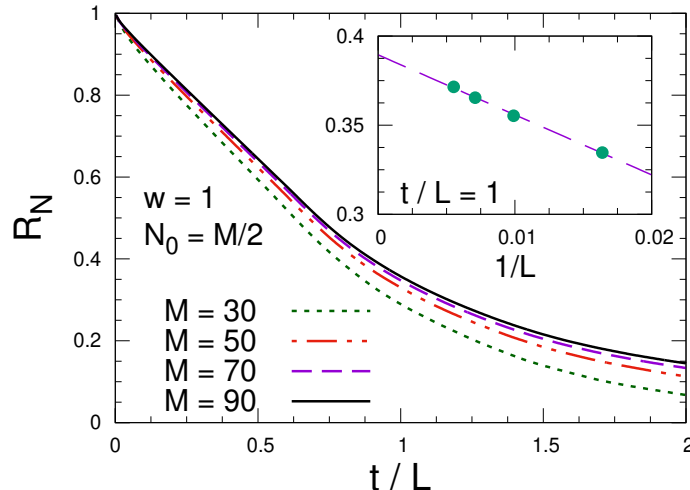


Figure 3.12: Behavior of the ratio R_N versus t/L , for systems within hard walls with $N_0/M = 1/2$, and central dissipation with $w = 1$. The inset shows the $1/L$ approach to the large- L asymptotic behavior.

We now consider the large- L behavior in the case we keep the ratio N_0/M fixed when increasing $L = 2M + 1$. This corresponds to the superfluid phase, i.e. when the chemical potential μ is larger than that at the vacuum-superfluid transition, $\mu > -2$. Within the superfluid phase, the gap Δ_S of isolated free Fermi gases behaves as [42] $\Delta_S \sim L^{-1}$.

Again we want to check whether the out-of-equilibrium dynamics in this condition develops an intermediate regime controlled by the part of the Lindblad equation driving the unitary dynamics introduces a time scale $t \sim \Delta_S^{-1} \sim L$ (again, much smaller than the time scale $t \sim L^3$ characterizing the approach to

the stationary large-time limit). Like the case at fixed N_0 , we show that such an intermediate regime exists.

The existence of a corresponding intermediate regime of the dynamics is demonstrated by the results shown in Fig. 3.12, leading to the intermediate scaling ansatz

$$R_N(t, w, L) \approx W(t/L, w), \quad (3.29)$$

obtained keeping t/L fixed in the large- L limit.

We finally report the existence of a further early-time regime when we start from the ground state for $N_0 \propto M$, as already noted in Ref. [117]. Indeed, for sufficiently small time

$$\frac{dN(t, w, L)}{dt} \approx f(t, w), \quad (3.30)$$

without showing any asymptotic size dependence. This is shown by the curves reported in Fig. 3.13. The behavior (3.30) is observed in the large-size limit, and can be considered as the *thermodynamic* limit of the quantum evolution, when the time is sufficiently small that the dynamics does not yet detect the effects of the boundaries. Indeed deviations are observed for $t \propto M$, thus later and later for larger and larger systems. At the end of this early-time regime, the intermediate regime (3.29) begins.

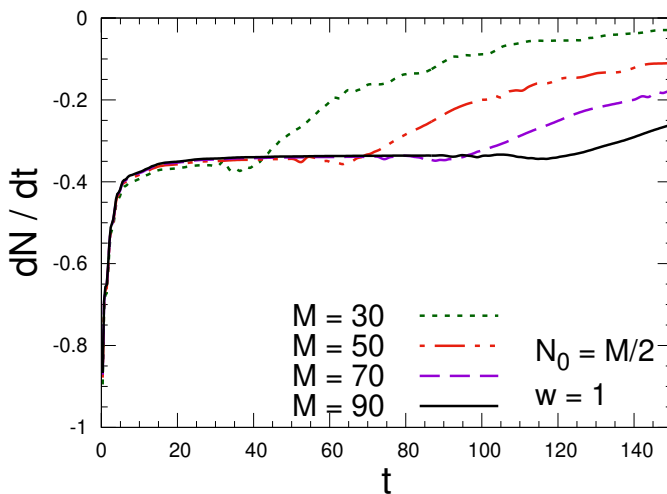


Figure 3.13: The time dependence of the derivative of the particle number, for systems within hard walls with central-site dissipation with $w = 1$, starting from ground states with $N_0/M = 1/2$ fixed.

3.3 Fermionic gases within harmonic traps

We now present results for lattice fermionic systems within traps arising from inhomogeneous external potentials, such as those in Eq. (3.3), in the presence of a particle-decay dissipation at the center of the trap, as described by the Lindblad equations (C.6) and (3.6). As already mentioned in the introductory section, effective harmonic trapping mechanisms are quite common in cold-atom experiments [119]. Therefore their analysis is also relevant from a phenomenological point of view.

We study the time evolution in the limit of large trap size L_t , in the case we keep the initial particle number N_0 fixed, and when we keep the ratio N_0/L_t constant (equivalent to adding a chemical potential). We consider harmonic traps, thus $p = 2$ in Eq. (3.3). The results are obtained for sufficiently large systems L at fixed L_t , so that a further increases of L does not change the results at fixed L_t , and therefore they can be considered as results for infinite-size systems with a large accuracy, within the accuracy of the numerical calculations, better than 10^{-8} .

3.3.1 Large-time behavior

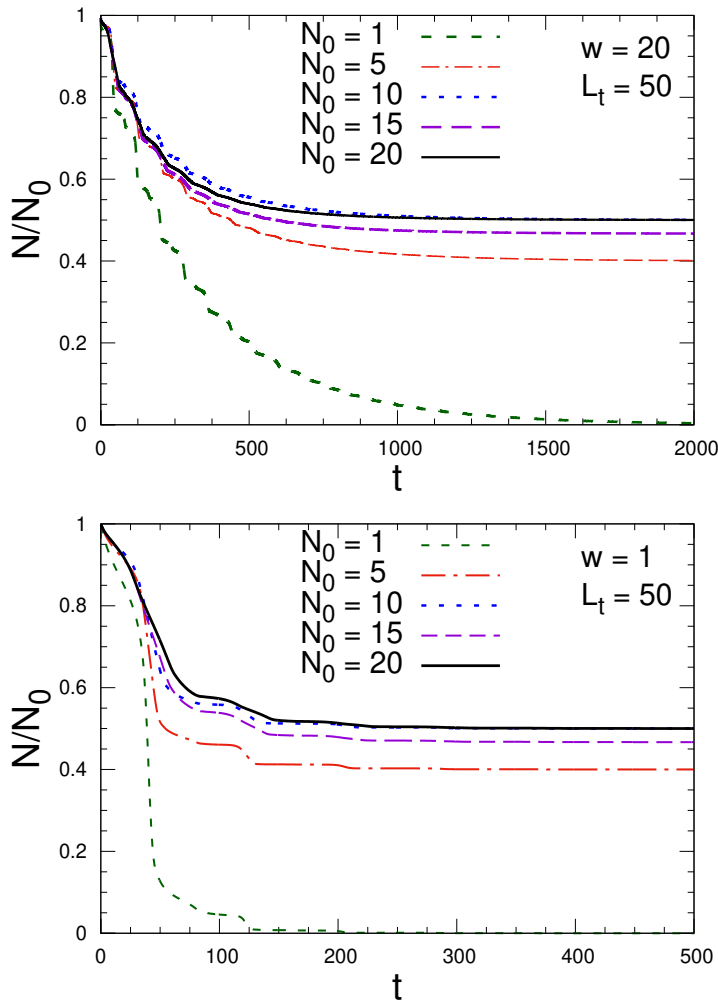


Figure 3.14: The time dependence of the ratio N/N_0 for the central-site particle-loss dissipation $w = 1$ (bottom) and $w = 20$ (top) in systems within harmonic traps, various N_0 , and $L_t = 50$ (in the large- L limit to make the finite-size effects negligible). The asymptotic stationary limit turns out to converge to $N/N_0 = 1/2$ for even N_0 , and $N/N_0 = (N_0 - 1)/(2N_0)$ for odd N_0 . Similarly to the case of systems within hard walls, see Fig. 3.2, the approach to the asymptotic value turns out to be slower for $w = 20$ than $w = 1$.

To begin with, we discuss the asymptotic stationary states. In Fig. 3.14 we show the time dependence, and asymptotic behavior, of the ratio $N(t)/N_0$ for

various values of the initial number of particles. Again, similarly to the case of homogeneous systems within hard walls and particle-decay dissipation at the center of the chain, we find that the large-time states keep a half of the initial particles. Analogously to the hard-wall case, this can be related to the fact that the one-particle Hamiltonian is invariant under reflections with respect to the center, thus the one-particle states must have definite parity. This can be easily seen in the continuum limit, see e.g. Ref. [122], where the one-particle Hamiltonian eigenfunctions can be written in terms of Hermite polynomials, and have definite parity. Since the one-particle states with negative parity vanishes at the center of the trap, the corresponding modes in the ground state of the fermionic system are not affected by the particle-decay dissipation at the center of the trap. Then, recalling that the ground state is obtained by filling the first N_0 one-particle levels, a selection mechanism analogous to that identified in the case of homogeneous systems applies, see Sec. 3.2.3, therefore half of them are odd [more precisely $N_0/2$ for even N_0 and $(N_0 - 1)/2$ for odd N_0], we expect again that half particles survive the central particle loss.

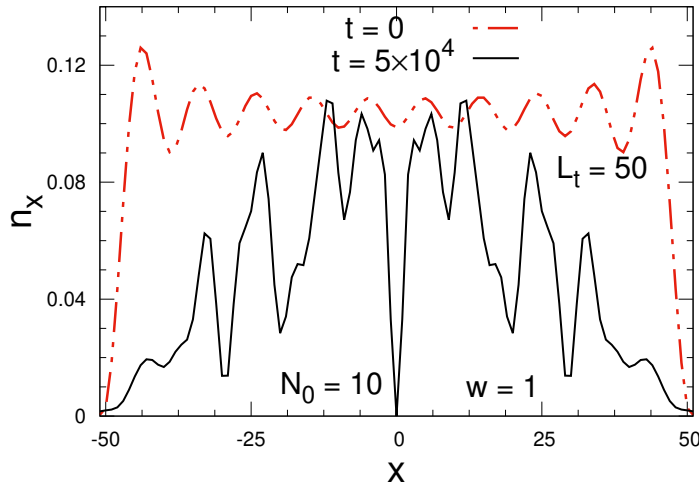


Figure 3.15: The particle density n_x for systems within a harmonic trap with initial particle number $N_0 = 10$, at $t = 0$ and after some time t , for a central dissipation with $w = 1$, fixed trap size $L_t = 50$, and for a sufficiently large size of the system, $L = 221$, to make finite-size effects negligible (numerically checked by verifying the dependence on L).

In Fig. 3.15 we show the particle density at $t = 0$ and at large time when the central particle density has already stably vanished. However, the spatial dependence of the particle density does not appear static in the large-time regime where the particle number stops decreasing. Indeed, as shown in Fig. 3.16, the time dependence of the particle density at sites $x \neq 0$ is characterized by time oscillations that apparently continue indefinitely, persisting even in the large- L_t limit. We also note that in this large-time regime the quantum evolution of the particle density appears effectively driven by the Hamiltonian term only. We have checked that the dissipative contribution in Eq. (3.10), i.e. the one proportional to w , gets suppressed asymptotically, thus only the Hamiltonian determines the large-time dependence of the fixed-time two-point function $\mathcal{C}_{xy}(t)$ and $n_x = \mathcal{C}_{xx}(t)$. In this large-time regime also the energy of the system defined in Eq. (3.13) remains

constant, indeed its time derivative vanishes when $\text{Re } \mathcal{C}_{0,1} = 0$, cf. Eq. (3.15).

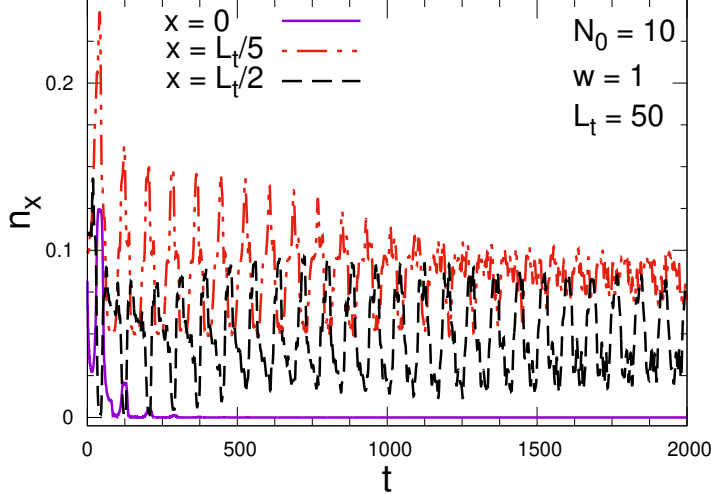


Figure 3.16: Time dependence of the particle density for systems within a trap of size $L_t = 50$, at various spatial coordinates, $x = 0$, $x = L_t/5 = 10$ and $x = L_t/2 = 25$, for central dissipation with $w = 1$. The particle density n_x for $x \neq 0$ are characterized by oscillations in the large-time regime, when n_x at $x = 0$ and the particle number have already approached their asymptotic behavior.

3.3.2 Large- L_t scaling behavior of the time dependence

The time dependence starting from a fixed number of particles shows the peculiar scaling behavior

$$R_N(t, w, L_t) \equiv \frac{N(t) - N_{\text{asy}}}{N_0 - N_{\text{asy}}} \approx A_t(t/L_t, w), \quad (3.31)$$

which apparently describes the whole time evolution. This is clearly supported by the data reported in Figs. 3.17 and 3.18 for central dissipation with $w = 1$ and initial particle number $N_0 = 10$.

Note that the time scale $t \sim L_t$ may be also related to the gap of the fermionic Hamiltonian, for which $\Delta_{L_t} \sim L_t^{-z\theta}$ where $z = 2$ is the dynamic exponent associated with the vacuum-to-superfluid transition, and $\theta = 1/2$ is the universal trap exponent characterizing critical behaviors in the presence of trapping potentials [136, 124, 122, 53] [for generic power laws of the potential (3.3), $\theta = p/(p+2)$].

The time scale $t \sim L_t$ characterizes the whole evolution of the system, up to the large-time regime, except for some small intermediate time intervals. Indeed, the curves shown in the bottom Fig. 3.17 presents some flat regions followed by rapid changes. Actually a more careful analysis, see, e.g., the top Fig. 3.17, shows that the scaling function $A_t(t/L_t, w)$ entering Eq. (3.31) appears to develop a singularity in the large-time limit, at $t/L_t = \tau^* \approx 0.8147$, so that

$$A_t(t/L_t, w) \approx f[L_t(t/L_t - \tau^*)] \quad (3.32)$$

around $t/L_t = \tau^*$. Therefore this sharp drop of the particle density occurs at a time $t^* \approx L_t \tau^*$ in the large- L_t limit, and lasts for a finite time interval, i.e. it

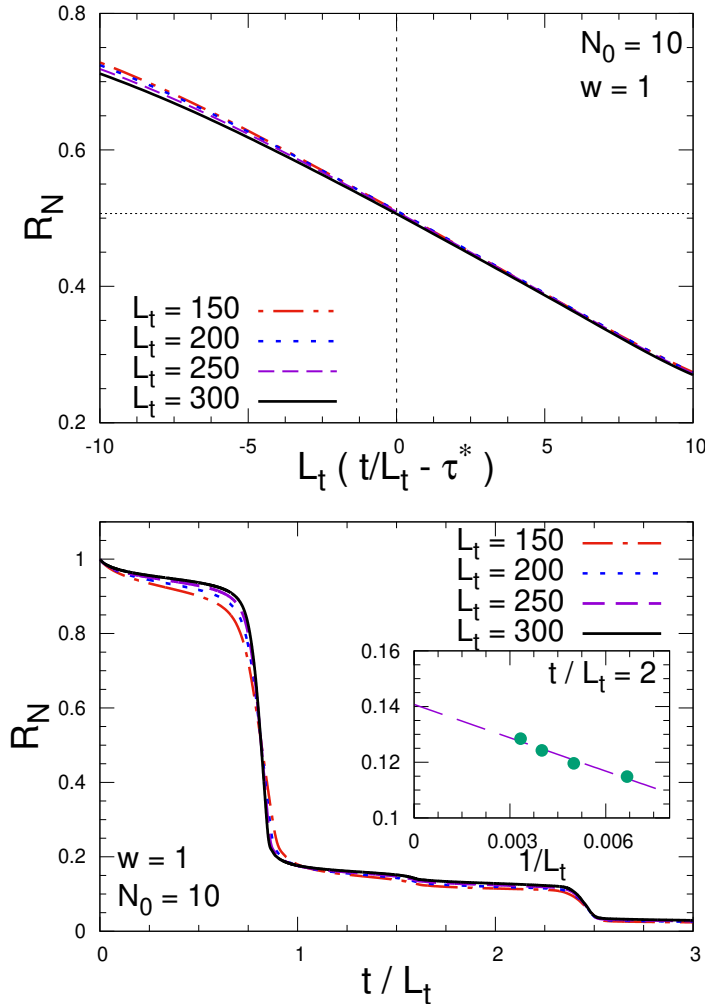


Figure 3.17: The bottom figure shows the time evolution of the ratio R_N versus t/L_t for $w = 1$, various trap sizes, keeping the initial number of particles $N_0 = 10$ fixed. The inset shows an example of convergence at $t/L_t = 2$. The top figure shows the scaling behavior at the fast drop of the particle number, around $t/L_t \approx 0.8147$, described by Eq. (3.32).

does not diverge when increasing L_t . Some data for the behavior of the particle density and number around the time τ^* are shown in Fig. 3.19, where we note the significant increase of the particle density around $x = 0$ when the singular behavior of the scaling function (3.31) appears. Analogous behaviors are observed for generic values of N_0 and w .

In the case we keep N_0/L_t fixed, the results show a generic scaling behavior in terms of t/L_t , analogous to Eq. (3.31), see for example Fig. 3.20.

3.4 From local to uniform dissipation: the sunburst model

We consider a lattice model tailored to unveil the crossover regime between the dissipation schemes presented. We investigate a $(1+1)$ -dimensional Kitaev ring with local particle-decay dissipators arranged in a *sunburst* geometry [38, 39, 40].

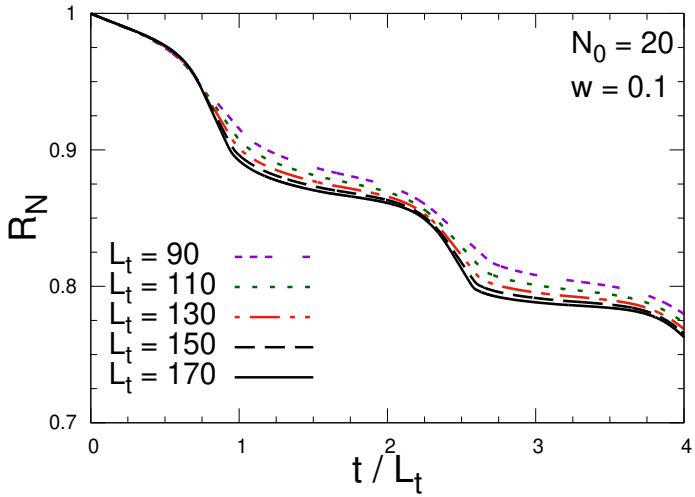


Figure 3.18: The ratio R_N for $w = 0.1$, various trap sizes, keeping the initial number of particles $N_0 = 20$ fixed.

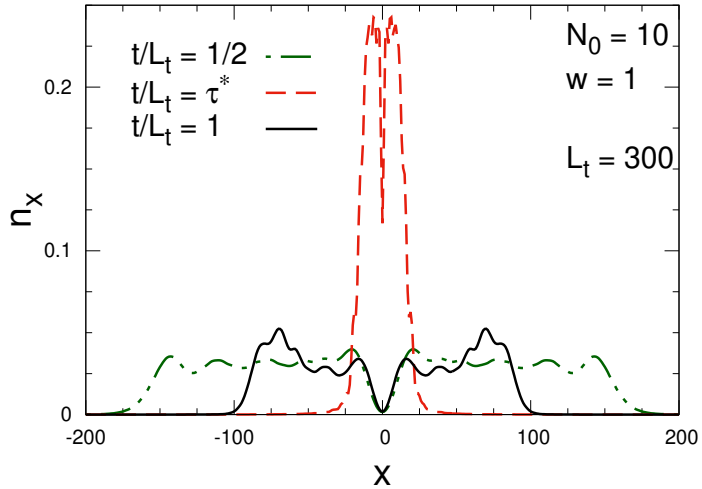


Figure 3.19: Behavior of the particle density around the singularity of the scaling function (3.31), for $L_t = 300$, central particle loss with $w = 1$, and some values of the ratio t/L_t around the singular point $t/L_t = \tau^* \approx 0.8147$. They show that large drop of the particle number at τ^* is connected with a simultaneous large increase of the particle density at the center of the trap.

The whole apparatus is sketched in Fig. 3.21. The open quantum system is coupled with the environment by means of $n \equiv L/b$ equally-spaced external baths, which reduce to some extent the translation invariance of the starting model. In particular, we focus on the case of particle-decay jump operators in the Eq.(1.4), i.e., $\hat{L}_x = \hat{c}_x$, where fermionic particles are continuously removed from the site x . With this choice, the Liouville operator \mathcal{L} is quadratic in the fermionic variables \hat{c}_x and \hat{c}_x^\dagger , and, in this sense, we say that the open ring we study maintains its integrability. Most of the results discussed in this work should preserve their validity also for particle-pumping dissipation ($\hat{L}_x = c_x^\dagger$), since Eq. (1.4) is still quadratic in the fermionic creation and annihilation operators.

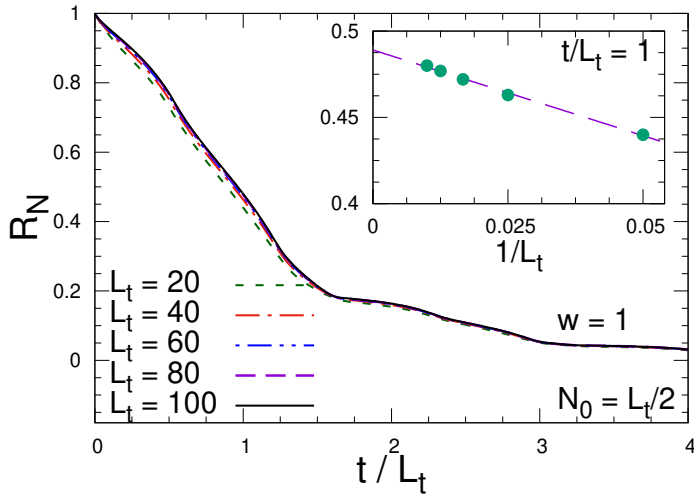


Figure 3.20: Time evolution of the ratio R_N versus t/L_t for fermionic gases within harmonic traps of various size, keeping the ratio $N_0/L_t = 1/2$ fixed, for central particle-loss dissipation with $w = 1$. The large- L_t convergence is evident, as also shown by the plot reported within the inset.

We explore different large-size limits, depending on the number of dissipators taken into account. A thorough study of the Liouvillian gap Δ_λ is the main focus of the first part of this section. In the second part, we examine the real-time evolution of the system, triggered by a *soft quench* of a coupling constant appearing in the defining hamiltonian ¹. Starting the protocol in the proximity of a CQT, we study the out-of-equilibrium dynamic using RG arguments and FSS frameworks [41, 27].

We emphasize the interplay between the unitary and dissipative dynamics and the role played by the gap Δ_λ , extending some of the results already presented in Ref. [107] to our model. To outline our FSS theory, we mainly focus on the scaling properties of the critical correlations and one of the most common entanglement quantifiers, i.e., the entanglement entropy [137].

3.4.1 Liouvillian Gap

This section is devoted to discussing the different scaling behaviors observed for the Liouvillian gap Δ_λ defined in the subsection 1.4.2. We will consider two different limits, depending on the number of dissipation sources considered with increasing the lattice size.

Liouvillian gap at fixed b

The value of the Liouvillian gap at fixed b can be computed using two different algorithm. One, useful for small value of b , consists to analyze the system in the Fourier space the Lindblad vectorized Eq. (1.9) whose spectrum gives the gap.

¹In a *soft quench* the variation of the quenched parameter is attenuated down to 0 with increasing the lattice size L .

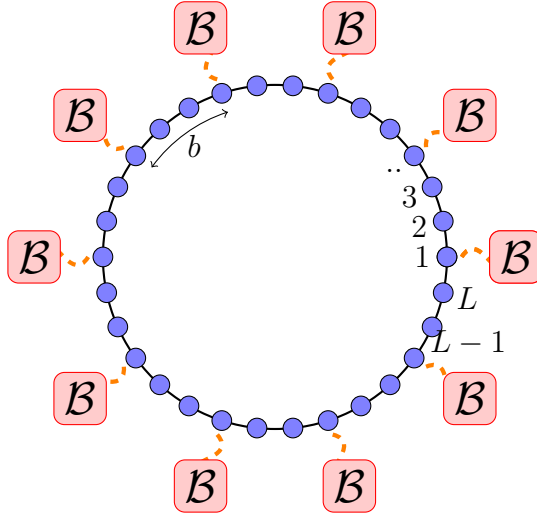


Figure 3.21: Sketch of a Kitaev ring with $L = 30$ qubits coupled with $n = 10$ dissipators in a *sunburst* geometry ($b = 3$ in the figure).

The latter uses the third quantization technique, see details in Ref. [131], particularly convenient for high value of the parameter b [138]. Without loss of generality, we will focus only on small values of b , i.e. up to $b = 7$, but all the results can be extended also in the case of high $b > 7$.

For $b = 3$, the Liouville gap Δ_λ shows a behavior in terms of w in Fig. 3.22. At fixed L , we can easily distinguish two different regimes for the gap, which are separated by a bump in the gap located at $w_*(L)$. We clarify that a non-monotone trend in Δ_λ is not unexpected due to the presence of the *quantum Zeno effect* – the dynamic of a quantum system slows down when it is frequently monitored [132, 139]. Note also that both $w_*(L)$ and $\Delta_\lambda(w_*)$ vanish in the thermodynamic limit, so only the region with $w \geq w_*$ is relevant to determine the typical relaxation time of the system for large enough ring sizes. As shown in Fig. 3.22, for $w < w_*$, the gap is perfectly compatible with a linear dependence of the form

$$\Delta_\lambda(w, b) = \frac{w}{2b}, \quad w < w_*. \quad (3.33)$$

We have verified numerically that the above expression holds also for different values of $b \leq 7$ (not shown). This equation has a clear interpretation when we rewrite $\mathbb{D}[\rho]$ in momentum space. Indeed, the full Hilbert space decomposes into the direct product of $n/2$ distinguished sectors with a dimension 4^b . The effective coupling perceived within each sector is equal to w/b . If we additionally assume that the minimum contribution stemming from a single sector is $1/2$ (which is always the case for $b = 1$), we get Eq. (3.33).

On the other hand, when $w > w_*$, we observe that the gap Δ_λ still depends linearly on the coupling w , but the slope of the asymptotic straight line approached is no longer $1/2b$. We conjecture that for $w > w_*$ and sufficiently large b , the following expression describes the Liouvillian gap

$$\Delta_\lambda(w, b) = A_\mu(b)w, \quad A_\mu(b) = \frac{C_\mu}{b^3}, \quad w > w_*, \quad (3.34)$$

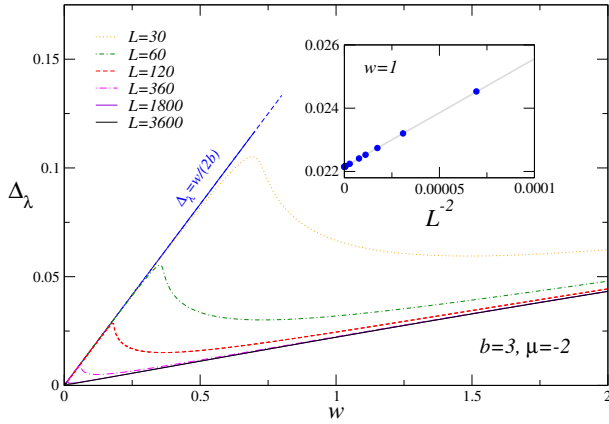


Figure 3.22: Liouvillian gap Δ_λ in terms of the dissipation coupling w for $b = 3$ and fixed $\mu = -2$. For small w and L finite, the gap depends linearly on the dissipation strength as $\Delta_\lambda = w/2b$. With increasing L and finite $w > 0$, the Liouvillian gap approaches a different regime, which still depends linearly on w . In the inset, scaling corrections evaluated at $w = 1$ are perfectly consistent with a L^{-2} decaying. The gray straight line is drawn to guide the eye.

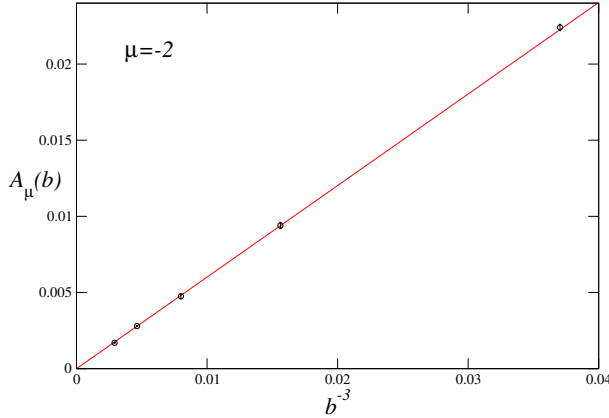


Figure 3.23: Liouvillian rate coefficient $A_\mu(b)$ versus b^{-3} with constant $\mu = -2$. For $b \geq 3$, we observe that $A_\mu(b)$ is compatible with a power-law dependence of the form $A_\mu(b) = C_\mu/b^3$, where $C_\mu = 0.601(3)$ ($\chi^2/\text{ndof} = 1.0$).

where C_μ is a constant that only depends on the chemical potential μ . Matching arguments with the boundary-dissipation cases surely prompted our guess. Indeed, when $b \propto L$, we expect to recover the leading behavior $\Delta_\lambda \sim L^{-3}$ frequently observed in the literature. Our ansatz is fully supported by the data that we have collected for A_μ in terms of $1/b^3$, as shown in Fig. 3.23¹. Indeed, a straight line with a slope of $C_\mu = 0.601(3)$ describes our data for all values of $b \geq 3$ considered ($\chi^2/\text{ndof} = 1.0$).

We also want to mention a scaling regime observed for $L\Delta_\lambda$ in terms of wL when the latter quantity is kept fixed in the large size limit. In Fig. 3.24, we report our data for $b = 2, \mu = -3$ and $b = 4, \mu = -1$.

¹Systematic error bars reported in the figure have been estimated from the comparison of $A_\mu(b)$ for different lattice sizes $L \geq L_{\min}$ and coupling ranges $w \geq w_{\min}$.

Liouvillian gap at fixed n

Now we start to study the behavior when we keep $n = L/b$ fixed. Since the number of the external baths scales with the system size L , we will apply the third quantization technique, cited above.

The Fig. 3.25 shows that the gap scales as $\Delta_\lambda \sim L^{-3}$ at fixed w in the regime $w > w_*$ (w_* is the maximum point). This scaling is correlated also to the Eq.(3.34) and simple matching arguments.

Referring to Fig. 3.25, when $w < w_*$ the gap does not show a uniform limit for $w \rightarrow 0^+$ as the maximum of $L^3\Delta_\lambda$ grows without bounds with increasing L . We shed some light on this peculiar trend in Fig. 3.26, considering the structure of the gap in the proximity of $w = 0$ at fixed $n = 10$ and $\mu = -1$. In fact, the plot supports the existence of a scaling regime for $L^2\Delta_\lambda$ when w is properly rescaled as $w \sim 1/L$. Scaling corrections are also compatible with a decaying L^{-2} , as shown in the corresponding inset. We stress again that numerical results for different values of μ do not exhibit remarkable differences. We conclude that the different scaling regimes shown by the Liouvillian gap do not depend either on μ or the quantum phase related to the Kitaev model.

3.4.2 Dynamic FSS Framework

In this section, we study the time evolution of the Kitaev ring in the proximity of a CQT. To this end, we exploit a dynamic FSS framework and use RG arguments to describe the evolution of the critical correlations. Concerning the algorithms adopted, we speed up our simulations by moving to the momentum basis every time we maintain b fixed. On the other hand, when n is fixed, we just monitor the evolution of the two-point correlation functions by solving a closed system of differential equations. To evolve the density matrix ρ in time, we use standard 4th-order Runge-Kutta techniques with typical integration time steps of $\Delta t = 0.01$.

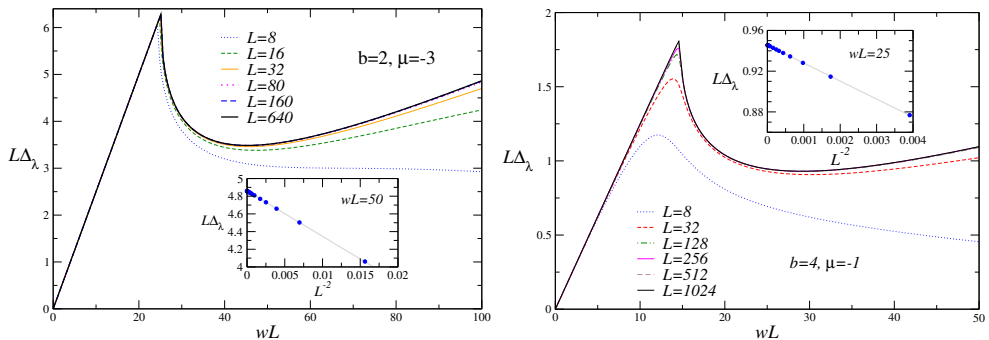


Figure 3.24: Scaling of $L\Delta_\lambda$ versus wL for different values of b and μ . On the top panel, we show results for $b = 2$ and $\mu = -3$, while on the bottom panel, we fix $b = 4$ and $\mu = -1$. The figures show an excellent data collapse in agreement with L^{-2} scaling corrections. The straight lines in the insets are drawn to guide the eye.

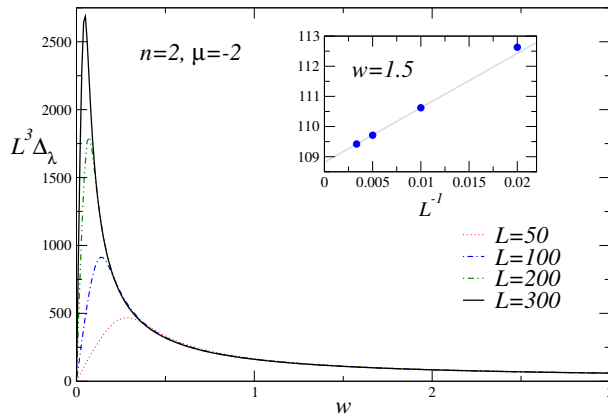


Figure 3.25: Plot of the rescaled gap $L^3 \Delta_\lambda$ in terms of w for fixed $n = 2$ and $\mu = -2$. At fixed w , the gap shows a nice data collapse within L^{-1} scaling corrections, as provided by the inset for the case $w = 1.5$. The straight line is drawn to guide the eye.

The quench protocol and the monitored observables

We now present the quench protocol considered to study the time evolution of the open quantum system under scrutiny at CQTs. We prepare the system in the ground state $|\Omega\rangle$ of Eq. (3.44). The starting chemical potential μ_i is always close to the critical value μ_c , meaning that $|\mu_i - \mu_c| \rightarrow 0$ for $L \rightarrow \infty$. At a reference time $t = 0$, the ring is driven out-of-equilibrium by suddenly coupling the system with the surrounding environment and eventually quenching the chemical potential to a different value $\mu_i \rightarrow \mu_f$. In such a case, the final μ_f should always be sufficiently close to the critical point.

We monitor the time evolution of the Kitaev ring by considering two distinguished two-point correlation functions $C(x, y, t)$ and $P(x, y, t)$, defined as

$$C(x, y, t) \equiv \text{Tr}[\rho(t)(\hat{c}_x^\dagger \hat{c}_y + \hat{c}_y^\dagger \hat{c}_x)], \quad (3.35)$$

$$P(x, y, t) \equiv \text{Tr}[\rho(t)(\hat{c}_x^\dagger \hat{c}_y^\dagger + \hat{c}_y \hat{c}_x)]. \quad (3.36)$$

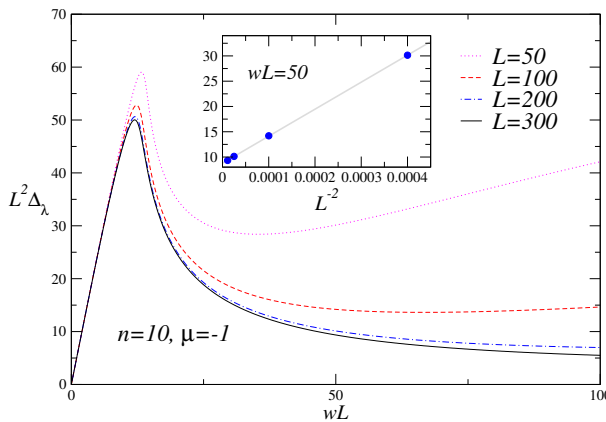


Figure 3.26: The figure shows the Liouvillian gap $L^2 \Delta_\lambda$ versus w at fixed $n = 10$ for $\mu = -1$. In the inset, scaling corrections at $wL = 50$ are consistent with a decay L^{-2} . The straight line is drawn to guide the eye.

3.4.3 Out-of-equilibrium FSS frameworks at CQTs with b fixed

To describe the time evolution of the system under study at CQTs, we employ RG arguments and a dynamic FSS framework [41, 27]. The interplay between the unitary and dissipative dynamics of a Kitaev ring subject to complete bulk dissipation ($b = 1$) has already been addressed in Ref. [107]. The results presented in this section extend the FSS reported in that work to all the cases with fixed $b > 1$, and provide a complementing discussion on the role of Δ_λ in such a regime. Let us first review the main ideas leading to the FSS theory that we are going to discuss.

When we consider the time evolution of an open quantum system after a quench, analogous equations are more involved given the presence of a larger number of scaling quantities and relevant perturbations. First of all, we need to introduce a pre- and a post-quench scaling field $M_{i/f} = (\mu_{i/f} - \mu_c)L^{y_\mu}$ for μ . In the second place, the time variable t requires a scaling field as well. The most natural guess, which also turns out to be the correct one in most cases, is to rescale t with L on the basis of the dynamic critical exponent z . We then introduce the quantity Θ defined as

$$\Theta = tL^{-z}, \quad z = 1, \quad (3.37)$$

which is maintained constant in the FSS limit. Since the number of particle-decay jump operators increases as L , we also need to soften the coupling w to observe an interplay between the critical and dissipative modes. We note that the parameter w plays the role of a decay rate, namely, it is an inverse relaxation time [107, 26]. In our work hypothesis, we then suppose that w should be rescaled with L^{-z} to observe universal FSS relations. We introduce the scaling field γ_b as

$$\gamma_b = \frac{wL^z}{b}, \quad z = 1. \quad (3.38)$$

Naturally, the prefactor b^{-1} appearing in γ_b is just a matter of convention if one restricts the analysis to just one value of b . However, the comparison between different values of b in the FSS limit may add new valuable insights to our analyses. To compare the dissipative processes of different rings on the same footing, we assume that the effective coupling strength is w/b . This choice is the most natural one considering the Kitaev ring in momentum space.

The universal scaling relations satisfied by the two-point functions C and P in Eq. (3.36) follows

$$C(x, y, t) \approx L^{-2y_c} \mathcal{C}(M_i, M_f, \{X_i\}, \Theta, \gamma_b) \quad (3.39)$$

$$P(x, y, t) \approx L^{-2y_c} \mathcal{P}(M_i, M_f, \{X_i\}, \Theta, \gamma_b), \quad (3.40)$$

where $y_c = 1/2$ is the scaling dimension of both \hat{c} and \hat{c}^\dagger . In Fig. 3.27 we show the scaling of $LC(X, Y, t)$ in terms of the scaling quantity Θ for $b = 2$, $M_i = 1$, $M_f = -1$, and $\gamma_b = 1$. The panel definitely supports the FSS laws exhibited in Eq. (3.39). In the inset, we show that the amplitude of the oscillations reduces at fixed Θ and increasing L , roughly as $\sim L^{-1/2}$. We have checked that Eq. (3.40) holds also for the scaling of the RG invariant quantity $LP(X, Y, t)$ (not shown).

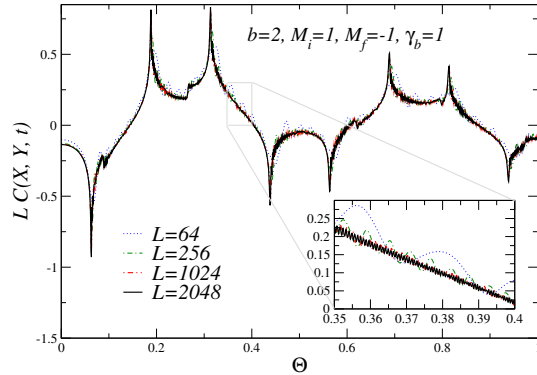


Figure 3.27: Scaling of the two-point function $LC(X, Y)$ in terms of the scaling variable Θ for fixed $b = 2$, $M_i = 1$ and $\gamma_b = 1$. We consider $(Y - X)/L = 1/4$ and fix $x = 1$, using translation invariance. In the inset, we show a zoom of the region $\Theta \in [0.35, 0.4]$. Our data clearly support the FSS laws exhibited in Eq.(3.39).

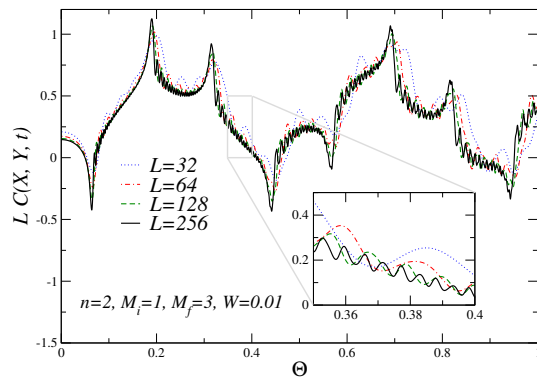


Figure 3.28: Scaling of the rescaled two-point correlation function $LC(X, Y)$ in terms of Θ for fixed of $n = 2$, $M_i = 1$, $M_f = 3$, and $W = 0.01$. We consider $Y - X = L/4$, exploiting translation invariance, and fix the first site to $x = 1$ in conjunction with a dissipator. We zoom in on the domain $\Theta \in [0.35, 0.4]$ to emphasize the convergence of different curves with increasing lattice size L .

3.4.4 Out-of-equilibrium FSS framework at CQTs with n fixed

In this section, we derive a dynamic FSS framework at CQTs to study the time evolution of Eq. (1.4) when the number of the dissipators n is fixed. Most of the scaling relations of the last section are still valid at fixed n with straightforward generalizations. In particular, we just replace the coupling w in our relations, which now represents a decay rate per unit space since $b \sim L$. As a working hypothesis, we expect the scaling field W , defined as

$$W = wL^{z-1}, \quad z = 1, \quad (3.41)$$

to be a reasonable scaling quantity in the FSS limit. For instance, the critical correlations satisfy scaling relations similar to the ones reported in Eq. (3.39)

$$C(x, y, t) \approx L^{-2y_c} \mathcal{C}(M_i, M_f, \{X_i\}, \Theta, W) \quad (3.42)$$

$$P(x, y, t) \approx L^{-2y_c} \mathcal{P}(M_i, M_f, \{X_i\}, \Theta, W). \quad (3.43)$$

We verify our hypotheses in Fig. 3.28, showing the scaling curve for $LC(X, Y, t)$ versus the scaling variable Θ with constant $n = 2, M_i = 1, M_f = 3, W = 0.01$. We obtain a nice data collapse considering lattice sizes up to $L = 256$. The oscillation amplitudes shrink with increasing L , converging to a universal asymptotic curve \mathcal{C} . The validity of Eq. (3.43) has been checked also by inspecting the time evolution of $LP(X, Y, t)$ (not shown).

3.5 Thermal-bath effects in quantum quenches

3.5.1 The fermionic Kitaev chain

We consider fermionic Kitaev wires of L sites with open boundary conditions, whose quantum unitary dynamics is driven by the Hamiltonian [58]

$$\hat{H}_K = -J \sum_{x=1}^{L-1} (\hat{c}_x^\dagger \hat{c}_{x+1} + \hat{c}_x^\dagger \hat{c}_{x+1}^\dagger + \text{h.c.}) - \mu \sum_{x=1}^L \hat{n}_x, \quad (3.44)$$

where \hat{c}_x is the fermionic annihilation operator associated with the site x of the chain, $\hat{n}_x \equiv \hat{c}_x^\dagger \hat{c}_x$ is the particle density operator. In the following we assume J as the energy scale, thus we set $J = 1$.

The Hamiltonian (3.44) can be mapped into a quantum Ising chain, by means of the Jordan-Wigner transformation, see, e.g., Ref. [42]. The corresponding spin model is the quantum Ising chain with open boundary conditions, i.e.

$$\hat{H}_{\text{Is}} = - \sum_{x=1}^{L-1} \hat{\sigma}_x^{(1)} \hat{\sigma}_{x+1}^{(1)} - g \sum_{x=1}^L \hat{\sigma}_x^{(3)}, \quad (3.45)$$

$\hat{\sigma}_x^{(k)}$ being the Pauli matrices and $g = -\mu/2$. In the following we prefer to stick with the Kitaev quantum wire, because the thermal baths and observables that we consider are best defined within the fermionic model. However, the general scaling scenarios that will emerge apply to both models.

The Kitaev model undergoes a CQT at $\mu = \mu_c = -2$ (corresponding to $g = g_c = 1$ in the quantum Ising chain), between a disordered quantum phase for $\mu < \mu_c$ (corresponding to $g > 1$) and an ordered quantum phase for $|\mu| < |\mu_c|$ (corresponding to $|g| < 1$). Thus, we define

$$w = \mu - \mu_c = \mu + 2, \quad (3.46)$$

so that one can easily see the correspondence between the Kitaev Hamiltonian (3.44) and the generic one reported in Eq. (1), i.e. \hat{H}_c corresponds to the Hamiltonian (3.44) for $\mu = \mu_c$, and $\hat{H}_p = -\sum_{x=1}^L \hat{n}_x$. The continuous transition at $w = w_c$ belongs to the two-dimensional Ising universality class [42, 53], characterized by the length-scale critical exponent $\nu = 1$, related to the RG dimension $y_w = 1/\nu = 1$ of the Hamiltonian parameter w . This implies that, approaching the critical point, the length scale ξ of the critical quantum fluctuations diverges as $\xi \sim |w|^{-\nu}$. The dynamic exponent $z = 1$ associated with the unitary quantum dynamics can be obtained from the power law $\Delta \sim \xi^{-z}$ of the vanishing gap with increasing ξ . Moreover, the RG dimension of the fermionic operators \hat{c}_j and \hat{c}_j^\dagger at the CQT is $y_c = 1/2$, and that of the particle density operator \hat{n}_x is $y_n = 1$ [42, 53].

3.5.2 Modelization of the thermal bath

In our study we consider a modelization of interaction with a thermal bath within the Lindblad master equation (1.4), whose asymptotic large-time behavior leads to a Gibbs density matrix at a given finite temperature T . In particular, we consider the proposal developed in Ref. [112] which applies to quantum models described by quadratic Hamiltonians, such as that of the fermionic Kitaev wires. This provides a relatively simple modelization of a thermal bath leading to thermalization in the large-time limit of the corresponding Lindblad master equation for the density matrix of the system.

The Kitaev Hamiltonian (3.44) with open boundary conditions can be diagonalized in the Nambu field space by a Bogoliubov transformation, see e.g. Refs. [59, 140, 112], so that we can rewrite it as

$$\hat{H}_K = \sum_{k=1}^L \omega_k \hat{b}_k^\dagger \hat{b}_k, \quad (3.47)$$

where ω_k are values of the spectrum of the Bogoliubov eigenoperators \hat{b}_k (we are neglecting an irrelevant constant term). Note that both ω_k and \hat{b}_k depend on the Hamiltonian parameter μ . The relation between the fermionic operators \hat{c}_x and the Bogoliubov eigenoperators \hat{b}_k can be generally written as [59, 140, 112]

$$\hat{c}_x = \sum_{k=1}^L A_{xk} \hat{b}_k + B_{xk} \hat{b}_k^\dagger, \quad (3.48)$$

where A and B are appropriate $L \times L$ matrices depending on μ . Following Refs. [112, 141], we write the dissipator $\mathbb{D}_T[\rho]$ in the Lindblad master equation (1.4) in terms of the Bogoliubov eigenoperators as

$$\begin{aligned} \mathbb{D}_T[\rho] &= \sum_k [1 - f(\omega_k, T)] \left(2 \hat{b}_k \rho \hat{b}_k^\dagger - \{\hat{b}_k^\dagger \hat{b}_k, \rho\} \right) \\ &+ \sum_k f(\omega_k, T) \left(2 \hat{b}_k^\dagger \rho \hat{b}_k - \{\hat{b}_k \hat{b}_k^\dagger, \rho\} \right), \end{aligned} \quad (3.49)$$

where

$$f(\omega_k, T) = (1 + e^{\omega_k/T})^{-1}. \quad (3.50)$$

When using this homogeneous dissipator term, the Lindblad master equation (1.4) ensures the asymptotic large-time thermalization [112]. Therefore,

$$\lim_{t \rightarrow \infty} \rho(t) = \rho_t(w, T), \quad (3.51)$$

$$\rho_t(w, T) = \sum_n e^{-E_n(w)/T} |\Phi_n, w\rangle \langle \Phi_n, w|, \quad (3.52)$$

where $\rho_t(w, T)$ is the density matrix representing the thermal state, $E_n(w)$ and $|\Phi_n, w\rangle$ are the eigenvalues and eigenstates of $\hat{H}(w)$. The asymptotic approach to the thermal distribution is controlled by the decay-rate parameter γ [112]. Indeed the Liouvillian gap $\Delta_{\mathcal{L}}$ that controls the exponential approach to the asymptotic stationary state of the Lindblad equation is proportional to the decay rate γ , i.e.

$$\Delta_{\mathcal{L}} \sim \gamma. \quad (3.53)$$

The above modelization of thermal baths provides a useful theoretical laboratory to investigate issues related to the out-of-equilibrium dynamics in the presence of thermal baths. Its derivation has been thoroughly discussed in Ref. [112]. We also mention that it has been employed in Refs. [141, 142]. Some details of the computations using the Lindblad master equation (1.4) with the dissipator (3.49) are reported in the appendix.

3.5.3 Quantum-quench protocols

We consider two protocols, differing for the absence or presence of the contact with the thermal bath during the quantum evolution after quenching, giving respectively rise to unitary or dissipative dynamics after quenching. We call them *unitary* and *dissipative* QQ protocols, respectively.

- *Unitary* QQ protocol: In this simplest QQ protocol the role of the thermal bath is limited to that of preparing the initial Gibbs state $\rho_t(w_i, T)$ at $t = 0$, reported in Eq. (1.2) with ρ_0 . This can be obtained by keeping the thermal bath in contact with the system for a sufficiently long time t_{th} , i.e. $t_{\text{th}} \gg \gamma^{-1}$. Then at $t = 0$ the Hamiltonian parameter is instantaneously quenched from $w_i < 0$ to $w \geq 0$ and the thermal bath is removed, so that the subsequent time evolution is that of a closed fermionic wire, i.e. it is unitary and only driven by the Hamiltonian of the system.
- *Dissipative* QQ protocol: The quantum evolution starts from the same initial Gibbs state $\rho_t(w_i, T)$, but the thermal bath is maintained in contact with the system after the QQ from $w_i < 0$ to $w \geq 0$, at $t = 0$. Therefore, the quantum evolution for $t > 0$ is driven by the Lindblad master equation (1.4) with the dissipator term (3.49). Note that this dynamic protocol entails a further time scale $\tau = \gamma^{-1}$, characterizing the asymptotic exponential approach to the large-time stationary Gibbs state associated with the Hamiltonian $\hat{H}(w)$ and temperature T .

3.5.4 Observables monitoring the time evolution

To characterize the dynamic properties of the quantum evolution after the QQ at $t = 0$, we consider the subtracted particle-density average

$$n_s(t, L) = \frac{1}{L} \text{Tr} \left[\rho(t) \sum_{x=1}^L \hat{n}_x \right] - n_c(L), \quad (3.54)$$

where $n_c(L)$ is the ground-state energy density of the Kitaev wire of size L at the critical point $w_c = 0$ (in the infinite-size limit $n_c = 1/2 - 1/\pi$ [59]). Note that the particle density operator \hat{n}_x and the transverse spin component $\hat{\sigma}_x^{(3)}$ of the quantum Ising chain (3.45) are trivially related, indeed $\hat{\sigma}_x^{(3)} = 2\hat{n}_x$. In the definition of n_s , the subtraction of $n_c(L)$ simplifies the scaling behavior of $n_s(t, L)$ within the critical regime, cancelling the leading analytical behavior [44, 53]. To monitor the spatial correlations, we also consider

$$P(x, y, t) = \text{Tr}[\rho(t) (\hat{c}_x^\dagger \hat{c}_y^\dagger + \hat{c}_y \hat{c}_x)], \quad (3.55)$$

$$C(x, y, t) = \text{Tr}[\rho(t) (\hat{c}_x^\dagger \hat{c}_y + \hat{c}_y^\dagger \hat{c}_x)]. \quad (3.56)$$

Some details on the computation of the above quantities during the time evolution of the QQ protocols are reported in the appendix.

3.5.5 Out-of-equilibrium scaling

We now discuss the out-of-equilibrium behaviors arising from the QQ protocols outlined in Sec. 3.5.3. We show that they develop OFSS behaviors where the effects of the thermal baths are taken into account by appropriate extensions of the out-of-equilibrium zero-temperature scaling laws describing soft QCs in closed systems within their critical regime, already put forward by earlier works [143, 53].

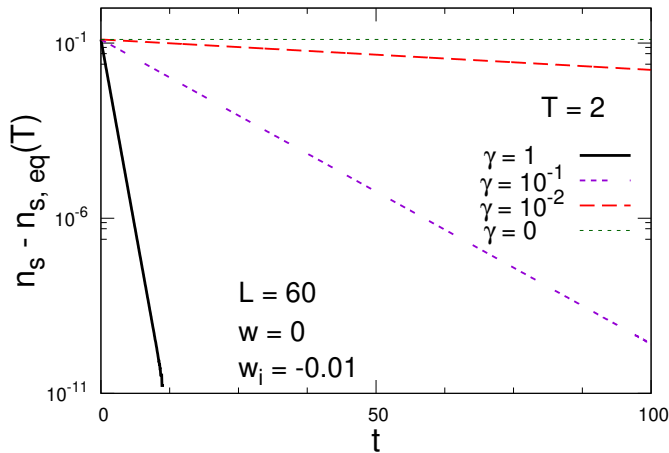


Figure 3.29: The quantum evolution of the subtracted particle density $n_s(t)$, cf. Eq. (3.54), for the dissipative QQ protocol entailing a dissipative dynamics after the QQ at $t = 0$ of the Hamiltonian parameter w , describing the persistent interaction with the thermal bath, cf. Eqs. (1.4) and (3.49). These curves refer to a system of size $L = 60$, temperature $T = 2$ of the thermal bath, quenching from $w_i = -0.01$ to $w = 0$, and various values of the decay rate γ (the case $\gamma = 0$ corresponds to the evolution of the close system). We plot the difference $n_s(t, L, T) - n_{s,eq}(L, T)$ which is expected to vanish in the large-time limit. In this figure and in the following ones, the unity that we use are such that $\hbar = 1$, $k_B = 1$, and $J = 1$.

The OFSS behaviors that we put forward for QQ protocols considered are verified by numerical computations for the fermionic Kitaev wire up to relatively large sizes. See the appendix for details on such calculations.

As a preliminary example of out-of-equilibrium QQ behaviors that we want to address, in Fig. 3.29 we show some results for the quantum evolution of the subtracted particle density (3.54) along the dissipative protocol outlined in Sec. 3.5.3, after quenching a fermionic Kitaev wire of size $L = 60$, from $w_i = -0.01$ to $w = 0$, in the presence of a thermal bath at a temperature $T = 2$, and various values of the decay rate γ . The quantum evolution turns out to have a significant dependence on the decay-rate parameter γ that characterized the interactions between the system and the thermal bath. Indeed, the curves of the subtracted particle density appear to approach its equilibrium value $n_{s,eq}(w = 0, T = 2) \approx 0.0004601\dots$ (while at $t = 0$ we have $n_{s,eq}(w = w_i, T = 2) \approx 0.126598\dots$), faster and faster with increasing γ , actually exponentially as $\exp(-t/\tau)$ with $\tau \sim \gamma^{-1}$, confirming

the role of decay rate of the parameter γ within the Lindblad master equation, cf. Eq. (3.53). Analogous results are obtained for other observables, such as fermionic correlation functions defined in Sec. 3.5.4. In the following we put forward an out-of-equilibrium scaling theory for these out-of-equilibrium phenomena within the quantum critical regime.

Zero-temperature scaling in quantum quenches

We now provide a brief summary of the out-of-equilibrium scaling theory for close systems, describing QQ protocols within the critical regime [143, 53]. The initial state is the ground state associated with an initial value $w_i < 0$, and, after the instantaneous quench at $t = 0$ from w_i to w , the quantum evolution is driven by the Schrödinger equation.

Out-of-equilibrium scaling laws can be obtained by extending those valid at equilibrium, allowing for a time dependence essentially controlled by the time scaling variable $\Theta \sim t \Delta$, which is obtained by assuming that the relevant time scale of the critical modes is proportional to the inverse energy difference Δ of the lowest states. We refer to Ref. [53] for a through presentation of the scaling arguments leading to the asymptotic OFSS behaviors.

Let us consider the out-of-equilibrium evolution (after quenching) of generic observables, such as the expectation value O at time t of a local operator $\hat{O}(\mathbf{x})$ and its fixed-time correlations $G_O = \langle \hat{O}(\mathbf{x})\hat{O}(\mathbf{y}) \rangle$. The general working hypothesis underlying out-of-equilibrium FSS frameworks is that the expectation value of $\hat{O}(\mathbf{x})$ and its correlation functions obey asymptotic homogeneous scaling laws [53], such as

$$O(t, \mathbf{x}, L, w_i, w) \approx b^{-y_o} \mathcal{O}(t/b^z, \mathbf{x}/b, L/b, b^{y_w} w_i, b^{y_w} w), \quad (3.57)$$

where b is an arbitrary (large) length scale, y_o is the RG dimension of the local operator $\hat{O}_{\mathbf{x}}$ and the RG exponents y_w and z are determined by the universality class of the CQT (they are the RG dimensions of the Hamiltonian parameter w and the temperature T , respectively). Thus both the initial and final values of w , i.e. w_i and w , take the same RG exponent y_w , being coupled to the RG perturbation \hat{H}_p within the Hamiltonian. Note that we do not assume translation invariance, which is generally broken by the presence of boundaries, such as those arising from open boundary conditions.

OFSS can be straightforwardly derived by fixing $b = L$ in the above homogeneous scaling law. Then, we expect the OFSS of the expectation value O of a generic local operator $\hat{O}_{\mathbf{x}}$, of its spatial average $\hat{O}_a = L^{-d} \sum_{\mathbf{x}} \hat{O}_{\mathbf{x}}$, and its two-point correlation function G_O , develop the asymptotic OFSS behavior [143, 53]

$$\begin{aligned} O(t, \mathbf{x}, L, w_i, w) &\approx L^{-y_o} \mathcal{O}(\Theta, \mathbf{X}, \Phi_i, \Phi), \\ O_a(t, L, w_i, w) &\approx L^{-y_o} \mathcal{O}_a(\Theta, \Phi_i, \Phi), \\ G_O(t, \mathbf{x}_1, \mathbf{x}_2, L, w_i, w) &\approx L^{-2y_o} \mathcal{G}_O(\Theta, \mathbf{X}_1, \mathbf{X}_2, \Phi_i, \Phi), \end{aligned} \quad (3.58)$$

where the scaling variables appearing in the scaling functions \mathcal{O} , \mathcal{O}_a , and \mathcal{G}_O are defined as

$$\Theta \equiv \frac{t}{L^z}, \quad \mathbf{X}_i \equiv \frac{\mathbf{x}_i}{L}, \quad \Phi_i \equiv L^{y_w} w_i, \quad \Phi \equiv L^{y_w} w. \quad (3.59)$$

The OFSS limit is obtained in the large- L and large- t limit keeping the above scaling variables fixed. These conditions ensure that the system remains within

the universal critical regime during the quantum evolution. Note that in the scaling law (3.59) the dynamic features are essentially encoded in the time dependence of the scaling variable $\Theta \sim t\Delta$. The other features, in particular when $w_i = w$, are analogous to those arising from equilibrium FSS at CQTs [44, 53], where the argument $\Phi = L^{y_w}w$ of the scaling functions is controlled by the RG dimension y_w of the relevant parameters w at the RG fixed point associated with the CQT.

The above OFSS equations can be straightforwardly applied to the observables defined in Sec. 3.5.4, after a quench from w_i to w at $t = 0$, keeping into account that the RG dimension of the subtracted particle density is $y_n = 1$, and that of the fermionic operator \hat{c}_x is $y_c = 1/2$. Note that the dominant analytical contributions to the particle density [44, 53] coming from the analytical background are canceled in the difference n_s defined in Eq. (3.54), whose leading asymptotic behavior arises from the quantum critical modes, therefore it is analogous to that of O_a in Eq. (3.58), with $y_o = y_n$. Analogously one can apply the OFSS in Eq. (3.58) to observables and correlation functions constructed with the spin operators of the quantum spin chain (3.45). The OFSS functions are expected to be universal with respect to the microscopic details of the model, apart from nonuniversal multiplicative rescaling and normalizations of its arguments. Within isolated fermionic Kitaev wires and quantum Ising chains, the OFSS arising from soft QQs has been verified by numerical computations for various boundary conditions, and also along their quantum first-order transition line [143, 53].

The OFSS limit is expected to be approached with power-law suppressed corrections. There are various sources of scaling corrections when approaching the OFSS. Of course, they include those that are already present at equilibrium. In particular, the irrelevant RG perturbations are sources of scaling corrections for the asymptotic behavior of the free-energy density [43, 53]. In the case of one-dimensional quantum systems undergoing CQTs belonging to the two-dimensional Ising universality class, the leading scaling corrections from irrelevant RG perturbations are suppressed as $L^{-\omega}$ with $\omega = 2$ [74, 44]. However, other contributions may become more relevant [43, 44, 53], such as those arising from the presence of analytical backgrounds, from the presence of boundaries (which generally gives rise to $O(1/L)$ corrections), and, in the case of correlation functions, from RG mixings of the source fields [this for example happens in the case of the correlation functions of the fermionic field \hat{c}_x , for which corrections are $O(1/L)$]. These scaling corrections have been confirmed by numerical results [44, 53]. Therefore, we expect that the asymptotic OFSS of fermionic Kitaev wires and quantum Ising chains with open boundary conditions is generally approached with $O(1/L)$ corrections.

OFSS along the unitary QQ protocol

For the simplest unitary protocol reported in Sec. 3.5.3, where the quantum evolution is that of the isolated fermionic wire, the request that the dynamics remains within the critical regime implies that the temperature of the initial Gibbs state must be appropriately suppressed in the large- L OFSS limit, to obtain a nontrivial out-of-equilibrium critical limit. This is analogous to what happens within the equilibrium FSS, where one introduces the scaling variable [144, 42, 53]

$$\Xi \equiv L^z T, \quad (3.60)$$

to allow for a nonzero temperature in the FSS of the observables. Therefore, like equilibrium FSS, we conjecture that the temperature of the initial Gibbs state enters the OFSS associated with the unitary QQ protocol by adding a further dependence on Ξ in the scaling functions (3.58). In other words, a nontrivial asymptotic OFSS limit is expected to be realized in the large- L and large- t limits keeping also Ξ fixed, beside the scaling variables already defined in Eq. (3.59). Therefore, we expect that the OFSS of standard QQ protocols starting from ground states, cf. Eq. (3.58), changes into

$$O(t, \mathbf{x}, L, w_i, w, T) \approx L^{-y_o} \mathcal{O}(\Theta, \mathbf{X}, \Phi_i, \Phi, \Xi), \quad (3.61)$$

and analogously for its spatial average O_a and the correlation function G_O .

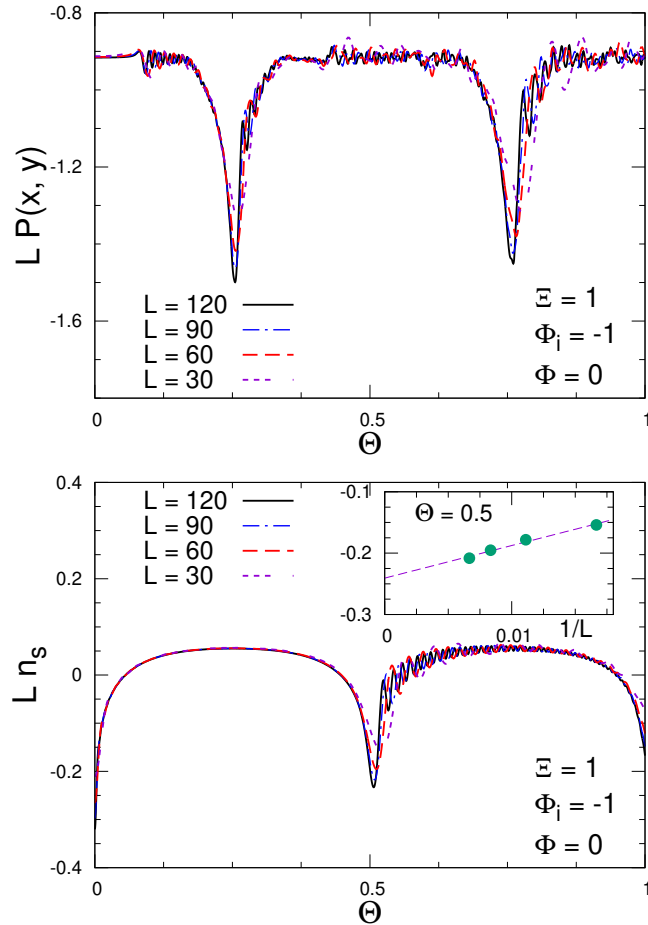


Figure 3.30: OFSS behavior of the subtracted particle density (bottom) and the fermionic correlation function $P(x = L/3, y = 2L/3, t)$, cf. Eq. (3.55), arising from the unitary QQ protocol, for various lattice sizes L , at fixed $\Xi = L^z T = 1$, $\Phi_i = L^{y_w} w_i = -1$ and $\Phi = L^{y_w} w = 0$, versus the time scaling variable $\Theta = t/L^z$. These computations nicely support the OFSS behaviors reported in Eq. (3.61). The inset of the bottom figure shows that the approach to the OFSS limit is consistent with $O(1/L)$ corrections. Analogous results are obtained for other values of the scaling variables.

The numerical analysis for the fermionic Kitaev wire under the unitary protocol fully support to this OFSS, obtained by extending the QQ FSS behaviors of closed

systems starting from an initial ground state. This is clearly demonstrated by the curves reported in Fig. 3.30, associated with the quantum evolutions of the subtracted particle density $n_s(t)$ and the fermionic correlation $P(x, y, t)$ (the other fermionic correlation $C(x, y, t)$ develops an analogous OFSS).

OFSS along the dissipative QQ protocol

We now discuss the dynamics arising from the dissipative protocol outlined in Sec. 3.5.3, when the quantum evolution after quenching is described by the Lindblad master equation (1.4) with the thermal-like dissipator (3.49), to modelize the interaction with a thermal bath characterized by a temperature T (which does not change after quenching) and decay rate γ .

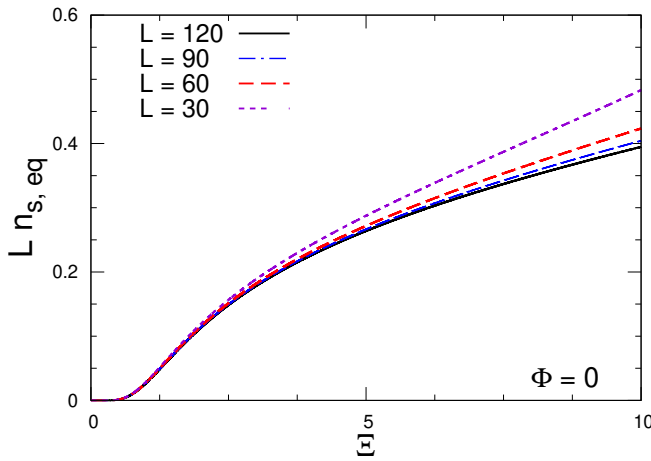


Figure 3.31: Equilibrium FSS of the subtracted particle density $n_{s,\text{eq}}$ at the critical point $w = 0$, versus the rescaled temperature $\Xi = L^z T$. With increasing L , the data show the expected convergence to the equilibrium FSS reported in Eq. (3.63) with $y_n = 1$.

We expect that the temperature T of the thermal bath must be rescaled as in the case of the unitary QQ protocol, i.e. we must consider again the associated scaling variable Ξ already defined in Eq. (3.60). However, since the QQ moves the system out-of-equilibrium, also the decay rate γ , and corresponding time scale $\tau = \gamma^{-1}$, associated with the interactions with the thermal bath is expected to play a relevant role to establish a corresponding nontrivial OFSS limit. This was already noted in Ref. [142] in the analysis of dynamic protocols entailing the variation of the temperature at the critical point.

When keeping τ constant in the FSS limit where the scaling variable $\Theta = t/L^z$ is kept fixed, in the large- L limit we have eventually that

$$t = \Theta L^z \gg \tau, \quad (3.62)$$

which is the condition ensuring thermalization for any finite value $\Theta > 0$. Therefore, when keeping τ fixed, the quantum evolution is not expected to develop a nontrivial OFSS limit. Indeed, in the large- L limit, the system turns out to suddenly approach an equilibrium Gibbs state (associated with the Hamiltonian parameter w and temperature T) with respect to the rescaled time Θ , without

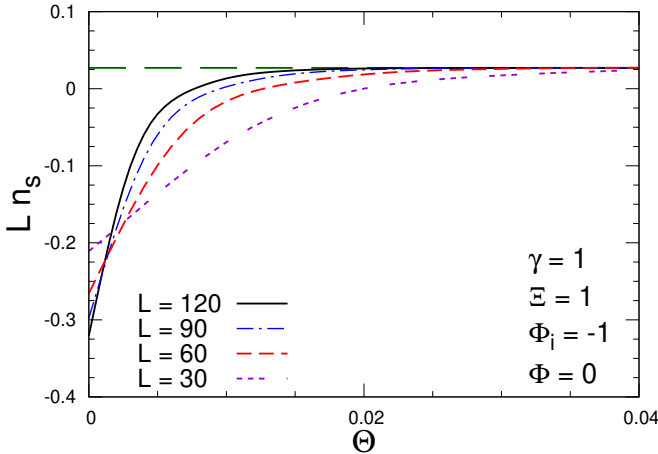


Figure 3.32: Quantum evolution of the subtracted particle density arising from the dissipative QQ protocol, when rescaling all quantities involved in the quench protocol, except for the decay rate γ . With increasing L , the curves appear to approach the equilibrium FSS value at finite temperature (where the temperature dependence enters through the scaling variable $\Xi = L^z T$) faster and faster, reflecting a nonuniform convergence for any $\Theta > 0$. The dashed line shows the equilibrium value of n_s for $\Phi = 0$ and $\Xi = 1$, which is asymptotically approached by the various curves.

any further relevant evolution of the system for any $\Theta > 0$. Therefore, if the temperature is rescaled by keeping $\Xi = L^z T$ fixed, we must recover the equilibrium FSS behavior in the presence of a thermal bath at temperature T , such as that associated with the subtracted particle density [44, 53]

$$n_{s,\text{eq}}(w, L, T) \approx L^{-y_n} \mathcal{N}(\Phi, \Xi), \quad (3.63)$$

where $\Phi = L^{y_w} w$, and the temperature dependence enters through the associated scaling variable $\Xi = L^z T$. In Fig. 3.31 we show some equilibrium data at the critical point $w = \Phi = 0$, versus Ξ , showing the approach to the asymptotic large- L equilibrium FSS (3.63). The realization of the equilibrium FSS within the QQ protocol at fixed γ is demonstrated by the plots reported in Fig. 3.32, which show the somewhat trivial convergence toward the equilibrium FSS for any finite $\Theta > 0$.

The above results suggest that also the the decay rate γ of the system-bath interactions must be rescaled to observe a nontrivial OFSS limit as a function of the time scaling variable Θ , to create the conditions for a balanced competition between the critical Hamiltonian driving and the interactions with the thermal bath. As already put forward in the case of other homogeneous dissipative terms in the Lindblad equation [107, 73, 36, 53, 138], for example associated with particle-decay or particle-pumping dissipative mechanisms, a nontrivial OFSS limit is obtained by rescaling the decay rate of the dissipative term, so that the scaling variable

$$\Gamma \equiv L^z \gamma \sim \gamma / \Delta \quad (3.64)$$

is kept fixed in the OFSS limit, where Δ is the energy difference of the lowest eigenstates of $\hat{H}(w)$ at the critical point $w = w_c = 0$. Then an OFSS behavior emerges from the nontrivial competition between the critical unitary dynamics and the dissipative driving arising from the thermal bath.

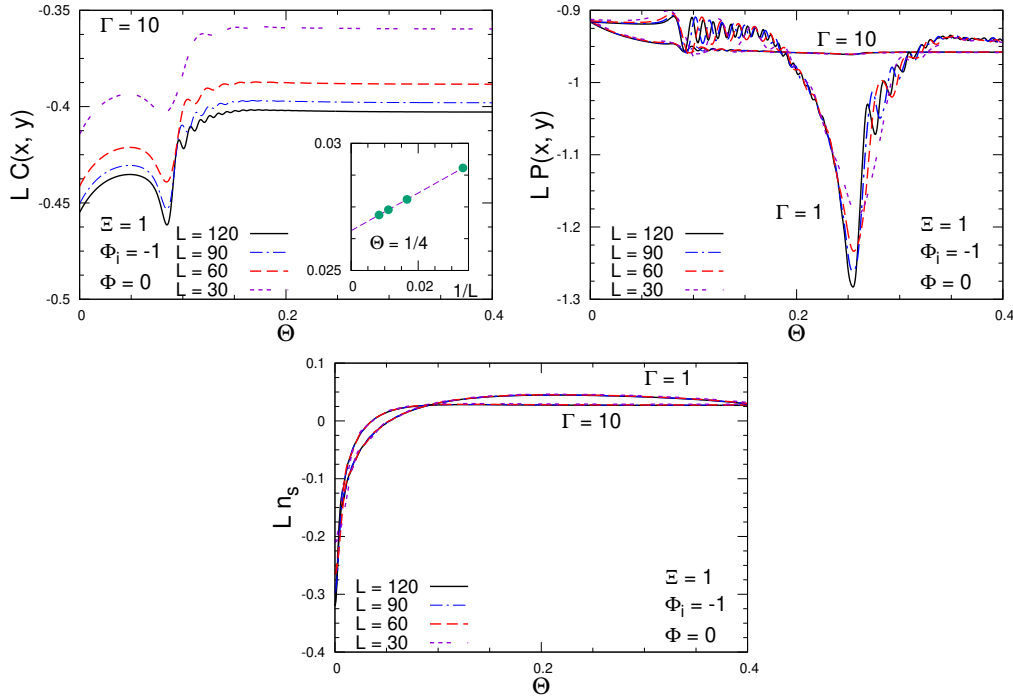


Figure 3.33: Quantum evolutions along the dissipative protocol, fully supporting the OFSS reported in Eqs. (3.65) and (3.66). We report curves for $L n_s$ (bottom), $L P(x = L/3, y = 2L/3, t)$ (middle), and $C(x = L/3, y = 2L/3, t)$ (top), for various values of L , at fixed $\Phi_i = -1$, $\Phi = 0$, $\Xi = 1$, and two values of $\Gamma = L^z \gamma$, i.e. $\Gamma = 1, 10$ (except for the top figure where we only report data for $\Gamma = 10$ to ensure a good readability). The inset of the top figure shows that the OFSS is approached with $O(1/L)$ corrections. Analogous results are obtained for other values of the scaling variables.

In conclusion, on the basis of the above scaling arguments, the OFSS arising from the dissipative QQ protocols in the presence of a thermal bath is expected to be given by

$$O_a(t, L, w_i, w, T, \gamma) \approx L^{-y_o} \mathcal{O}_a(\Theta, \Phi_i, \Phi, \Xi, \Gamma), \quad (3.65)$$

and

$$\begin{aligned} G_O(t, \mathbf{x}_1, \mathbf{x}_2, L, w_i, w, T, \gamma) \approx \\ L^{-2y_o} \mathcal{G}_O(\Theta, \mathbf{X}_1, \mathbf{X}_2, \Phi_i, \Phi, \Xi, \Gamma). \end{aligned} \quad (3.66)$$

In the large- Γ limit the above OFFS behaviors at fixed Ξ is expected to approach the corresponding equilibrium FSS, faster and faster in terms of Θ , matching the behavior at finite γ . Moreover, we also expect that the equilibrium FSS is also approached in the large- Θ limit at fixed Γ and Ξ , independently of Γ , but faster and faster with increasing Γ .

Again, the numerical results for the particle density $n_s(t)$ and correlation functions P and C fully support the above OFSS equations, i.e. Eq. (3.65) for $n_s(t)$ with $y_o = y_n = 1$, and Eq. (3.66) for P and C with $y_o = y_c = 1/2$. Some results are reported in Fig. 3.33. We also stress that analogous results are expected for other observables, for example the correlation functions of the spin operator of the equivalent formulation provided by the quantum Ising chains.

Chapter 4

Conclusions

We have studied the out-of-equilibrium behavior of many-body systems when their time-dependent Hamiltonian parameters slowly cross phase transition points. In particular, we present an exploratory study of out-of-equilibrium behaviors arising from round-trip protocols across first and second order quantum phase transitions and classical transitions.

The analogy of the scaling behaviors for one-way KZ protocols at classical and quantum transitions is only partially extended to round-trip KZ protocols. Substantial differences emerge, in particular when the extreme value of the outward driving parameter variation is kept fixed and finite in the large- t limit. On the one hand, classical systems show a well-defined dynamic scaling limit, developing scaling hysteresis-like scenarios, essentially because the purely relaxational stochastic dynamics leads eventually to thermalization at fixed model parameters. On the other hand, in quantum systems the observation of scaling behavior along the return way turns out to be more problematic, due to the persistence of rapidly oscillating relative phases between the relevant quantum states. They make the return way extremely sensitive to the parameters of the protocol, such as the extreme driving parameter value and the size of the system. This is essentially related to the quantum nature of the dynamics. Indeed there are some notable similarities with the behavior of quantum two-level models subject to round-trip protocols, analogous the well-known Landau-Zener-Stckelberg problem.

In the FOQT scenario, we formulate the FSS regime as the limit $L \rightarrow \infty$, where the time-dependent expectation values of local observables are proportional to quasi-universal FSS functions of the variables $\tau = t/u$ and $\nu = u\delta^2$. Here, the meaning of quasi-universality stands for the residual dependence of the FSS functions on the details of the driving protocol at the inversion time. Numerical results for the many-body system confirm the validity of our scaling hypothesis. We further probe the validity of the FSS regime using time-dependent perturbation theory, relating it to the emergence of an effective two-level description which involves the lowest two states near the FOQT. With this effective description, we reduce the driving protocol to a series of Landau-Zener transitions and we determine an analytical expression of the FSS functions. Lastly, we extend the setup to the case of periodic driving across the quantum FOQT, and we comment on the validity of the FSS after several crossings.

In the second part, we consider systems where particles are constrained within a limited spatial region by hard walls, and systems where they are trapped by a space-dependent potential, such as an effective harmonic potential. These is-

sues are particularly relevant for cold-atom experiments, where atoms are confined within a limited spatial region by external potentials. Within this class of confined particle systems, we investigate the dynamic features arising from localized particle-loss dissipative mechanisms, which may be controllable, or inevitably present, in the experimental setup. The out-of-equilibrium evolution arising from the protocol considered shows various dynamic regimes, which can be effectively distinguished by relating them to dynamic FSS limits corresponding to different time scales, which can be associated with the gap of the Liouvillian gap of the Lindblad equation, and the gap of its Hamiltonian driving.

To understand the role of this Liouvillian gap, we analyze the interplay between the Liouvillian gap Δ_λ and the gap related to the Kitaev ring Δ in the FSS limit. In particular, we take into account the short- and long-time regimes, focusing on how they join together in the FSS limit. When we keep b fixed, the gap Δ_λ is always finite and depends linearly on the dissipation strength w . Nonetheless, two different regimes emerge for systems of finite size. In the small w region, the gap is given by $\Delta_\lambda = w/(2b)$, whereas, at large w and sufficiently large b , it behaves as $\Delta_\lambda = wC_\mu/b^3$. The last equation always controls the gap in the large-size limit and is our starting point to deduce the scaling of such a quantity when $b \propto L$. It is worth mentioning that we also put forward a scaling regime for $L\Delta_\lambda$ as a function of wL , which ties together the two different regimes outlined in a smooth manner. On the other hand, when we keep the number of dissipators n fixed, the gap vanishes as $\sim L^{-3}$ at large L . Addressing the structure of the gap at small w , we find a scaling regime for $L^2\Delta_\lambda$ in terms of wL , which is closely related to the presence of a non-uniform convergence of $L^3\Delta_\lambda$ in the limit $w \rightarrow 0^+$.

We, also, develop a dynamic FSS regime at CQTs to describe the time evolution of the Kitaev model under investigation. At fixed b , our results extend the homogenous dissipative FSS theory to the cases with $b > 1$. As a working hypothesis, we suppose that the scaling variable associated with the relevant coupling w is $\gamma_b = wL^z/b$. Our numerical results for the two-point correlation functions and the entanglement entropy fully support this ansatz. In the second stage, we compare the real-time evolution of several rings corresponding to different b to get some additional insights into the dissipation mechanisms of these systems. As far as our numerical capabilities allow us to conclude, the entanglement entropy and the P -correlations admit a universal scaling function for all b , but the C -correlations do not. This issue requires further investigations to be better understood. When the number of dissipators n is fixed, the FSS theory outlined at fixed b generalizes straightforwardly after replacing γ_b with $W = wL^{z-1}$. In the last section, we analyze the interplay between the Liouvillian gap Δ_λ and the gap related to the Kitaev ring Δ in the FSS limit. In particular, we take into account the short- and long-time regimes, focusing on how they join together in the FSS limit. When b is fixed, we observe that the link between the two regimes is smooth, whereas, at fixed n , the two regions can be easily distinguished given the presence of different power-law scalings for the gaps Δ and Δ_λ .

Finally, we have reported a study of the effects of thermal baths to the out-of-equilibrium dynamics of many-body systems within their quantum critical regime close to a zero-temperature CQT. Within FSS frameworks, we argue that, when the thermal baths are associated with a sufficiently small temperature, their effects can be taken into account by appropriate extensions of the zero-temperature out-of-equilibrium scaling laws describing soft QCs of isolated systems within the critical

regime. For the unitary QQ protocol, where the thermal bath only determines the initial Gibbs state and the evolution is unitary, a nontrivial OFFS limit is simply obtained by rescaling the temperature as $T \sim L^{-z}$, similarly to equilibrium FSS. Along the dissipative QQ protocol, where the thermal bath is not removed after quenching, the dynamics is more complicated, and the decay rate γ plays a relevant role. Indeed, in addition to the rescaling of the temperature T associated with thermal bath, one also needs to rescale γ as $\gamma \sim L^{-z}$ to obtain a nontrivial FSS. Otherwise, when keeping γ fixed, the dynamics converges toward the equilibrium FSS at finite temperature, which happens suddenly after quenching with respect to the time scale $t_c \sim L^z$ of the critical regime. Therefore the scaling behavior when keeping γ fixed becomes somehow trivial, reproducing the equilibrium FSS for any rescaled time $\Theta = L^{-z}t > 0$ in the large- L limit.

As future outlooks, we mention that the results of the round-trip KZ protocol and of the Liouvillian gap analysis can be extended in several directions. First of all, our studies can be generalized by considering thermal baths in the Lindblad formalism [145] with a round-trip protocol which drives the time evolution. Alternatively, it would be interesting to understand how the different large-size limits considered in this thesis affect the Liouville gap and the FSS regime of open quantum models in higher dimensions. Despite the numerous challenges given by such a quest, we must say that this setting certainly offers attractive questions and new paradigms to be addressed. To name a few, we mention that the NESS, in more than one spatial dimension, may undergo a continuous phase transition, similar to a finite-temperature quantum system at equilibrium. For this reason, the evolutions of open quantum models in the short- and long-time regimes can be associated with different RG fixed points, entailing a more intriguing scenario in the FSS limit.

Appendix A

Round-trip Landau-Zener protocols in two-level models

In this appendix we study time-dependent round-trip protocols within a paradigmatic two-level model, described by the Hamiltonian (2.56). Their quantum evolution is ruled by the Schrödinger equation

$$i \partial_t \Psi(t) = H_{2\ell}(t) \Psi(t), \quad (A.1)$$

$$H_{2\ell}(t) = -\beta(t) \sigma^{(3)} + \frac{\Delta}{2} \sigma^{(1)}.$$

The parameter Δ corresponds to the energy difference of the Hamiltonian eigenstates at $\beta(t) = 0$. To describe the states $\Psi(t)$ of the system, we consider the *adiabatic* basis provided by the eigenvectors $|+\rangle$ and $|-\rangle$ of $\sigma^{(3)}$, with eigenvalues $\lambda = 1$ and $\lambda = -1$ respectively. Therefore, we may write

$$\Psi(t) = \phi_1(t)|+\rangle + \phi_2(t)|-\rangle, \quad (A.2)$$

and define $\Psi(t) \equiv [\phi_1(t), \phi_2(t)]$. It is convenient to define

$$\eta(t) = \frac{2\beta(t)}{\Delta}, \quad (A.3)$$

so that

$$H_{2\ell}(t) = \frac{\Delta}{2} \tilde{H}_{2\ell}(t), \quad \tilde{H}_{2\ell}(t) = -\eta(t) \sigma^{(3)} + \sigma^{(1)}. \quad (A.4)$$

Adiabatic time evolutions, i.e. for sufficiently slow changes of the Hamiltonian parameter $\beta(t)$, pass through the stationary eigenstates of $H_{2\ell}$ at fixed $\beta(t) \equiv \beta \equiv \delta\eta$, which are given by

$$|\Psi_0, \eta\rangle = \mathcal{N}_0(\eta) \left[(-\eta - \sqrt{1 + \eta^2})|+\rangle + |-\rangle \right],$$

$$E_0 = -\frac{\Delta}{2} \sqrt{1 + \eta^2}, \quad (A.5)$$

$$|\Psi_1, \eta\rangle = \mathcal{N}_1(\eta) \left[(-\eta + \sqrt{1 + \eta^2})|+\rangle + |-\rangle \right],$$

$$E_1 = \frac{\Delta}{2} \sqrt{1 + \eta^2}, \quad (A.6)$$

where $\mathcal{N}_i(\eta)$ are appropriate normalizations so that $\langle 0|0\rangle = \langle 1|1\rangle = 1$.

In the following we consider a linear time dependence of the Hamiltonian parameter $\beta(t)$, and round-trip linear protocols. We start at $t_i = -t_*$ from the ground state $|\Psi_0, \eta_i\rangle \equiv [\phi_1^{(0)}, \phi_2^{(0)}]$ of the system for $\beta(t_i)$. Then the system evolves according to the Schrödinger equation (A.1) with $\beta(t)$ given by the Eq. (2.57), i.e. $\beta(t) = \mathcal{T}(t)/t_s$ for $t_i = -t_* \leq t \leq 3t_*$, where $\mathcal{T}(t) = t_* - |t - t_*|$ is the triangular function going linearly from $\mathcal{T}(-t_*) = -t_*$ to $\mathcal{T}(t_*) = t_*$, and then back to $\mathcal{T}(3t_*) = -t_*$. The parameter t_s represents the time scale of the variation. The parameter $t_* > 0$ controls the extension (i.e. the starting and final times) of the protocols, from $t_i = -t_*$ to $t_f = 3t_*$, and also the interval of variation of $\beta(t)$, from $\beta(t_i) = -t_*/t_s$ to $\beta(t_*) = t_*/t_s$.

To solve this problem, it is convenient to introduce the variables

$$\tau = \frac{\mathcal{T}(t)}{\sqrt{t_s}}, \quad \tau_* = \frac{t_*}{\sqrt{t_s}}, \quad v = t_s \Delta^2, \quad (\text{A.7})$$

$$\kappa = \frac{2\tau}{\sqrt{v}} = \frac{2\beta(t)}{\Delta}, \quad \kappa_* = \frac{2\tau_*}{\sqrt{v}}. \quad (\text{A.8})$$

Then the time evolution can be straightforwardly determined using the results of Ref. [79], in terms of parabolic cylinder functions $D_\nu(x)$ [146]. Along the first branch from $-t^*$ to t^* , we write

$$\phi_i^{(1)}(\tau) = U_{ij}(\tau, \tau_i) \phi_j^{(0)}, \quad (\text{A.9})$$

where $\tau = t/\sqrt{t_s}$ with $-t_* \leq t \leq t_*$, $\tau_i = -\tau_*$, and the evolution matrix elements are [79]

$$\begin{aligned} U_{11}(\tau, \tau_i) &= \frac{\Gamma(1 - iv/8)}{\sqrt{2\pi}} \times \\ &\left[D_{iv/8}(\sqrt{2}e^{-i\pi/4}\tau) D_{-1+iv/8}(\sqrt{2}e^{i3\pi/4}\tau_i) + \right. \\ &\left. D_{iv/8}(\sqrt{2}e^{i3\pi/4}\tau) D_{-1+iv/8}(\sqrt{2}e^{-i\pi/4}\tau_i) \right], \\ U_{12}(\tau, \tau_i) &= \frac{2\Gamma(1 - iv/8)e^{i\pi/4}}{\sqrt{\pi v}} \times \\ &\left[-D_{iv/8}(\sqrt{2}e^{-i\pi/4}\tau) D_{iv/8}(\sqrt{2}e^{i3\pi/4}\tau_i) + \right. \\ &\left. D_{iv/8}(\sqrt{2}e^{i3\pi/4}\tau) D_{iv/8}(\sqrt{2}e^{-i\pi/4}\tau_i) \right], \\ U_{21} &= -U_{12}^*, \quad U_{22} = U_{11}^*. \end{aligned} \quad (\text{A.10})$$

Using the properties of the evolution matrix U under the transformation $\beta(t) \rightarrow -\beta(t)$ [79], we can write the evolution for $t > t^*$ as

$$\phi_i^{(2)}(\tau) = V_{ij}(\tau_b, \tau_i) \phi_j^{(1)}(\tau_*), \quad (\text{A.11})$$

where τ is defined as in Eq. (A.7), thus it is decreasing from τ_* to $-\tau_*$, again $\tau_i = -t_*/\sqrt{t_s}$, $\tau_b = t_b/\sqrt{t_s}$ with $t_b = t - 2t_*$, and the functions V_{ij} are closely related to U_{ij} : [79]

$$\begin{aligned} V_{11} &= U_{11}^*, & V_{12} &= -U_{12}^*, \\ V_{22} &= U_{22}^*, & V_{21} &= -U_{21}^*. \end{aligned} \quad (\text{A.12})$$

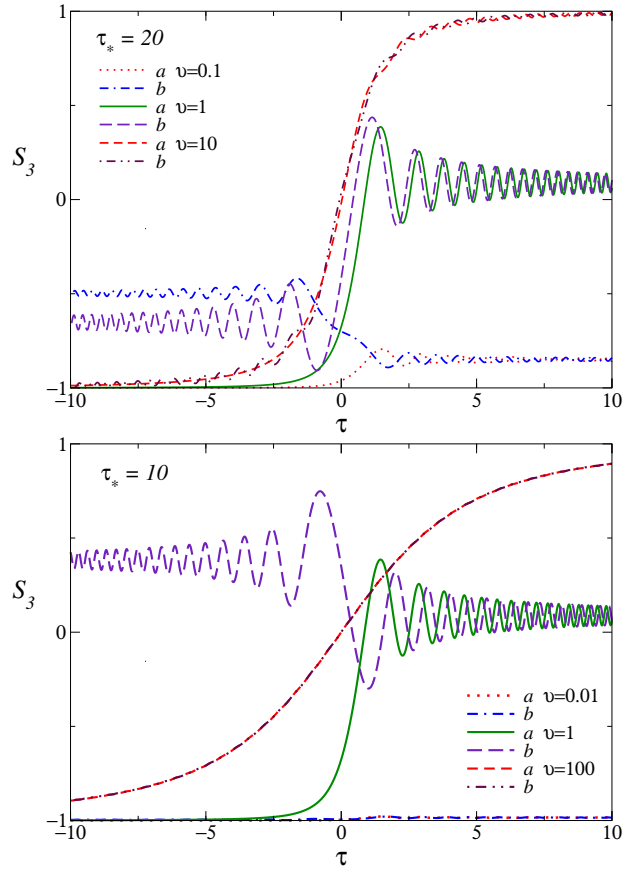


Figure A.1: Evolution of S_3 during the protocol, for $\tau_* = 10$ (bottom) and $\tau_* = 20$ (top), and various values of v .

We have also numerically checked the above analytic expressions for the time evolution along the round-trip protocol.

Since the variable τ related to time takes the same values in the intervals $-t_* \leq t \leq t_*$ and $t_* \leq t \leq 3t_*$, we separate the time dependence in two parts: (a) for the first part where $\beta(t)$ and τ increases, and (b) where $\beta(t)$ and τ decreases. We monitor the dynamic evolution along the protocol defined above by the expectation values of the operators $\sigma^{(k)}$, i.e.

$$S_3^{(a/b)}(v, \tau, \tau_*) = \langle \Psi(t) | \sigma^{(3)} | \Psi(t) \rangle, \quad (\text{A.13})$$

$$S_1^{(a/b)}(v, \tau, \tau_*) = \langle \Psi(t) | \sigma^{(1)} | \Psi(t) \rangle, \quad (\text{A.14})$$

and the adiabaticity function

$$A^{(a/b)}(v, \tau, \tau_*) = |\langle \Psi_0, \eta(t) | \Psi(t) \rangle|. \quad (\text{A.15})$$

Note that the adiabatic limit of the evolution is obtained by sending $v \rightarrow \infty$ keeping fixed κ . Therefore,

$$\lim_{v \rightarrow \infty} A^{(a/b)}(v, \kappa\sqrt{v}/2, \kappa_*\sqrt{v}/2) = 1. \quad (\text{A.16})$$

Some results for the *magnetization* S_3 are shown in Fig. A.1 along the first and second branch of the protocol, for various values of v , $v = 0.01, 1, 10000$, and $\tau_* = 10, 20$. As expected, the case of large v the dynamic tends to be adiabatic, so

that the values of S_3 along the two ways tend to superimpose. In the case of small v the dynamic tends to be frozen to the initial condition, moving only slightly from the initial value. More complex behaviors are observed for intermediate values of v .

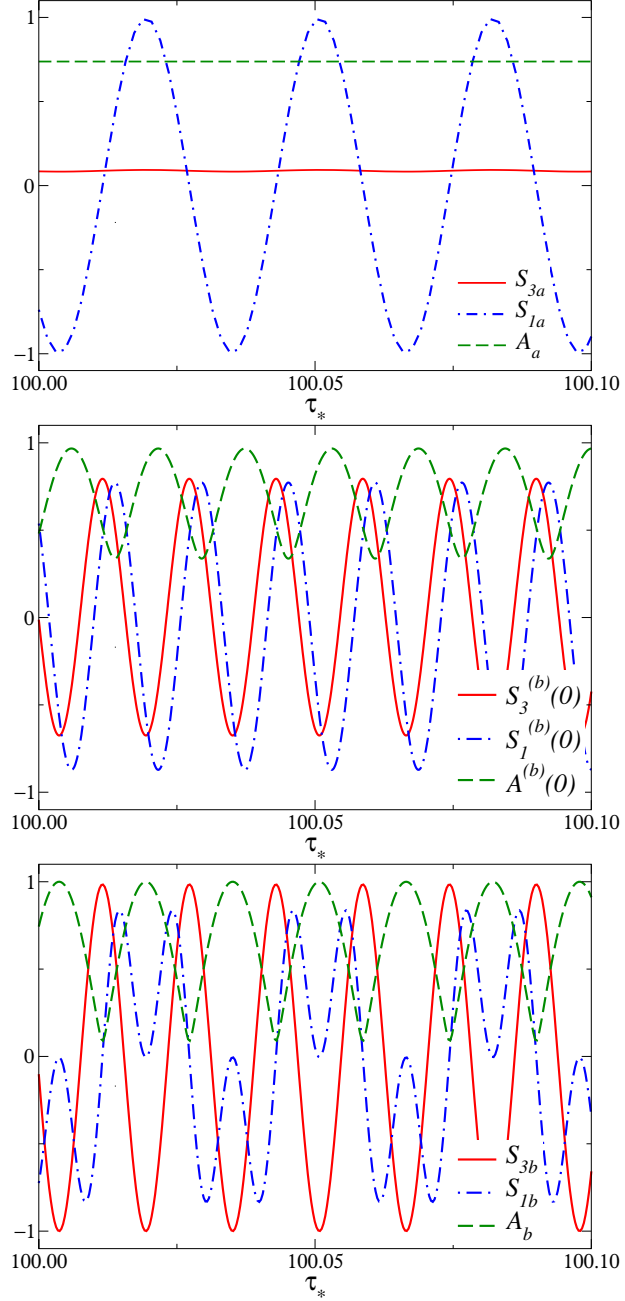


Figure A.2: Dependence on $\tau_* \equiv t_*/\sqrt{t_s}$ of the magnetizations $S_{1/3}$ and the adiabaticity function A at the end of the first dynamic branch where $\beta(t)$ is linearly increasing, and then back along the return way, when $\tau = 0$ (intermediate) and at the end of the round-trip protocol (bottom), for $v = 1$, and $\tau_* \approx 100$. These results show clearly how the oscillations of $S_{1,a}$, and therefore of the relative phase of the two functions $\phi_i(t)$ in Eq. (A.2), at the end of the first branch are closely related to the oscillations of all observables along the return way of the round-trip protocol.

We now analyze the dynamics of the round-trip protocol in the large- τ_* limit,

showing that such limit is problematic for this problem. We consider the values of the above observables at the end of the first and second part of the protocol:

$$\begin{aligned} S_{3/1a}(v, \tau_*) &= S_{3/1}^{(a)}(v, \tau_*, \tau_*) , \\ S_{3/1b}(v, \tau^*) &= S_{3/1}^{(b)}(v, -\tau_*, \tau_*) , \\ A_a(v, \tau_*) &= A^{(a)}(v, \tau_*, \tau_*) , \\ A_b(v, \tau_*) &= A^{(b)}(v, -\tau_*, \tau_*) . \end{aligned} \quad (\text{A.17})$$

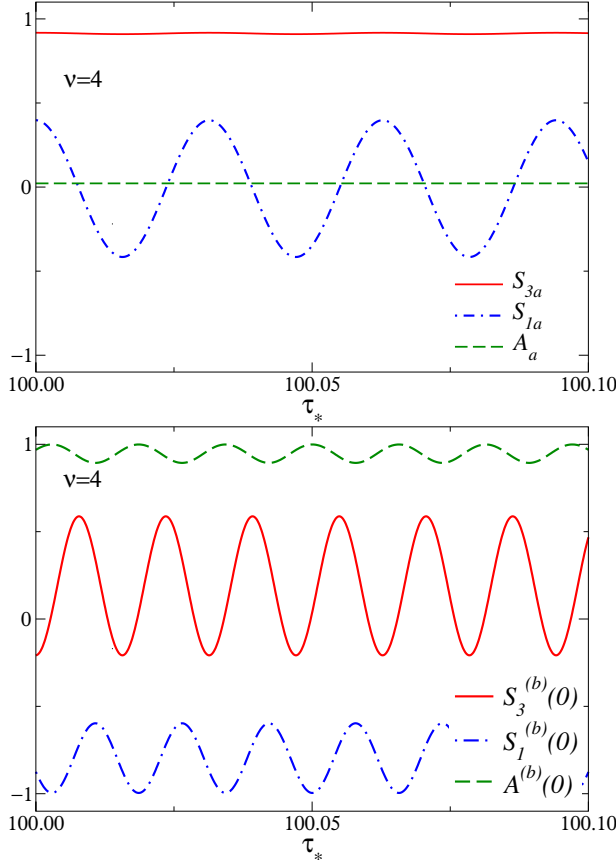


Figure A.3: Dependence on $\tau_* \equiv t_*/\sqrt{t_s}$ of the magnetizations $S_{1/3}$ and the adiabaticity function A at the end of the first dynamic branch where $\beta(t)$ is linearly increasing, and then back along the return way, when $\tau = 0$ (bottom), for $v = 4$, and $\tau_* \approx 100$.

Some notable limits can be derived for the first branch of the protocol using the asymptotic behaviors of the parabolic cylinder functions $D_\nu(x)$ [79, 147], corresponding to the standard LZ problem, see e.g. Refs. [79, 101], such as

$$\begin{aligned} S_{3a}(v, \tau_* \rightarrow \infty) &= 1 - 2 e^{-\pi v/4} , \\ A_a(v, \tau_* \rightarrow \infty) &= \sqrt{1 - e^{-\pi v/4}} . \end{aligned} \quad (\text{A.18})$$

Both S_{3a} and A_a approach their asymptotic behaviors with oscillating corrections suppressed as $O(\tau_*^{-1})$. For example, in the case of the adiabaticity function we find

$$\begin{aligned} \Delta A_a &\equiv A_a(v, \tau_*) - A_a(v, \infty) \\ &\approx \frac{f(u)}{\tau_*} \cos[\tau_*^2 - \frac{u}{4} \ln \tau_* + g(u)] , \end{aligned} \quad (\text{A.19})$$

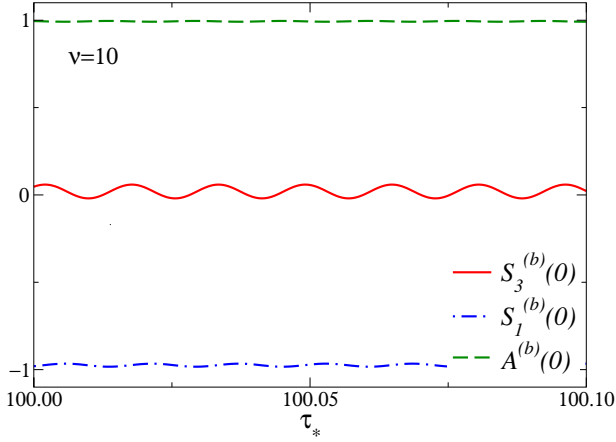


Figure A.4: Dependence on $\tau_* \equiv t_*/\sqrt{t_s}$ of the magnetizations $S_{1/3}$ and the adiabaticity function A along the return way at $\tau = 0$, for $v = 10$, and $\tau_* \approx 100$.

where $f(u)$ and $g(u)$ are time-independent functions of u . Unlike S_{3a} and A_a , the quantity S_{1a} does not show a regular large- τ_* limit, but rapid oscillations with diverging frequency in the large- τ^* limit. Indeed, using again the asymptotic behaviors of the parabolic cylinder functions $D_\nu(x)$ [79, 147], the asymptotic large- τ_* behavior of $S_{1,a}$ turns out to be

$$\begin{aligned} S_{1a} &\approx B(v) \cos \varphi(v, \tau_*) , \\ B(v) &= 2 e^{-\pi v/8} \sqrt{1 - e^{-\pi v/4}} \leq 1 , \\ \varphi(v, \tau_*) &= \tau_*^2 + \frac{v}{8} \ln(2\tau_*^2) - \text{Arg} \left[\Gamma \left(i \frac{v}{8} \right) \right] + \frac{3\pi}{4} . \end{aligned} \quad (\text{A.20})$$

In particular, $B(1) = 0.99611\dots$ and

$$\varphi(1, \tau_*) = \tau_*^2 + \frac{1}{4} \ln \tau_* + 4.08501\dots \quad (\text{A.21})$$

Unlike S_{3a} and A_a that converge to a large- τ_* limit, the leading behavior of S_{1a} is characterized by rapid oscillations. Its oscillatory behavior is essentially related to the relative phase $e^{-i\varphi(u,\tau)}$ of the functions $\phi_1(u, \tau)$ and $\phi_2(u, \tau)$, cf. Eq. (A.2). Note that oscillations become faster and faster in the large- τ^* limit, with a time-dependent frequency $\omega(\tau_*)$ diverging as $\omega(\tau_*) \approx \tau_*$. Therefore, unlike S_{3a} and A_a whose oscillations gets suppressed as $1/\tau_*$ approximately, the quantity S_{1a} does not possess a well defined large- τ_* limit, reflecting the fact that the relative phase of the ϕ_i does not converge in the large- τ_* limit.

This fact has dramatic implications for the behavior of the system along the backward branch, making all quantities rapidly oscillating at the return point, with a frequency related to that of the relative phase at the end of the first branch. This behavior is clearly shown in Figs. A.2, where we report some results for the quantities defined in Eqs. (A.17), at the end of the first branch and at the end of the round-trip protocol, and along the return way at $\tau = 0$, at fixed $v = 1$ and as a function of the parameter τ_* , for a relatively small interval around $\tau_* \approx 100$. As shown by the analogous curves reported in Figs. A.3 and A.4 for $\nu = 4$ and $\nu = 10$ respectively, the size of the oscillations depends on the value of ν , and, as expected, it tends to decreases in the adiabatic limit when increasing ν .

These results evidentiate the peculiar oscillations in the large- τ_* limit at finite values of ν , which make predictions on the return behavior practically impossible without an extreme precision on the control of the parameters of the protocols.

A.1 Equilibrium FSS functions

In this appendix, we derive the FSS functions (2.64) for the Ising model (2.58) at $h_\perp < 1$, in the limit $h_\parallel \rightarrow 0^\pm$, $L \rightarrow \infty$. As noticed in Refs. [83], the quantum FOT is controlled by the competition of the two lowest energy levels. Therefore, it is possible to write down an effective two-level Hamiltonian by restricting the many-body system to the Hilbert space spanned by the ground state $|\psi_0\rangle$ and the first excited state $|\psi_1\rangle$, obtaining

$$\hat{H}_{\text{eff}} = E_0 \hat{\text{Id}}_{2 \times 2} + \frac{1}{2} (\Delta(h_\perp, L) \hat{\sigma}^{(1)} - \mathcal{E}(h_\perp, h_\parallel, L) \hat{\sigma}^{(3)}), \quad (\text{A.22})$$

where E_0 is the ground state energy of the degenerate vacua at $h_\parallel = 0$, $L = \infty$. This Hamiltonian is readily diagonalized in the basis

$$|+\rangle = \sin\left(\frac{\alpha}{2}\right) |\psi_0\rangle + \cos\left(\frac{\alpha}{2}\right) |\psi_1\rangle \quad (\text{A.23})$$

$$|-\rangle = \cos\left(\frac{\alpha}{2}\right) |\psi_0\rangle - \sin\left(\frac{\alpha}{2}\right) |\psi_1\rangle \quad (\text{A.24})$$

with

$$\tan(\alpha) = \kappa^{-1} = \frac{\Delta(h_\perp, L)}{\mathcal{E}(h_\perp, h_\parallel, L)}, \quad 0 < \alpha \leq \frac{\pi}{2}. \quad (\text{A.25})$$

It follows that the energy eigenvalues are given by

$$E_\pm = E_0 \pm \frac{1}{2} \sqrt{\mathcal{E}^2 + \Delta^2} \quad (\text{A.26})$$

and, therefore, the energy gap (2.63) reads as

$$\Delta E(h_\perp, h_\parallel, L) = \Delta(h_\perp, L) \sqrt{1 + \kappa^2} \quad (\text{A.27})$$

from which one has $f_E(\kappa) = \sqrt{1 + \kappa^2}$ (cf Eq. (2.64)). The longitudinal magnetization is

$$\begin{aligned} M(h_\perp, h_\parallel, L) &= M_0(h_\perp) \langle -|\hat{\sigma}^{(3)}|-\rangle \\ &= M_0(h_\perp) \left(\cos^2\left(\frac{\alpha}{2}\right) - \sin^2\left(\frac{\alpha}{2}\right) \right), \end{aligned} \quad (\text{A.28})$$

from which one finds the FSS function (cf. Eq. (2.64))

$$f_M(\kappa) = \cos(\alpha) = \frac{\kappa}{\sqrt{1 + \kappa^2}}. \quad (\text{A.29})$$

A.2 FSS functions across a FOT

In this appendix, we focus on the solution of the finite-time LZS problem characterizing the linear driving of the Ising model (2.58) across a quantum FOT, see Sec. 2.8.3. For a better exposition, the case of single and of round-trip passages are treated in different subsections.

A.2.1 Single passage

For a single passage through the quantum FOT starting at $\tau_i < 0$, the finite-time LZS problem has an analytical solution – first derived in Ref. [79]. The standard procedure is to decouple the set of equation (2.92) by taking a time derivative. In this way, the differential equation e.g. for $c_0(\tau, v)$ takes the form of a Weber differential equation

$$\frac{d^2}{d\tau^2}c_0(\tau, v) + (\tau^2 + \frac{v}{4} - i)c_0(\tau, v) = 0, \quad (\text{A.30})$$

which is solved in terms of Parabolic Cylinder functions. It follows that the 2×2 evolution matrix $U(\tau, \tau_i)$ in (2.92) has elements

$$U_{00} = \frac{\Gamma(1 - \frac{iv}{8})}{\sqrt{2\pi}} \left[\mathcal{D}_{-1+\frac{iv}{8}}(\sqrt{2}e^{i\frac{3\pi}{4}}\tau_i)\mathcal{D}_{\frac{iv}{8}}(\sqrt{2}e^{-i\frac{\pi}{4}}\tau) + \mathcal{D}_{-1+\frac{iv}{8}}(\sqrt{2}e^{-i\frac{\pi}{4}}\tau_i)\mathcal{D}_{\frac{iv}{8}}(\sqrt{2}e^{i\frac{3\pi}{4}}\tau) \right]; \quad (\text{A.31a})$$

$$U_{01} = \frac{2\Gamma(1 - \frac{iv}{8})}{\sqrt{\pi v}} e^{i\frac{\pi}{4}} \left[\mathcal{D}_{\frac{iv}{8}}(\sqrt{2}e^{-i\frac{\pi}{4}}\tau_i)\mathcal{D}_{\frac{iv}{8}}(\sqrt{2}e^{i\frac{3\pi}{4}}\tau) - \mathcal{D}_{\frac{iv}{8}}(\sqrt{2}e^{i\frac{3\pi}{4}}\tau_i)\mathcal{D}_{\frac{iv}{8}}(\sqrt{2}e^{-i\frac{\pi}{4}}\tau) \right], \quad (\text{A.31b})$$

with $U_{10} = -U_{01}^*$ and $U_{11} = U_{00}^*$, $\Gamma(z)$ is the Euler Gamma function.

In the limit $|\tau_i| \gg 1$, these expressions can be simplified using known relations for $\mathcal{D}_\nu(z)$, reading as

$$U_{00}(|\tau_i| \gg 1) \simeq e^{i\Phi(\tau_i, v)} e^{-\frac{\pi v}{32}} \mathcal{D}_{\frac{iv}{8}}(\sqrt{2}e^{i\frac{3\pi}{4}}\tau); \quad (\text{A.32a})$$

$$U_{10}(|\tau_i| \gg 1) \simeq e^{i\Phi(\tau_i, v)} \sqrt{\frac{v}{8}} e^{-i\frac{\pi}{4}} e^{-\frac{\pi v}{32}} \mathcal{D}_{-1+\frac{iv}{8}}(\sqrt{2}e^{i\frac{3\pi}{4}}\tau), \quad (\text{A.32b})$$

and the dependence on the initial condition τ_i drops out everywhere but in the phase

$$\Phi(q, v) = -q^2 - \frac{v}{4} \log(\sqrt{2}|q|). \quad (\text{A.33})$$

One can then easily obtain the expressions in Eqs. (2.93)-(2.94) for the FSS functions. The latter do not show any dependence on the initial condition τ_i . It is interesting to note that by taking the limit $\tau \rightarrow \infty$ in Eq. (2.93), one obtains the Landau-Zener prediction for the defects abundance

$$\mathcal{F}_M(\tau \rightarrow \infty, v) = 1 - 2e^{-\frac{\pi v}{4}}, \quad (\text{A.34})$$

in agreement with standard Kibble-Zurek arguments [24].

A.2.2 Round trip

With a similar strategy, it is possible to extend the solution of Appendix A.2.1 to the round-trip protocol, by solving the two-level problem in the interval $t \in [t_f, 2t_f + |t_i|]$. Denoting with

$$x = \frac{t_f + |t_i| - t}{\sqrt{u}}, \quad (\text{A.35})$$

one finds the following elements of the 2×2 evolution matrix $\tilde{U}(\tau, \tau_f)$ in (2.95):

$$\tilde{U}_{00} = \frac{\Gamma(1 - \frac{i\nu}{8})}{\sqrt{2\pi}} \left[\mathcal{D}_{\frac{i\nu}{8}}(\sqrt{2}e^{i\frac{3\pi}{4}}|\tau_i|) \mathcal{D}_{-1+\frac{i\nu}{8}}(\sqrt{2}e^{-i\frac{\pi}{4}}x) + \mathcal{D}_{\frac{i\nu}{8}}(\sqrt{2}e^{-i\frac{\pi}{4}}|\tau_i|) \mathcal{D}_{-1+\frac{i\nu}{8}}(\sqrt{2}e^{i\frac{3\pi}{4}}x) \right]; \quad (\text{A.36a})$$

$$\tilde{U}_{10} = \frac{2\Gamma(1 - \frac{i\nu}{8})}{\sqrt{\pi\nu}} e^{i\frac{\pi}{4}} \left[\mathcal{D}_{\frac{i\nu}{8}}(\sqrt{2}e^{i\frac{3\pi}{4}}|\tau_i|) \mathcal{D}_{\frac{i\nu}{8}}(\sqrt{2}e^{-i\frac{\pi}{4}}x) - \mathcal{D}_{\frac{i\nu}{8}}(\sqrt{2}e^{-i\frac{\pi}{4}}|\tau_i|) \mathcal{D}_{\frac{i\nu}{8}}(\sqrt{2}e^{i\frac{3\pi}{4}}x) \right], \quad (\text{A.36b})$$

with $\tilde{U}_{01} = -\tilde{U}_{10}^*$ and $\tilde{U}_{11} = \tilde{U}_{00}^*$.

Similarly to the previous case, these expressions simplify in the limit $|\tau_i| \gg 1$:

$$\tilde{U}_{11}(|\tau_i| \gg 1) \simeq e^{i\Phi(\tau_i, \nu)} e^{-\frac{\pi\nu}{32}} \mathcal{D}_{\frac{i\nu}{8}}(\sqrt{2}e^{-i\frac{\pi}{4}}x); \quad (\text{A.37a})$$

$$\tilde{U}_{01}(|\tau_i| \gg 1) \simeq e^{i\Phi(\tau_i, \nu)} \sqrt{\frac{\nu}{8}} e^{-i\frac{\pi}{4}} e^{-\frac{\pi\nu}{32}} \mathcal{D}_{-1+\frac{i\nu}{8}}(\sqrt{2}e^{-i\frac{\pi}{4}}x). \quad (\text{A.37b})$$

From these equations (together with (A.32)), one finds

$$c_0 = e^{-\frac{\pi\nu}{16}} \left\{ \mathcal{D}_{\frac{i\nu}{8}}(\sqrt{2}e^{i\frac{3\pi}{4}}\tau_f) [\mathcal{D}_{\frac{i\nu}{8}}(\sqrt{2}e^{-i\frac{\pi}{4}}x)]^* - \frac{i\nu}{8} e^{2i\Phi(\tau_i, \nu)} \mathcal{D}_{-1+\frac{i\nu}{8}}(\sqrt{2}e^{i\frac{3\pi}{4}}\tau_f) \mathcal{D}_{-1+\frac{i\nu}{8}}(\sqrt{2}e^{-i\frac{\pi}{4}}x) \right\}; \quad (\text{A.38a})$$

$$c_1 = e^{-\frac{\pi\nu}{16}} \sqrt{\frac{\nu}{8}} e^{i\frac{\pi}{4}} \left\{ - \mathcal{D}_{\frac{i\nu}{8}}(\sqrt{2}e^{i\frac{3\pi}{4}}\tau_f) [\mathcal{D}_{-1+\frac{i\nu}{8}}(\sqrt{2}e^{-i\frac{\pi}{4}}x)]^* - i e^{2i\Phi(\tau_i, \nu)} \mathcal{D}_{-1+\frac{i\nu}{8}}(\sqrt{2}e^{i\frac{3\pi}{4}}\tau_f) \mathcal{D}_{\frac{i\nu}{8}}(\sqrt{2}e^{-i\frac{\pi}{4}}x) \right\}, \quad (\text{A.38b})$$

and determines the FSS functions as detailed in the main text.

Notice that the coefficients (A.38a)-(A.38b) (hence the FSS functions) keep a non-trivial dependence on the initial condition τ_i during the non-equilibrium dynamics via the phase (A.33). This is not surprising given that $x_i \equiv |\tau_i|$ is the time at which the ramp is inverted after the first passage across the quantum FOT. At this time, the system is far from equilibrium and hence unable to wash out the memory on its initial (non-equilibrium) condition before being driven across the quantum FOT for the second time.

Appendix B

Liouvillian gap

B.1 Steady-state solution and Δ_λ for $b = 1$.

In this appendix, we discuss the spectrum of the Liouville superoperator $\mathcal{L}[\rho]$ appearing in Eq. (1.4) for the case $b = 1$. In particular, we focus on the Liouvillian gap Δ_λ and the steady-state solution. The study is dramatically simplified after we move to the momentum basis. To this end, let us first review the unitary Kitaev ring in momentum space in the absence of dissipation.

We define the Fourier transform of the operator \hat{c}_x as [107]

$$\hat{c}_x = \frac{e^{-i\pi/4}}{\sqrt{L}} \sum_k e^{ikx} \hat{c}_k, \quad k = \left\{ \pm \frac{(2n-1)\pi}{L} \right\}, \quad (\text{B.1})$$

where the momenta are induced by the boundary conditions used and $n = 1, \dots, L/2$. To simplify the discussion, we only consider even lattice sizes, so that $L/2$ is always an integer number. For each mode $k > 0$, we can choose an ordered Hilbert-space basis of the form $\{|0_k\rangle, |1_k\rangle, |1_{-k}\rangle, |1_{k,-k}\rangle\}$, where the hamiltonian is $\hat{H} = \sum_{k>0} \hat{H}_k$ with

$$\hat{H}_k = \begin{pmatrix} 0 & 0 & 0 & 2|\sin k| \\ 0 & -2f_k(\mu) & 0 & 0 \\ 0 & 0 & -2f_k(\mu) & 0 \\ 2|\sin k| & 0 & 0 & -4f_k(\mu) \end{pmatrix}, \quad (\text{B.2})$$

and $f_k = \mu/2 + \cos k$ [107, 131]. The full Hilbert space \mathcal{H} decomposes naturally into the direct product of n distinct 4-dimensional subspaces. We take advantage of this transformation, which allows us to trade the exponential complexity of the starting problem with a polynomial one.

The same change of basis simplifies the study even in the presence of dissipation. If we consider the eigenvalue problem related to Eq. (1.4) in momentum space, we get

$$\mathcal{L}[\rho] = \sum_{k>0} \mathcal{L}_k[\rho_k], \quad \mathcal{L}_k[\rho_k] = \beta_k^{(j)} \rho_k^{(j)}, \quad (\text{B.3})$$

where $\rho = \bigotimes_{k>0} \rho_k$ and the superoperator \mathcal{L}_k reads as

$$\begin{aligned} \mathcal{L}_k[\rho_k] = & -i[H_k, \rho_k] + w\hat{c}_k \rho_k \hat{c}_k^\dagger - \frac{w}{2} \{c_k^\dagger \hat{c}_k, \rho_k\} \\ & + w\hat{c}_{-k} \rho_k \hat{c}_{-k}^\dagger - \frac{w}{2} \{c_{-k}^\dagger \hat{c}_{-k}, \rho_k\}. \end{aligned} \quad (\text{B.4})$$

In eq. (B.3), the complex number $\beta_k^{(j)} \in \mathbb{C}$ denotes the j -th eigenvalue associated with the k -th Hilbert space, so that λ_r are the eigenvalues of \mathcal{L} that are fully specified by $\lambda_r = \sum_k \beta_k^{(a_k)}$ with $a_k = 1, \dots, 16$. Within each momentum sector, the 16 eigenvalues $\beta_k^{(j)}$ are explicitly given by

$$\beta_k^{(j)} = \begin{cases} 0 & \\ -w & \text{deg. 4} \\ -w/2 \pm \sqrt{-4 - \mu^2 - 4\mu \cos k} & \text{deg. 2} \\ -w \pm 2\sqrt{-4 - \mu^2 - 4\mu \cos k} & \\ -3w/2 \pm \sqrt{-4 - \mu^2 - 4\mu \cos k} & \text{deg. 2} \\ -2w, & \end{cases} \quad (\text{B.5})$$

where on the right side we indicate the degeneracy of each eigenvalue. It is now simple to show that the Liouville gap is always equal to

$$\Delta_\lambda = \frac{w}{2}, \quad (\text{B.6})$$

independently of the chemical potential μ considered. The NESS is the only matrix $\rho_k^{(0)}$ surviving at asymptotically large times; it satisfies $\mathcal{L}_k[\rho_k^{(0)}] = 0$ for all $k > 0$. We remark that the existence and uniqueness of a steady-state solution, in general terms, cannot be taken for granted [29]. Nonetheless, we were able to find a closed-form expression for this state within each Hilbert domain \mathcal{H}_k

$$\rho_k^{(0)} = \begin{pmatrix} 1 - \frac{3(1-\cos(2k))}{2g_k(\mu,w)} & 0 & 0 & \frac{|\sin k|(2\mu+iw+4\cos k)}{2g_k(\mu,w)} \\ 0 & \frac{\sin^2 k}{g_k(\mu,w)} & 0 & 0 \\ 0 & 0 & \frac{\sin^2 k}{g_k(\mu,w)} & 0 \\ \frac{|\sin k|(2\mu-iw+4\cos k)}{2g_k(\mu,w)} & 0 & 0 & \frac{\sin^2 k}{g_k(\mu,w)} \end{pmatrix} \quad (\text{B.7})$$

where $g_k(\mu, w) = 4 + \mu^2 + w^2/4 + 4\mu \cos k$. Even if the system is coupled with particle-decay operators that continuously remove particles from the ring, the NESS can exhibit a non-vanishing density of fermions—the total number of particles is not preserved by \hat{H} . For instance, the average number of particles per site in the asymptotic limit $t \rightarrow +\infty$ is

$$\frac{1}{L} \sum_x \langle \hat{n}_x \rangle = \frac{4}{L} \sum_{n=1}^{L/2} \frac{\sin^2 \left[\frac{(2n-1)\pi}{L} \right]}{4 + \mu^2 + \frac{w^2}{4} + 4\mu \cos \left[\frac{(2n-1)\pi}{L} \right]}. \quad (\text{B.8})$$

We verified numerically the above equation.

B.2 Simulation techniques

In this Appendix, we summarize the numerical techniques employed for the real-time evolution of the Kitaev ring in Eq. (1.5) and the determination of the gap Δ_λ [131]. We also review the Kitaev model investigated in this thesis in momentum space for $b \geq 1$.

B.2.1 Time evolution of two-point functions (coordinate space)

The algorithmic details related to the real-time evolution of correlation functions are thoroughly explained in Refs. [107, 36]. We generalize these techniques to the dissipation mechanism described by Eq. (1.4). We adopt these numerical techniques every time the number of local dissipators n is fixed. Essentially, we find a closed system of coupled differential equations allowing us to describe the time evolution of the two-point functions $C(x, y, t) = C_{x,y}$ and $P(x, y, t) = P_{x,y}$ defined in Eq. (3.36). Differentiating these observables with respect to time, we obtain the following differential equations

$$\begin{aligned} \frac{d}{dt} C_{x,y} &= i(C_{x,y+1} - C_{x-1,y} + C_{x,y-1} - C_{x+1,y}) \\ &\quad - i(P_{y,x-1}^\dagger - P_{y,x+1}^\dagger - P_{x,y-1} + P_{x,y+1}) \\ &\quad - \frac{w}{2} \sum_{\substack{j=1 \\ (\text{mod } b)}}^n (\delta_{j,y} C_{x,j} + \delta_{j,x} C_{j,y} + \delta_{j,y} C_{x,j} + \delta_{1,j} C_{j,y}) \\ &\quad , \\ \frac{d}{dt} P_{x,y} &= -i(P_{x,y+1} + P_{x+1,y} + P_{x,y-1} + P_{x-1,y}) \\ &\quad - i(C_{x,y-1} - C_{y,x-1} - C_{x,y+1} + C_{y,x+1}) \\ &\quad - i(\delta_{x-1,y} - \delta_{x+1,y}) - 2i\mu P_{x,y} \\ &\quad - \frac{w}{2} \sum_{\substack{j=1 \\ (\text{mod } b)}}^n (\delta_{j,y} P_{x,j} + \delta_{j,x} P_{j,y} + \delta_{j,y} P_{x,j} + \delta_{j,x} P_{j,y}) . \end{aligned} \quad (\text{B.9})$$

We then use standard 4th-order Runge-Kutta techniques to solve this system, using the initial conditions given by

$$C_{x,y}(0) = \text{Tr}[\rho(0)(\hat{c}_x^\dagger \hat{c}_y + \hat{c}_y^\dagger \hat{c}_x)] \quad (\text{B.10})$$

$$P_{x,y}(0) = \text{Tr}[\rho(0)(\hat{c}_x^\dagger \hat{c}_y^\dagger + \hat{c}_y \hat{c}_x)] . \quad (\text{B.11})$$

B.2.2 Time evolution for $b \geq 1$ (momentum space)

Following the quench protocol outlined in Sec. 3.4.2, we first set the starting density matrix $\rho(0)$ to the ground state of \hat{H} from Eq. (B.2). In particular, the mixture $\rho(0)$ can be rewritten in terms of the reduced density matrices defined within each k -sector $\rho_k(0) = |\Omega_k\rangle \langle \Omega_k|$ as

$$\rho(0) = \bigotimes_{k>0} \rho_k(0) . \quad (\text{B.12})$$

For $t > 0$, unfortunately, $\rho_k(t)$ does not remain inside the same k -sector as $\rho_k(0)$ (unless $b = 1$), and we are forced to study the time evolution of $\rho_k(t)$ in larger domains. For this reason, we define $n/2$ orthogonal Hilbert subspaces \mathcal{H}_{k_a} , whose dimension is 4^b , generated by

$$\mathcal{H}_{k_a} = \text{span} \bigotimes_{m=1}^b \{|0_{k_a^m}\rangle, |1_{k_a^m}\rangle, |1_{-k_a^m}\rangle, |1_{k_a^m, -k_a^m}\rangle\} , \quad (\text{B.13})$$

where $k_a^m \equiv k_a + 2\pi m/b$ and $k_a = \pi(2a - 1)/L$ with $a = 1, \dots, n/2$. We then express $\rho(t)$ as $\rho = \bigotimes_{a=1}^{n/2} \rho_{k_a}$, where ρ_{k_a} is a reduced density matrix living entirely in \mathcal{H}_{k_a} . The time evolution of each ρ_{k_a} is controlled by a self-contained Lindblad equation

$$\frac{d\rho_{k_a}}{dt} = -i[\hat{H}_{k_a}, \rho_{k_a}] + w\mathbb{D}[\rho_{k_a}], \quad (\text{B.14})$$

where $\hat{H}_{k_a} = \sum_{m=1}^b \hat{H}_{k_a^m}$. Straightforward manipulations allow us to write the dissipator $\mathbb{D}[\rho_{k_a}]$ in the following form

$$\begin{aligned} \mathbb{D}[\rho_{k_a}] &= \frac{1}{b} \sum_{m,p=1}^b \left(\hat{c}_{k_a^m} \rho_{k_a} \hat{c}_{k_a^p}^\dagger - \frac{1}{2} \{ \hat{c}_{k_a^m}^\dagger \hat{c}_{k_a^p}, \rho_{k_a} \} \right. \\ &\quad \left. + \hat{c}_{-k_a^m} \rho_{k_a} \hat{c}_{-k_a^p}^\dagger - \frac{1}{2} \{ \hat{c}_{-k_a^m}^\dagger \hat{c}_{-k_a^p}, \rho_{k_a} \} \right); \end{aligned} \quad (\text{B.15})$$

note that a prefactor $1/b$ naturally emerges in this context. Now, the two-point function expectation values, such as $C(x, y, t)$ or $P(x, y, t)$ in Eq. (3.36), can be evaluated directly. For instance, $C(x, y, t)$ takes the form

$$C(x, y, t) = \frac{2}{L} \Re \sum_{m,a,q} e^{\mp ik_a^m x} e^{iqy} \langle \hat{c}_{\pm k_a^m}^\dagger \hat{c}_q \rangle. \quad (\text{B.16})$$

The above equation can be further simplified since $\langle \hat{c}_{\pm k_a^m}^\dagger \hat{c}_q \rangle$, where $\langle \hat{c}_k^\dagger \hat{c}_q \rangle \equiv \text{Tr}[\rho(t) \hat{c}_k^\dagger \hat{c}_q]$, is non vanishing if and only if $q_a = \pm k_a^p$ for $p = 1, \dots, b$. Thus we obtain

$$\begin{aligned} C(x, y, t) &= \frac{2}{L} \sum_{a=1}^{n/2} \Re \left\{ \sum_{m,p=1}^b e^{\mp ik_a^m x} e^{ik_a^p y} \langle \hat{c}_{\pm k_a^m}^\dagger \hat{c}_{k_a^p} \rangle \right. \\ &\quad \left. + \sum_{m,p=1}^b e^{\mp ik_a^m x} e^{-ik_a^p y} \langle \hat{c}_{\pm k_a^m}^\dagger \hat{c}_{-k_a^p} \rangle \right\}. \end{aligned} \quad (\text{B.17})$$

Analogous equations can be obtained for different two-point functions as well with similar manipulations. We finally provide an explicit expression for the entanglement entropy $S(t)$ that can be easily expressed within each sector \mathcal{H}_{k_a} as

$$S = - \sum_{a=1}^{n/2} \sum_{m=1}^{4^b} \lambda_{a,m} \log \lambda_{a,m}, \quad (\text{B.18})$$

where $\lambda_{a,m}$ is the m -th eigenvalue of the reduced density matrix ρ_{k_a} .

B.2.3 Third quantization techniques: coordinate basis

We use third-quantization techniques presented in Ref. [131] to compute the Liouvillian gap of the Kitaev rings considered in this work. The results shown in this thesis have been obtained from the diagonalization of $4L \times 4L$ antisymmetric complex matrix A defined as

$$\begin{aligned} A_{2j-1,2k-1} &= -2iH_{jk} - D_{jk}/2 + D_{kj}/2 \\ A_{2j-1,2k} &= iD_{kj} \\ A_{2j,2k-1} &= -iD_{jk} \\ A_{2j,2k} &= -2iH_{jk} + D_{jk}/2 - D_{kj}/2. \end{aligned} \quad (\text{B.19})$$

The $2L \times 2L$ matrices H_{jk} and D_{jk} are determined, respectively, by the hamiltonian and dissipation processes written in terms of Majorana fermion operators $\{\hat{v}_j\}$, which are defined as

$$\hat{v}_{2j-2} = (\hat{c}_j + \hat{c}_j^\dagger), \quad \hat{v}_{2j-1} = i(\hat{c}_j - \hat{c}_j^\dagger). \quad (\text{B.20})$$

The Hamiltonian matrix H_{jk} reads as follows (here the indices range from 0 up to $2L - 1$)

$$\begin{aligned} \hat{H} = \sum_{jk} \hat{v}_j H_{jk} \hat{v}_k &= \frac{1}{4} \sum_{j=0}^{L-1} \left(-2i\hat{v}_{2j+1}\hat{v}_{2j+2} \right. \\ &\quad \left. + i\mu\hat{v}_{2j}\hat{v}_{2j+1} + h.c. \right), \end{aligned} \quad (\text{B.21})$$

where due to APBC we have $\hat{v}_{x+2L} = -\hat{v}_{2x}$. The matrix elements of D_{jk} are instead given by

$$\begin{aligned} D_{jk} &= \frac{w}{4} \sum_{k=0}^{n-1} \left(\delta_{2bk,2bk} + i\delta_{2bk,2bk+1} \right. \\ &\quad \left. - i\delta_{2bk+1,2bk} + \delta_{2bk+1,2bk+1} \right) \end{aligned} \quad (\text{B.22})$$

If β_j are the eigenvalues of the matrix A , known as the *rapitidies* [131], all eigenvalues come in pairs $\beta_j, -\beta_j$ due to the algebraic properties of complex antisymmetric matrices. The Liouvillian gap is finally given by

$$\Delta_\lambda = 2 \min_j [|\Re \beta_j|] \quad (\text{B.23})$$

B.2.4 Third quantization techniques: momentum basis

We use third-quantization techniques also in momentum space to facilitate the evaluation of the Liouvillian gap Δ_λ . This strategy is surely convenient for moderate values of b , since one trades the diagonalization of a unique $4L \times 4L$ matrix with the diagonalization of $n/2$ matrices A^a of dimension $8b \times 8b$.

We thus define the antisymmetric matrix A^a corresponding to the momentum $k_a = \pi(2a - 1)/L$ with $a = 1, \dots, n/2$ as

$$\begin{aligned} A_{2j,2k}^a &= -2iH_{jk}^a + D_{kj}^a/2 - D_{jk}^a/2 \\ A_{2j,2k+1}^a &= iD_{jk}^a \\ A_{2j+1,2k}^a &= -iD_{kj}^a \\ A_{2j+1,2k+1}^a &= -2iH_{jk}^a + D_{kj}^a/2 - D_{jk}^a/2 \quad , \end{aligned} \quad (\text{B.24})$$

where H_{jk}^a and D_{jk}^a are $4^b \times 4^b$ matrices that correspond, respectively, to the hamiltonian and dissipation operators acting on the Hilbert space \mathcal{H}_{k_a} . After introducing Majorana fermions, one obtains for H_{jk}^a

$$\begin{aligned} H^a &= \frac{1}{4} \sum_{p=0}^{2b-1} \left(i\delta_{2p,2p+1} + 2i \cos k_a^p \delta_{2p,2p+1} + h.c. \right) \\ &\quad + \frac{1}{2} \sum_{p=0}^{b-1} |\sin k_a^p| \left(i\delta_{2p,2b+2p+1} + i\delta_{2p+1,2b+2p} + h.c. \right), \end{aligned} \quad (\text{B.25})$$

where we recall that $k_a^p = \pi(2a - 1)/L + 2\pi p/b$. The matrix elements of the dissipation matrix D_{jk}^a are instead given by

$$D^a = \frac{1}{4} \sum_{p=0}^{b-1} \sum_{q=0}^{b-1} (\delta_{2\omega_a(p), 2\omega_a(q)} + \delta_{2\omega_a(p), 2\omega_a(q)+1} \\ - \delta_{2\omega_a(p)+1, 2\omega_a(q)} + \delta_{2\omega_a(p)+1, 2\omega_a(q)+1}), \quad (\text{B.26})$$

where $\omega_a(p)$ is a shorthand notation standing for

$$\omega_a(p) = \begin{cases} b + p & \text{if } k_a^p \geq \pi \\ p & \text{if } k_a^p < \pi. \end{cases} \quad (\text{B.27})$$

Again, if β_j^a are the eigenvalues of the matrices A^a , the Liouvillian gap is then given by

$$\Delta_\lambda = 2 \min_{a,j} [|\Re \beta_j^a|], \quad (\text{B.28})$$

since all rapidities β_j always come in pairs $\beta_j, -\beta_j$.

Appendix C

Correlators in the thermal bath framework

In this appendix we provide some details of the computations for the fermionic Kitaev wire in the presence of a thermal bath.

C.1 Asymptotic thermal states

The dynamics of the system in contact with the thermal bath described by the Lindblad master equation (1.4) with the dissipator term (3.49) leads to thermal states, such as those described by the density matrix reported in Eq. (3.52). To compute the correlation functions of the fermionic operators \hat{c}_x in thermal states of the Hamiltonian $\hat{H}(w)$, one can use the relation with the Bogoliubov eigenoperators \hat{b}_k , cf. Eq. (3.48), and the thermal correlations of the Bogoliubov operators b_k , i.e.

$$\langle b_k^\dagger b_q \rangle \equiv \text{Tr}[\rho_t(w, T) b_k^\dagger b_q] = \frac{\delta_{kq}}{1 + e^{\omega_k/T}}, \quad (\text{C.1})$$

corresponding to the standard Fermi-Dirac distribution function. Note also that the other correlations $\langle b_k b_q \rangle$ and $\langle b_k^\dagger b_q^\dagger \rangle$ vanish. Then the correlation functions of the original fermionic field \hat{c}_x can be straightforwardly obtained from Eq. (3.48).

C.2 Computations for the unitary protocol

In the unitary QQ protocol, one starts from a Gibbs state associated with the Hamiltonian parameter w_i and the temperature T , then at $t = 0$ one instantaneously changes $w_i \rightarrow w$ and removes the contact with the thermal bath. Therefore the quantum evolution is unitary, described by the Schrödinger equation (1.2). One may easily obtain closed equations for the evolution of the correlation functions C and P defined in Eqs. (3.55) and (3.56).

We introduce the correlations

$$\mathcal{C}_{x,y} = \text{Tr}[\rho(t) \hat{c}_x^\dagger \hat{c}_y], \quad \mathcal{P}_{x,y} = \text{Tr}[\rho(t) \hat{c}_x^\dagger \hat{c}_y^\dagger], \quad (\text{C.2})$$

whose quantum evolution can be written as

$$\begin{aligned} \frac{d\mathcal{C}_{x,y}}{dt} &= i [\mathcal{C}_{x,y+1} - \mathcal{C}_{x-1,y} + \mathcal{C}_{x,y-1} - \mathcal{C}_{x+1,y}] - \\ &\quad - i (\mathcal{P}_{y,x-1}^\dagger - \mathcal{P}_{y,x+1}^\dagger) + i (\mathcal{P}_{x,y-1} - \mathcal{P}_{x,y+1}), \end{aligned} \quad (\text{C.3})$$

$$\begin{aligned} \frac{d\mathcal{P}_{x,y}}{dt} &= -i [\mathcal{P}_{x,y+1} + \mathcal{P}_{x+1,y} + \mathcal{P}_{x,y-1} + \mathcal{P}_{x-1,y}] - \\ &\quad - 2i\mu\mathcal{P}_{x,y} - i(\delta_{x-1,y} - \delta_{x+1,y}) - \\ &\quad - i (\mathcal{C}_{x,y-1} - \mathcal{C}_{y,x-1} - \mathcal{C}_{x,y+1} + \mathcal{C}_{y,x+1}). \end{aligned} \quad (\text{C.4})$$

The initial conditions are easily obtained by the relations with the thermal correlations of the Bogoliubov operators associated with the initial Gibbs state. Then the fermionic correlation function are obtained by

$$C(x, y, t) = 2 \operatorname{Re} \mathcal{C}_{x,y}(t), \quad P(x, y, t) = 2 \operatorname{Re} \mathcal{P}_{x,y}(t). \quad (\text{C.5})$$

The above differential equations are solved using the four-order Runge-Kutta method. The particle density is obtained from the data of $\mathcal{C}_{x,x} = \operatorname{Tr} [\rho(t) \hat{c}_x^\dagger \hat{c}_x]$.

C.3 Computations for the dissipative protocol

For the dissipative QQ protocol, where the thermal bath is kept in contact with the system, the evolution is driven by the Lindblad master equation (1.4), which can be equivalently written in terms of the time dependence of Heisenberg operators $\hat{O}_H(t)$, i.e. [141, 112]:

$$\partial_t \hat{O}_H(t) = i [\hat{H}(w), \hat{O}_H(t)] + \gamma \hat{\mathbb{D}}_T[\hat{O}_H(t)], \quad (\text{C.6})$$

where

$$\begin{aligned} \hat{\mathbb{D}}_T[\hat{O}_H(t)] &= \sum_k f(\omega_k) \left[2\hat{b}_k^\dagger \hat{O}_H(t) \hat{b}_k - \left\{ \hat{O}_H(t), \hat{b}_k \hat{b}_k^\dagger \right\} \right] \\ &\quad + \sum_k (1 - f(\omega_k)) \left[2\hat{b}_k \hat{O}_H(t) \hat{b}_k^\dagger - \left\{ \hat{O}_H(t), \hat{b}_k^\dagger \hat{b}_k \right\} \right], \end{aligned} \quad (\text{C.7})$$

where \hat{b}_k are the Bogoliubov operators associated with the Hamiltonian $\hat{H}(w)$.

The initial state at $t = 0$ is the Gibbs state for the Hamiltonian parameter w_i . This state corresponds to the steady state solution of the Eq. (C.6) with $\hat{H}(w_i)$. Then, the change of the Hamiltonian parameter to $w \neq w_i$ leads to a change of the Bogoliubov operators diagonalizing the Hamiltonian. We call $\{b'_k\}$ the operators which diagonalizes $\hat{H}(w)$,

$$\hat{H}(w) = \sum_{k=1}^L \omega'_k \hat{b}'_k^\dagger \hat{b}'_k, \quad (\text{C.8})$$

where $\{\omega'_k\}$ is the Bogoliubov spectrum associated with $\hat{H}(w)$. To evaluate the correlations of the Bogoliubov operators $\{b'_k\}$, one can solve the Eq. (C.6) for

couples of operators $\{b'_k\}$, obtaining [112]

$$\begin{aligned}\langle b'^{\dagger}_k b'_k \rangle &= (1 - e^{-2\gamma t}) f(\omega'_k) + e^{-2\gamma t} \langle b'^{\dagger}_k b'_k \rangle_0, \\ \langle b'^{\dagger}_k b'_q \rangle &= e^{i(\omega'_k - \omega'_q)t - 2\gamma t} \langle b'^{\dagger}_k b'_q \rangle_0, \\ \langle b'^{\dagger}_k b'^{\dagger}_q \rangle &= e^{i(\omega'_k + \omega'_q)t - 2\gamma t} \langle b'^{\dagger}_k b'^{\dagger}_q \rangle_0, \\ \langle b'_k b'_q \rangle &= e^{-i(\omega'_k + \omega'_q)t - 2\gamma t} \langle b'_k b'_q \rangle_0.\end{aligned}\tag{C.9}$$

The initial values $\langle b'^{\dagger}_k b'_q \rangle_0$ of the correlations is computed on the initial Gibbs state associated with w_i , and it can be obtained using the relations between $\{b_k\}$ to $\{b'_k\}$. This relation can be formally derived as follows [112]. Introducing the fermionic Nambu field $\mathbb{C}^{\dagger} = (\hat{c}_1^{\dagger}, \dots, \hat{c}_L^{\dagger}, \hat{c}_1, \dots, \hat{c}_L)$, their relations with the Bogoliubov operators $\mathbb{B}(w)^{\dagger} = (\hat{b}_1^{\dagger}, \dots, \hat{b}_L^{\dagger}, \hat{b}_1, \dots, \hat{b}_L)$ corresponding to the Hamiltonian $\hat{H}_K(w)$ are obtained by a unitary transformation, $\mathbb{C} = \mathbb{T}(w)\mathbb{B}(w)$. See e.g. Ref. [112] for more details. Therefore one can formally derive the relation between the Bogoliubov operators \hat{b}'_k and \hat{b}_k , corresponding to the Hamiltonian parameters w_i and w respectively, from the general relation

$$\mathbb{B}(w_2) = \mathbb{T}(w_2)^{\dagger} \mathbb{T}(w_1) \mathbb{B}(w_1).\tag{C.10}$$

Finally, to compute the time-dependent observables defined in Sec. 3.5.4, one can use the relations between the fermionic correlation functions associated with \hat{c}_x and those of the Bogoliubov operators \hat{b}_k , such as

$$\begin{aligned}C(x, y) &= \sum_{k,q=1}^L \left[A_{xk}^* A_{yq} \langle b'^{\dagger}_k b'_q \rangle + B_{xk}^* B_{yq} \langle b_k b'^{\dagger}_q \rangle \right. \\ &\quad \left. + A_{xk}^* B_{yq} \langle b'^{\dagger}_k b'^{\dagger}_q \rangle + B_{xk}^* A_{yq} \langle b_k b_q \rangle \right]\end{aligned}\tag{C.11}$$

where A and B are the matrices entering Eq. (3.48).

References

- [1] Anatoli Polkovnikov et al., “Colloquium: Nonequilibrium dynamics of closed interacting quantum systems”, *Rev. Mod. Phys.* **83**, 863–883 (2011).
- [2] I. M. Georgescu, S. Ashhab, and Franco Nori, “Quantum simulation”, *Rev. Mod. Phys.* **86**, 153–185 (2014).
- [3] Marton Kormos et al., “Real-time confinement following a quantum quench to a non-integrable model”, *Nature Physics* **13**, 246–249 (2017).
- [4] Alessio Lerose et al., “Quasilocalized dynamics from confinement of quantum excitations”, *Physical Review B* **102**, 041118 (2020).
- [5] Riccardo Javier Valencia Tortora, Pasquale Calabrese, and Mario Collura, “Relaxation of the order-parameter statistics and dynamical confinement”, *Europhysics Letters* **132**, 50001 (2020).
- [6] Gianluca Lagnese et al., “Quenches and confinement in a heisenberg–ising spin ladder”, *Journal of Physics A: Mathematical and Theoretical* **55**, 124003 (2022).
- [7] Stefano Scopa, Pasquale Calabrese, and Alvise Bastianello, “Entanglement dynamics in confining spin chains”, *Physical Review B* **105**, 125413 (2022).
- [8] Olalla A Castro-Alvaredo et al., “Entanglement oscillations near a quantum critical point”, *Physical Review Letters* **124**, 230601 (2020).
- [9] Joseph Vovrosh and Johannes Knolle, “Confinement and entanglement dynamics on a digital quantum computer”, *Scientific reports* **11**, 11577 (2021).
- [10] Marco Rigobello et al., “Entanglement generation in (1+ 1) D QED scattering processes”, *Physical Review D* **104**, 114501 (2021).
- [11] Stefan Birnhammer, Alvise Bastianello, and Michael Knap, “Prethermalization in one-dimensional quantum many-body systems with confinement”, *Nature Communications* **13**, 7663 (2022).
- [12] Andrew JA James, Robert M Konik, and Neil J Robinson, “Nonthermal states arising from confinement in one and two dimensions”, *Physical review letters* **122**, 130603 (2019).
- [13] Neil J Robinson, Andrew JA James, and Robert M Konik, “Signatures of rare states and thermalization in a theory with confinement”, *Physical Review B* **99**, 195108 (2019).
- [14] Titas Chanda et al., “Confinement and lack of thermalization after quenches in the bosonic Schwinger model”, *Physical Review Letters* **124**, 180602 (2020).

- [15] Leandro Aolita, Fernando de Melo, and Luiz Davidovich, “Open-system dynamics of entanglement:a key issues review”, *Reports on Progress in Physics* **78**, 042001 (2015).
- [16] Thomas WB Kibble, “Topology of cosmic domains and strings”, *Journal of Physics A: Mathematical and General* **9**, 1387 (1976).
- [17] Tom WB Kibble, “Some implications of a cosmological phase transition”, *Physics Reports* **67**, 183–199 (1980).
- [18] Wojciech H Zurek, “Cosmological experiments in superfluid helium?”, *Nature* **317**, 505–508 (1985).
- [19] Wojciech H Zurek, “Cosmological experiments in condensed matter systems”, *Physics Reports* **276**, 177–221 (1996).
- [20] Kurt Binder, “Theory of first-order phase transitions”, *Reports on progress in physics* **50**, 783 (1987).
- [21] Jin-Ming Cui et al., “Experimentally testing quantum critical dynamics beyond the Kibble–Zurek mechanism”, *Communications Physics* **3**, 44 (2020).
- [22] Alan J Bray, “Theory of phase-ordering kinetics”, *Advances in Physics* **51**, 481–587 (2002).
- [23] Chad N Weiler et al., “Spontaneous vortices in the formation of Bose–Einstein condensates”, *Nature* **455**, 948–951 (2008).
- [24] Jacek Dziarmaga, “Dynamics of a quantum phase transition and relaxation to a steady state”, *Advances in Physics* **59**, 1063–1189 (2010).
- [25] S Ulm et al., “Observation of the Kibble–Zurek scaling law for defect formation in ion crystals”, *Nature communications* **4**, 2290 (2013).
- [26] H. P. Breuer and F. Petruccione, “The theory of open quantum systems”, Oxford University Press, 2002.
- [27] Davide Rossini and Ettore Vicari, “Coherent and dissipative dynamics at quantum phase transitions”, *Physics Reports* **936**, 1–110 (2021).
- [28] L M Sieberer, M Buchhold, and S Diehl, “Keldysh field theory for driven open quantum systems”, *Reports on Progress in Physics* **79**, 096001 (2016).
- [29] Davide Nigro, “On the uniqueness of the steady-state solution of the LindbladGoriniKossakowskiSudarshan equation”, *Journal of Statistical Mechanics: Theory and Experiment* **2019**, 043202 (2019).
- [30] S. G. Schirmer and Xiaoting Wang, “Stabilizing open quantum systems by Markovian reservoir engineering”, *Phys. Rev. A* **81**, 062306 (2010).
- [31] Fernando Pastawski, Lucas Clemente, and Juan Ignacio Cirac, “Quantum memories based on engineered dissipation”, *Phys. Rev. A* **83**, 012304 (2011).
- [32] Marko Znidaric, “Relaxation times of dissipative many-body quantum systems”, *Phys. Rev. E* **92**, 042143 (2015).
- [33] Dong Yuan et al., “Solving the Liouvillian Gap with Artificial Neural Networks”, *Phys. Rev. Lett.* **126**, 160401 (2021).
- [34] Naoyuki Shibata and Hosho Katsura, “Dissipative spin chain as a non-Hermitian Kitaev ladder”, *Phys. Rev. B* **99**, 174303 (2019).

- [35] Naoyuki Shibata and Hosho Katsura, “Quantum Ising chain with boundary dephasing”, *PTEP* **2020**, 12 (2020).
- [36] Francesco Tarantelli and Ettore Vicari, “Quantum critical systems with dissipative boundaries”, *Phys. Rev. B* **104**, 075140 (2021).
- [37] Markonidari, “Transport in a one-dimensional isotropic Heisenberg model at high temperature”, *Journal of Statistical Mechanics: Theory and Experiment* **2011**, P12008 (2011).
- [38] Alessio Franchi, Davide Rossini, and Ettore Vicari, “Quantum many-body spin rings coupled to ancillary spins: The sunburst quantum Ising model”, *Phys. Rev. E* **105**, 054111 (2022).
- [39] Alessio Franchi, Davide Rossini, and Ettore Vicari, “Decoherence and energy flow in the sunburst quantum Ising model”, *Journal of Statistical Mechanics* **2022**, 083103 (2022).
- [40] Akash Mitra and Shashi C. L. Srivastava, “Quantum sunburst model under interaction quench: entanglement and role of initial state coherence”, arXiv:2212.12276 , (2022).
- [41] John Cardy, “Scaling and Renormalization in Statistical Physics”, Cambridge Lecture Notes in Physics, Cambridge University Press, 1996.
- [42] Subir Sachdev, “Quantum phase transitions”, 4, Cambridge University Press, 1999.
- [43] Andrea Pelissetto and Ettore Vicari, “Critical phenomena and renormalization-group theory”, ISSN: 0370-1573, *Physics Reports* **368**, 549–727 (2002).
- [44] Massimo Campostrini, Andrea Pelissetto, and Ettore Vicari, “Finite-size scaling at quantum transitions”, *Phys. Rev. B* **89**, 094516 (2014).
- [45] Andrea Pelissetto and Ettore Vicari, “Scaling behaviors at quantum and classical first-order transitions”, arXiv preprint arXiv:2302.08238 , (2023).
- [46] Anushya Chandran et al., “Kibble-Zurek problem: Universality and the scaling limit”, *Physical Review B* **86**, 064304 (2012).
- [47] Andrea Pelissetto, Davide Rossini, and Ettore Vicari, “Scaling properties of the dynamics at first-order quantum transitions when boundary conditions favor one of the two phases”, *Physical Review E* **102**, 012143 (2020).
- [48] Haralambos Panagopoulos, Andrea Pelissetto, and Ettore Vicari, “Dynamic scaling behavior at thermal first-order transitions in systems with disordered boundary conditions”, *Physical Review D* **98**, 074507 (2018).
- [49] Massimo Campostrini, Andrea Pelissetto, and Ettore Vicari, “Quantum Ising chains with boundary fields”, *Journal of Statistical Mechanics: Theory and Experiment* **2015**, P11015 (2015).
- [50] Andrea Pelissetto, Davide Rossini, and Ettore Vicari, “Finite-size scaling at first-order quantum transitions when boundary conditions favor one of the two phases”, *Physical Review E* **98**, 032124 (2018).
- [51] Davide Rossini and Ettore Vicari, “Ground-state fidelity at first-order quantum transitions”, *Physical Review E* **98**, 062137 (2018).

- [52] Wojciech H Zurek, Uwe Dorner, and Peter Zoller, “Dynamics of a quantum phase transition”, *Physical review letters* **95**, 105701 (2005).
- [53] Davide Rossini and Ettore Vicari, “Coherent and dissipative dynamics at quantum phase transitions”, *Physics Reports* **936**, 1–110 (2021).
- [54] Francesco Tarantelli and Ettore Vicari, “Out-of-equilibrium quantum dynamics of fermionic gases in the presence of localized particle loss”, *Phys. Rev. A* **105**, 042214 (2022).
- [55] Michael Zwolak and Guifré Vidal, “Mixed-State Dynamics in One-Dimensional Quantum Lattice Systems: A Time-Dependent Superoperator Renormalization Algorithm”, *Phys. Rev. Lett.* **93**, 207205 (2004).
- [56] T. Schultz E. Lieb and D. Mattis, “Two soluble models of an antiferromagnetic chain”, *Ann. Phys.* **16**, 407 , (1961).
- [57] S. Katsura, “Statistical mechanics of the anisotropic linear Heisenberg model”, *Phys. Rev.* **127**, 1508 , (1962).
- [58] A Yu Kitaev, “Unpaired Majorana fermions in quantum wires”, *Physics-Uspekhi* **44**, 131 (2001).
- [59] Pierre Pfeuty, “The one-dimensional Ising model with a transverse field”, *Annals of Physics* **57**, 79–90 (1970).
- [60] L. Onsager, “Crystal statistics. I. A two-dimensional model with an order-disorder transition”, *Phys. Rev.* **65**, 117 , (1944).
- [61] P. C. Hohenberg and B. I. Halperin, “Theory of dynamic critical phenomena”, *Rev. Mod. Phys.* **49**, 435 , (1977).
- [62] S. k. Ma, “Modern theory of critical phenomena”, Routledge Editor , (2001).
- [63] M. N. Rosenbluth A. H. Teller N. Metropolis A. W. Rosenbluth and E. Teller, “Equation of state calculations by fast computing machines”, *J. Chem. Phys.* **21**, 1087 , (1953).
- [64] M. P. Nightingale and H. W. J. Blöte, “Monte Carlo computation of correlation times of independent relaxation modes at criticality”, *Phys. Rev. B* **62**, 1089 , (2000).
- [65] F.-G. Wang and Hu C.-K, “Universality in dynamic critical phenomena”, *Phys. Rev. E* **56**, 2310 , (1997).
- [66] M. P. Nightingale and H. W. J. Blöte, “Dynamic Exponent of the Two-Dimensional Ising Model and Monte Carlo Computation of the Subdominant Eigenvalue of the Stochastic Matrix”, *Phys. Rev. Lett.* **76**, 4548 , (1996).
- [67] P. Grassberger, “Damage spreading and critical exponents for model A Ising dynamics”, *Physica A* **214**, 547 , (1995).
- [68] G. Costagliola and E. Vicari, “Critical dynamics in trapped particle systems”, *J. Stat. Mech.* L08001 , (2011).
- [69] Anatoli Polkovnikov, “Universal adiabatic dynamics in the vicinity of a quantum critical point”, *Physical Review B* **72**, 161201 (2005).
- [70] Jacek Dziarmaga, “Dynamics of a quantum phase transition: Exact solution of the quantum Ising model”, *Physical review letters* **95**, 245701 (2005).

- [71] A. Polkovnikov and V. Gritsev, “Breakdown of the adiabatic limit in low-dimensional gapless systems”, *Nature Phys.* **4**, 477 , (2008).
- [72] B. K. Chakrabarti U. Divakaran T. F. Rosenbaum A. Dutta G. Aeppli and D. Sen, “Quantum phase transitions in transverse field spin models: From statistical physics to quantum information”, Cambridge University Press , (2015).
- [73] Davide Rossini and Ettore Vicari, “Dynamic Kibble-Zurek scaling framework for open dissipative many-body systems crossing quantum transitions”, *Physical Review Research* **2**, 023211 (2020).
- [74] A. Pelissetto M. Caselle M. Hasenbusch and E. Vicari, “Irrelevant operators in the two-dimensional Ising model”, *J. Phys. A* **35**, 4861 , (2002).
- [75] A. Celi A. Pelissetto P. Calabrese M. Caselle and E. Vicari, “Nonanalyticity of the Callan-Symanzik β -function of two-dimensional O(N) models”, *J. Phys. A* **33**, 8155 , (2000).
- [76] G. Parisi, “Statistical Field Theory”, Addison-Wesley, New York , (1988).
- [77] Andrea Pelissetto and Ettore Vicari, “Off-equilibrium scaling behaviors driven by time-dependent external fields in three-dimensional O (N) vector models”, *Physical Review E* **93**, 032141 (2016).
- [78] Clarence Zener, “Non-adiabatic crossing of energy levels”, *Proceedings of the Royal Society of London. Series A, Containing Papers of a Mathematical and Physical Character* **137**, 696–702 (1932).
- [79] NV Vitanov and BM Garraway, “Landau-Zener model: Effects of finite coupling duration”, *Physical Review A* **53**, 4288 (1996).
- [80] Pierpaolo Fontana, “Scaling behavior of Ising systems at first-order transitions”, *Journal of Statistical Mechanics: Theory and Experiment* **2019**, 063206 (2019).
- [81] Vladimir Privman, “Finite size scaling and numerical simulation of statistical systems”, World Scientific, 1990.
- [82] GG Cabrera and R Jullien, “Role of boundary conditions in the finite-size Ising model”, *Physical Review B* **35**, 7062 (1987).
- [83] Massimo Campostrini et al., “Finite-size scaling at first-order quantum transitions”, *Physical review letters* **113**, 070402 (2014).
- [84] Massimo Campostrini et al., “Finite-size scaling at the first-order quantum transitions of quantum Potts chains”, *Physical Review E* **91**, 052103 (2015).
- [85] B Nienhuis and M Nauenberg, “First-order phase transitions in renormalization-group theory”, *Physical Review Letters* **35**, 477 (1975).
- [86] Vladimar Privman and Michael E Fisher, “Finite-size rounding of first-order transitions”, *Journal of Applied Physics* **57**, 3327–3328 (1985).
- [87] Michael E Fisher and A Nihat Berker, “Scaling for first-order phase transitions in thermodynamic and finite systems”, *Physical Review B* **26**, 2507 (1982).
- [88] Michael E Fisher and Vladimir Privman, “First-order transitions breaking O (n) symmetry: finite-size scaling”, *Physical Review B* **32**, 447 (1985).

- [89] Mario Collura and Dragi Karevski, “Critical quench dynamics in confined systems”, *Physical review letters* **104**, 200601 (2010).
- [90] I-Kang Liu et al., “Kibble-Zurek dynamics in a trapped ultracold Bose gas”, *Physical Review Research* **2**, 033183 (2020).
- [91] Victor Mukherjee, Uma Divakaran, Adolfo del Campo, et al., “Universal finite-time thermodynamics of many-body quantum machines from Kibble-Zurek scaling”, *Physical Review Research* **2**, 043247 (2020).
- [92] Hua-Bi Zeng, Chuan-Yin Xia, and Adolfo Del Campo, “Universal breakdown of kibble-zurek scaling in fast quenches across a phase transition”, *Physical Review Letters* **130**, 060402 (2023).
- [93] Anirban Dutta, Armin Rahmani, and Adolfo Del Campo, “Anti-Kibble-Zurek behavior in crossing the quantum critical point of a thermally isolated system driven by a noisy control field”, *Physical review letters* **117**, 080402 (2016).
- [94] Debasis Sadhukhan et al., “Sonic horizons and causality in phase transition dynamics”, *Phys. Rev. B* **101**, 144429 (2020), URL: <https://link.aps.org/doi/10.1103/PhysRevB.101.144429>.
- [95] K. Pyka et al., “Topological defect formation and spontaneous symmetry breaking in ion Coulomb crystals”, *Nature Comm.* **4**, (2013). URL: <https://doi.org/10.1038/ncomms3291>.
- [96] Nir Navon et al., “Emergence of a turbulent cascade in a quantum gas”, *Nature* **539**, 72–75 (2016), URL: <https://doi.org/10.1038%2Fnature20114>.
- [97] Fernando J. Gómez-Ruiz, Jack J. Mayo, and Adolfo del Campo, “Full Counting Statistics of Topological Defects after Crossing a Phase Transition”, *Phys. Rev. Lett.* **124**, 240602 (2020), URL: <https://link.aps.org/doi/10.1103/PhysRevLett.124.240602>.
- [98] Yuki Bando et al., “Probing the universality of topological defect formation in a quantum annealer: Kibble-Zurek mechanism and beyond”, *Phys. Rev. Res.* **2**, 033369 (2020), URL: <https://link.aps.org/doi/10.1103/PhysRevResearch.2.033369>.
- [99] Fernando J. Gómez-Ruiz, David Subires, and Adolfo del Campo, “Role of boundary conditions in the full counting statistics of topological defects after crossing a continuous phase transition”, *Phys. Rev. B* **106**, 134302 (2022), URL: <https://link.aps.org/doi/10.1103/PhysRevB.106.134302>.
- [100] Stefano Scopa and Sascha Wald, “Dynamical off-equilibrium scaling across magnetic first-order phase transitions”, *Journal of Statistical Mechanics: Theory and Experiment* **2018**, 113205 (2018).
- [101] Andrea Pelissetto, Davide Rossini, and Ettore Vicari, “Out-of-equilibrium dynamics driven by localized time-dependent perturbations at quantum phase transitions”, *Physical Review B* **97**, 094414 (2018).
- [102] Aritra Sinha, Titas Chanda, and Jacek Dziarmaga, “Nonadiabatic dynamics across a first-order quantum phase transition: Quantized bubble nucleation”, *Physical Review B* **103**, L220302 (2021).

- [103] Ivan B Coulamy, Andreia Saguia, and Marcelo S Sarandy, “Dynamics of the quantum search and quench-induced first-order phase transitions”, *Physical Review E* **95**, 022127 (2017).
- [104] Keita Shimizu et al., “Dynamics of first-order quantum phase transitions in extended Bose–Hubbard model: from density wave to superfluid and vice versa”, *New Journal of Physics* **20**, 083006 (2018).
- [105] L-Y Qiu et al., “Observation of generalized Kibble-Zurek mechanism across a first-order quantum phase transition in a spinor condensate”, *Science advances* **6**, eaba7292 (2020).
- [106] Lev Davidovich Landau, “Zur theorie der energieubertragung ii”, *Z. Sowjetunion* **2**, 46–51 (1932).
- [107] Davide Nigro, Davide Rossini, and Ettore Vicari, “Competing coherent and dissipative dynamics close to quantum criticality”, *Phys. Rev. A* **100**, 052108 (2019).
- [108] Giovanni Di Meglio, Davide Rossini, and Ettore Vicari, “Dissipative dynamics at first-order quantum transitions”, *Physical Review B* **102**, 224302 (2020).
- [109] G. Lindblad, “On the generators of quantum dynamical semigroups”, *Commun. Math. Phys.* **48**, 119 , (1976).
- [110] A. Kossakowski V. Gorini and E. C. G. Sudarshan, “Completely positive dynamical semigroups of N-level systems”, *J. Math. Phys.* **17**, 821 , (1976).
- [111] A. Rivas and S. F. Huelga, “Open Quantum System: An Introduction”, SpringerBriefs in Physics, Springer , (2012).
- [112] Antonio D’Abbruzzo and Davide Rossini, “Self-consistent microscopic derivation of Markovian master equations for open quadratic quantum systems”, *Phys. Rev. A* **103**, 052209 (2021).
- [113] C. Kollath H. Fröml A. Ciocchetta and S. Diehl, “Fluctuation-Induced Quantum Zeno Effect”, *Phys. Rev. Lett.* **122**, 040402 , (2019).
- [114] P. Fabritius D. Husmann L. Corman M. Lebrat S. Häusler and T. Esslinger, “Quantized conductance through a spin-selective atomic point contact”, *Phys. Rev. Lett.* **123**, 193605 , (2019).
- [115] K. Mallick P. L. Krapivsky and D. Sels, “Free fermions with a localized source”, *J. Stat. Mech.*, 113108 , (2019).
- [116] S. Diehl S. Wolff A. Sheikhan and C. Kollath, “Non-equilibrium metastable state in a chain of interacting spinless fermions with localized loss”, *Phys. Rev. B* **101**, 075139 , (2020).
- [117] C. Kollath A. Chiocchetta H. Fröml C. Muckel and S. Diehl, “Ultracold quantum wires with localized losses: many-body quantum Zeno effect”, *Phys. Rev. B* **101**, 144301 , (2020).
- [118] C. Torrero G. Ceccarelli and E. Vicari, “Critical parameters from trap-size scaling in trapped particle systems”, *Phys. Rev. B* **87**, 024513 , (2013).
- [119] J. Dalibard I. Bloch and W. Zwerger, “Many-body physics with ultracold gases”, *Rev. Mod. Phys.* **80**, 885 , (2008).

- [120] M. Rigol and A. Muramatsu, “Universal properties of hard-core bosons confined on one-dimensional lattices”, Phys. Rev. A **70**, 031603(R) , (2004).
- [121] M. Campostrini and E. Vicari, “Quantum critical behavior and trap-size scaling of trapped bosons in a one-dimensional optical lattice”, Phys. Rev. A **81**, 063614 , (2010).
- [122] E. Vicari A. Angelone M. Campostrini, “Universal quantum behaviors of interacting fermions in 1D traps: from few particles to the trap thermodynamic limit”, Phys. Rev. A **89**, 023635 , (2014).
- [123] D. Nigro, “Trap effects and the continuum limit of the Hubbard model in the presence of a harmonic potential”, Phys. Rev. A **96**, 033608 , (2017).
- [124] M. Campostrini and E. Vicari, “Trap-size scaling in confined particle systems at quantum transitions”, Phys. Rev. A **81**, 023606 , (2010).
- [125] L. Pollet, “Recent developments in quantum Monte Carlo simulations with applications for cold gases”, Rep. Prog. Phys. **75**, 094501 , (2012).
- [126] B. Horstmann and J. I. Cirac, “Noise-driven dynamics and phase transitions in fermionic systems”, Phys. Rev. A **87**, 012108 , (2013).
- [127] G. E. Santoro R. Fazio M. Keck S. Montangero and D. Rossini, “Dissipation in adiabatic quantum computers: lessons from an exactly solvable model”, New. J. Phys. **19**, 113029 , (2017).
- [128] N. Bartolo F. Minganti A. Biella and C. Ciuti, “Spectral theory of Liouvillians for dissipative quantum transitions”, Phys. Rev. A **98**, 042118 , (2018).
- [129] K. V. Kepesidis and M. J. Hartmann, “Bose-Hubbard model with localized particle losses”, Phys. Rev. A **85**, 063620 , (2012).
- [130] T. Prosen and I. Pizorn, “Quantum Phase Transition in a Far-from-Equilibrium Steady State of an XY Spin Chain”, Phys. Rev. Lett. **101**, 105701 , (2008).
- [131] Toma Prosen, “Third quantization: a general method to solve master equations for quadratic open Fermi systems”, *New Journal of Physics* **10**, 043026 (2008).
- [132] B. Misra and E. C. G. Sudarshan, “The Zeno’s paradox in quantum theory”, *Journal of Mathematical Physics* **18**, 756–763 (1977).
- [133] P. Facchi and S. Pascazio, “Quantum Zeno dynamics: Mathematical and physical aspects”, J. Phys. A: Math. Theor. **41**, 493001 , (2008).
- [134] I. Danshita Y. Takasu T. Tomita S. Nakajima and Y. Takahashi, “Observation of the Mott insulator to superfluid crossover of a driven-dissipative Bose-Hubbard system”, Adv. **3**, e1701513 , (2017).
- [135] D. Sels P. E. Dolgirev J. Marino and E. Demler, “Non-Gaussian correlations imprinted by local dephasing in fermionic wires”, Phys. Rev. B **102**, 100301(R) , (2020).
- [136] M. Campostrini and E. Vicari, “Critical behavior and scaling in trapped systems”, Phys. Rev. Lett. **102**, 240601 , (2009).
- [137] Yi-Neng Zhou, Liang Mao, and Hui Zhai, “Rényi entropy dynamics and Lindblad spectrum for open quantum systems”, *Phys. Rev. Research* **3**, 043060 (2021).

- [138] Alessio Franchi and Francesco Tarantelli, “Liouvillian gap and out-of-equilibrium dynamics of a sunburst Kitaev ring: from local to uniform dissipation”, arXiv:2305.04207 , (2023).
- [139] Taiki Haga et al., “Quasiparticles of Decoherence Processes in Open Quantum Many-Body Systems: Incoherentons”, arXiv:2211.14991 , (2022).
- [140] J. P. Blaizot and G. Ripka, “Quantum Theory of Finite Systems”, Cambridge, Massachusetts: The MIT Press, 1986.
- [141] Giulia Piccitto, Michele Campisi, and Davide Rossini, “The Ising critical quantum Otto engine”, [New Journal of Physics](#) **24**, 103023 (2022).
- [142] A. Bácsi and B. Dóra, “Kibble-Zurek scaling due to environment temperature quench in the transverse field Ising model”, [Scientific Rep.](#) **13**, 1 , (2023).
- [143] Andrea Pelissetto and Ettore Vicari, “Dynamic finite-size scaling at first-order transitions”, [Physical Review E](#) **96**, 012125 (2017).
- [144] J. P. Carini S. L. Sondhi S. M. Girvin and D. Shahar, “Continuous quantum phase transitions”, [Rev. Mod. Phys.](#) **69**, 315 , () .
- [145] Francesco Tarantelli and Ettore Vicari, “Thermal bath effects in quantum quenches within quantum critical regimes”, [Phys. Rev. B](#) **108**, 035128 (2023).
- [146] M. Abramowitz and I. A. Stegun, “Handbook of Mathematica Functions”, Dover, New York , (1964).
- [147] S. N. Shevchenko O. V. Ivashenko and F. Nori, “Quantum Control via Launda-Zener-Stückelberg-Majorana Transitions”, arXiv:2203.16348 , (2022).